University of California
Santa Barbara

Bulk and Nanoscale Methods for the Characterization of Organic Solar Cells

A dissertation submitted in partial satisfaction
of the requirements for the degree

Doctor of Philosophy
in
Chemistry

by

Samuel Collins

Committee in charge:

Professor Thuc-Quyen Nguyen, Chair
Professor Steven Buratto
Professor Michael Chabinyc
Professor Michael Gordon

March 2017

The Dissertation of Samuel Collins is approved.

Professor Steven Buratto

Professor Michael Chabinyc

Professor Michael Gordon

Professor Thuc-Quyen Nguyen, Committee Chair

January 2017

Bulk and Nanoscale Methods for the Characterization of Organic Solar Cells

by

Samuel Collins

Dedicated to my parents, Angela and Dwayne Collins

Acknowledgements

I would first of all like to thank my advisor, Thuc-Quyen Nguyen, for her leadership and ingenuity, and for providing so many opportunities to learn, grow, and travel the world. This dissertation has been financially supported by the Institute for Collaborative Biotechnologies at UCSB, funded by the Army Research Office, and through funding from the Office of Naval Research and the National Science Foundation. The Department of Chemistry and Biochemistry at UCSB has also provided financial support through teaching assistantships. To my long list of mentors and collaborators in the Center for Polymers and Organic Solids, Drs. Yuan Zhang, Peter Zalar, Michele Guide, Jianhua Liu, Martijn Kuik, Huiqiong Zhou, Lei Ying, Chris Takacs, Oleksandr Mikhnenko, Chris Proctor, Alexander Mikhailovsky, Jack Love, Zach Rengert, Viktor Brus, Ming Wang, Cheng-Kang Mai, Jes Sherman, Jang Jo, Mike Heiber, Cristiano Woellner, Tom van der Poll, Xiaofeng Liu, and Jenny Du, to my cohorts in the Nguyen group Drs. Niva Ran and Hung Phan, and to professors Guillermo Bazan and Alan Heeger: you have been excellent companions and have given me a high standard for which to strive. I'd like to thank Professor David Ginger for providing my entry point to academic research at the University of Washington, along with Drs. Guozheng Shao, Raj Giridharagopal, and Obadiah Reid. I'm grateful to my Mom and Dad for a youth filled with music, nature, exploration, and learning, and for showing me what it looks like to be a decent human being, to my sister Danelle, for giving me a head start by teaching me her grade school homework, to my grandparents, Ray and Kay Mosher, whose generous support helped me jump back into academia, and to the rest of my family, who lifted me up so much through the years. Finally, I want to acknowledge the loving patience and support of my wonderful wife Kate and daughter Sylvia—you have helped me reach a goal I once thought was unattainable, and I promise to do everything I can to return the favor.

Curriculum Vitæ

Samuel Collins

Education

2017 Ph.D. in Chemistry (Expected), University of California, Santa Barbara.

2011 B.S. in Chemistry (with Honors), University of Washington.

2004 B.A. in Music, University of Puget Sound.

Presentations

Submitted talk at the 12^{th} International Symposium on Functional π-Electron Systems, Seattle, WA.

Poster at the Gordon Research Conference on Electronic Processes in Organic Materials, Lucca, Italy.

Publications

Collins, S. D., Ran, N. A., Heiber, M. C. & Nguyen, T.-Q. Small is Powerful: Recent Progress in Solution-Processed Small Molecule Solar Cells. *Advanced Energy Materials* **2017**, *7*, 1602242.

Collins, S. D., Proctor, C. M., Ran, N. A., & Nguyen, T.-Q. Understanding Open-Circuit Voltage Loss Through the Density of States in Organic Bulk Heterojunction Solar Cells. *Advanced Energy Materials* **2016**, *6*, 1501721.

Collins, S. D., Mikhnenko, O.V., Nguyen, T. L., Rengert, Z. D., Bazan, G. C., Woo, H. Y. & Nguyen, T.-Q. Real-time Observation of Ion Motion in Conjugated Polyelectrolytes with Kelvin Probe Force Microscopy. *Advanced Electronic Materials* **2017**, *3*, 1700005.

Takacs, C. J., Collins, S. D., Love, J. A., Mikhailovsky, A. A., Wynands, D., Bazan, G. C., Nguyen, T.-Q. & Heeger, A. J. Mapping Orientational Order in a Bulk Heterojunction Solar Cell with Polarization-Dependent Photoconductive Atomic Force Microscopy. *ACS Nano* **2014**, *8*, 8141.

Love, J. A., Collins, S. D., Nagao, I., Mukherjee, S., Ade, H., Bazan, G. C. & Nguyen, T.-Q. Interplay of Solvent Additive Concentration and Active Layer Thickness on the Performance of Small Molecule Solar Cells. *Advanced Materials* **2014**, *26*, 7308.

Mikhnenko, O. V., Collins, S. D. & Nguyen, T.-Q. Rectifying Electrical Noise with an Ionic-Organic Ratchet. *Advanced Materials* **2015**, *27*, 2007.

Brus, V. V., Collins, S. D., Mikhnenko, O. V., Wang, M., Bazan, G. C., & Nguyen, T.-Q. Fabricating Low-Cost Ionic-Organic Electronic Ratchets with Graphite Pencil and Adhesive Tape. *Advanced Electronic Materials* **2016**, *2*, 1500344.

Zhang, Y., Wang, M., Collins, S. D., Zhou, H., Phan, H., Proctor, C., Mikhailovsky, A. A., Wudl, F. & Nguyen, T.-Q. Enhancement of the Photoresponse in Organic Field-Effect Transistors by Incorporating Thin DNA Layers. *Angewandte Chemie International Edition* **2014**, *53*, 244.

Ying, L., Zalar, P., Collins, S. D., Chen, Z., Mikhailovsky, A. A., Nguyen, T.-Q. & Bazan, G. C. All-Conjugated Triblock Polyelectrolytes. *Advanced Materials* **2012**, *24*, 6496.

Zhang, Y., Zalar, P., Kim, C., Collins, S. D., Bazan, G. C. & Nguyen, T.-Q. DNA Interlayers Enhance Charge Injection in Organic Field-Effect Transistors. *Advanced Materials* **2012**, *24*, 4255.

Zhou, H., Zhang, Y., Mai, C. K., Collins, S. D., Bazan, G. C., Nguyen, T.-Q. & Heeger, A. J. Polymer Homo-Tandem Solar Cells with Best Efficiency of 11.3%. *Advanced Materials* **2015**, *27*, 1767.

Zhou, H., Zhang, Y., Mai, C. K., Collins, S. D., Nguyen, T.-Q., Bazan, G. C. & Heeger, A. J. Conductive Conjugated Polyelectrolyte as Hole-Transporting Layer for Organic Bulk Heterojunction Solar Cells. *Advanced Materials* **2014**, *26*, 780.

Zhou, H., Zhang, Y., Seifter, J., Collins, S. D., Luo, C., Bazan, G. C., Nguyen, T.-Q. & Heeger, A. J. High-Efficiency Polymer Solar Cells Enhanced by Solvent Treatment. *Advanced Materials* **2013**, *25*, 1646.

Jo, J., Pouliot, J.-R., Wynands, D., Collins, S. D., Kim, J. Y., Nguyen, T. L., Woo, H. Y., Sun, Y., Leclerc, M. & Heeger, A. J. Enhanced Efficiency of Single and Tandem Organic Solar Cells Incorporating a Diketopyrrolopyrrole-Based Low-Bandgap Polymer by Utilizing Combined ZnO/Polyelectrolyte Electron Transport Layers *Advanced Materials* **2013**, *25*, 4783.

Sherman, J. B., Puroshothaman, B., Parkin, S. R., Kim, C., Collins, S. D., Anthony, J., Nguyen, T.-Q. & Chabinyc, M. L. Role of Crystallinity of Non-Fullerene Acceptors in Bulk Heterojunctions *Journal of Materials Chemistry A* **2015**, *3*, 9989.

Ran, N. A., Love, J. A., Takacs, C. J., Sadhanala, A., Beavers, J. K., Collins, S. D., Huang, Y., Wang, M., Friend, R. H., Bazan, G. C. & Nguyen, T.-Q. Harvesting the Full Potential of Photons with Organic Solar Cells. *Advanced Materials* **2016**, *28*, 1482.

Abstract

Bulk and Nanoscale Methods for the Characterization of Organic Solar Cells

by

Samuel Collins

Organic photovoltaics (OPVs) based on conjugated polymer and small molecule semiconductors are a promising technology for solar energy capture. The compatibility of organic semiconductors with solution processing allows OPV devices to be prepared using high-throughput manufacturing processes on flexible substrates, opening up applications not available to most commercial technologies. The most efficient devices utilize a bulk heterojunction (BHJ) active layer, a two-component solid state mixture that provides efficient photocurrent generation, but also presents several performance-limiting issues. The consequences of structural and energetic disorder in these systems can be difficult to quantify using existing experimental techniques. This dissertation describes three studies presenting new approaches to measuring the morphological, energetic, and interfacial properties of BHJ solar cells. First, a study of static disorder in the density of states (DOS) is carried out *in-situ* in several BHJ blends. DOS tail states are characterized here by combining the charge carrier density dependence of V_{OC} with disorder-dependent band bending behavior. A direct connection is found between disorder observed within donor and acceptor phases and the overall impact of disorder on open-circuit voltage. Disorder is shown to be both material- and morphology-dependent, significantly impacting device performance. Next, a new technique, polarization-dependent photoconductive atomic force microscopy, is used to measure local orientation-dependent photocurrent in BHJ active layers with resolution below 100 nanometers. A high-performing small molecule donor is found to exhibit in-plane, micron-scale orientational order not seen

by typical diffraction or topography measurements. The observed liquid-crystalline networks provide a unique picture of morphology that goes beyond the typical binary of crystalline vs amorphous. Lastly, a technique is presented to measure the ion transport properties in conjugated polyelectrolytes (CPEs) used as interlayers in OPVs. Ion motion is characterized using Kelvin probe force microscopy to observe the relaxation over time of bias-stressed CPE device channels. Based on studies of systematically varied CPE structures, the number of ionic side chains per monomer shows a strong correlation with ionic conductivity. These results help inform the material design of CPEs, not just for interlayers in organic optoelectronic devices, but also for a number of emerging mixed ionic-electronic conductor applications.

Contents

List of Figures

List of Tables

Chapter 1

Introduction

1.1 Background and Motivation

Photovoltaic devices based on conjugated polymers and small molecules, also known as organic photovoltaics (OPV), are a promising technology for solar energy capture. The field has attracted a growing number of researchers over the last few decades, and now produces on the order of a thousand publications each year. Just within the last ten years, the record power conversion efficiency (PCE) of single junction devices has increased from 5%[1] to a recently certified result of 11.5%.[2] Continuing efforts to increase PCE and long-term device stability have brought OPVs to the point of commercial viability, where products such as semi-transparent solar windows for integration into energy-zero buildings are currently under development. Although they lag behind silicon cells in peak efficiency, they still hold potential for use in utility-scale applications due to their ability to perform better under the low light intensities and elevated temperatures experienced under real-world conditions.[3] The compatibility of organic semiconductors with solution processing also means that OPVs can be prepared using high-throughput manufacturing processes on flexible substrates, opening up new applications not available

to most inorganic solar cells.

The most efficient devices utilize a bulk heterojunction (BHJ) active layer 100-300 nm thick, comprising a blend of electron donor and electron acceptor molecules. This two-component solid state mixture allows for efficient photocurrent generation, but it also presents a set of issues that limit performance and lead to complicated operational physics. Unlike crystalline silicon, photoexcitation in organic semiconductors does not immediately yield free carriers, resulting instead in a bound electron-hole pair known as an exciton.[4] Photocurrent production can be achieved by using two materials with offset energy levels, which allows for spontaneous charge transfer that helps the charges escape their Coulomb well. The idealized form of the BHJ morphology is inherently complex, and requires pure, ordered donor and acceptor phases of around 10-20 nm in size with mixed regions at donor-acceptor interfaces. The structural and energetic disorder in these systems has direct consequences on device operation, and understanding these structure-property relationships remains one of the most vital areas of research in the field.

This dissertation describes three studies unified by their presentation of new approaches to measuring the morphological, energetic, and/or interfacial properties of BHJ solar cells. First, a study of static electronic disorder in the density of states (DOS) of donor and acceptor phases is carried out *in-situ* in several different BHJ solar cells. DOS tail states are characterized here by combining the charge carrier density dependence of V_{OC} with disorder-dependent band bending behavior. A direct connection is found between bulk disorder observed within donor and acceptor phases and the interfacial disorder determined from the dependence of open-circuit voltage on carrier density. The effect of disorder on V_{OC} is also shown to be both material- and morphology-dependent, with voltage losses due to excess disorder as high as 200 mV. Next, a technique is demonstrated for measuring the ion transport properties of ion-functionalized conjugated polymers used as electrode-modifying interlayers in high-performance OPVs. Ion motion is

characterized by applying a bias stress to a planar, FET-like channel and observing the relaxation of ions over time using Kelvin probe force microscopy. Based on observations of a series of conjugated polyelectrolyte (CPE) materials, polymer structure is found to play the most critical role in the conductivity of mobile ion species, where a change only in the number of ionic side chains per monomer from two to six increases ionic conductivity by nearly two orders of magnitude. The result has implications for material design of CPEs, not just for interlayers in organic optoelectronic devices, but also for a number of emerging mixed ionic-electronic conductor applications. Lastly, a new technique, polarization-dependent photoconductive atomic force microscopy (pd-pcAFM), is used to map molecular orientation at a resolution of 10s of nanometers by measuring local polarization-dependent photocurrent. A high-performing small molecule donor is found to exhibit in-plane, micron-scale orientational order that is not apparent by typical diffraction techniques or surface topography measurements. Liquid-crystalline networks are formed independently of morphology optimization, offering valuable insight into film microstructure and the nature of molecular self-assembly that goes beyond the binary of crystalline vs amorphous. A brief overview of the fundamental concepts and operating principles of organic solar cells follows.

1.2 Operating Principles of Organic Solar Cells

The semiconducting properties of conjugated polymers and small molecules, first reported forty years prior to this writing,[5] arise from having extended p-orbital systems that allow for the delocalization of charge carriers. The frontier orbitals of organic semiconductors, the highest occupied molecular orbital (HOMO) and lowest unoccupied molecular orbital (LUMO), serve as the effective valence and conduction levels, respec-

tively. The corresponding transport of holes and electrons in these levels proceeds via a hopping mechanism between localized, polaronic states.[6,7] Introducing chromophores to the conjugated backbone affords optoelectronic properties that can be synthetically tuned for use in light-emitting and photovoltaic devices. For solar cell devices, materials are designed to have bandgaps that overlap with the solar spectrum and energy levels that are positioned to maximize photovoltage, while still maintaining an energetic offset to allow charge generation. Furthermore, molecular design must also take into account solubility in typical processing solvents, and strive to yield ordered structures within the film that lead to efficient charge transport.

The concept of the ideal OPV morphology has evolved rather significantly over the years, as is illustrated in **Figure 1.1**. Initially, the introduction of a bilayer heterojunction helped to provide the necessary driving force for charge separation (Figure 1.1a). Due to the low relative permittivity of organic semiconductors (OSCs), usually between 3 and 4, photoexcitations result in bound electron-hole pairs called excitons that can only generate free carriers by separating at a heterojunction interface. Excitons have short diffusion lengths, on the order of 5-15 nm,[8,9] and so a high interfacial area between electron donor and electron acceptor is needed to produce photocurrent. This has led to the aforementioned BHJ active layer, which is cast from blend solutions of donor and acceptor molecules, as it offers a solution to the issue of photocurrent production by allowing nearly all excitons generated within a material to be quenched at an internal interface. In contrast to bilayer solar cells, BHJ solar cell devices can be very efficient at generating photocurrent and are capable of reaching external quantum efficiencies above 80%. An idealized bulk heterojunction consisting of interdigitated pillars (Figure 1.1b) was introduced as an ideal balanced of domain connectivity and length-scale of phase separation, yet remains impractical and is only demonstrated in rare cases.[10] Instead, researchers have focused on optimizing the BHJ morphology to achieve domains of ap-

propriate size for the exciton diffusion length and interconnected for transport to the electrodes (Figure 1.1c). Finally, in the last few years researchers have been calling attention to a 3-phase model for morphology, which includes donor and acceptor phases, as well as a mixed region with both donor and acceptor molecules between the pure phases (Figure 1.1d).

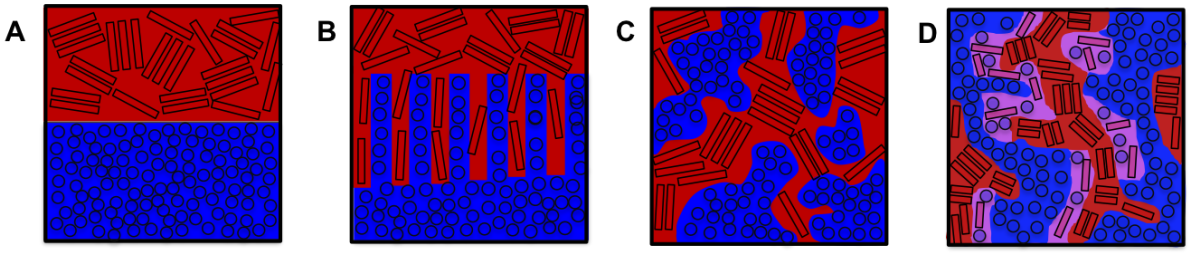

Figure 1.1: (a) first concept of donor/acceptor heterojunction; (b) ideal donor/acceptor morphology, accounting for exciton diffusion lengths; (c) representation of BHJ morphology with strict phase separation (d) emergent BHJ morphology, taking into account the 'third-phase' of a mixed donor:acceptor morphology. Reproduced with permission.[23] Copyright 2017, Wiley-VCH.

The mixed phase is thought in some cases to be beneficial and necessary for good charge separation and to suppress recombination processes. Generating photocurrent requires that excitons are separated into free charge carriers that can be extracted from the device. To overcome the exciton binding energy, which is generally in the range of 0.3 to 1.0 eV,[11–14] a heterojunction between an electron donating material (donor) and an electron accepting material (acceptor) is needed.[15,16] Excitons created away from the donor-accepter heterojunction must then migrate to the interface,[17] where an electron is transferred from the donor to the acceptor, creating a weakly bound electron-hole pair across the donor/acceptor interface called a charge transfer (CT) state. This CT state acts as an intermediate state before the electron and hole separate from each other to become free charge carriers that generate a photocurrent in the solar cell.[18–22] As a result, photocurrent generation, which mainly affects the short-circuit current of the solar cell, is broadly dictated by the three processes of exciton diffusion, exciton dissociation, and

charge separation, as illustrated in **Figure 1.2**.

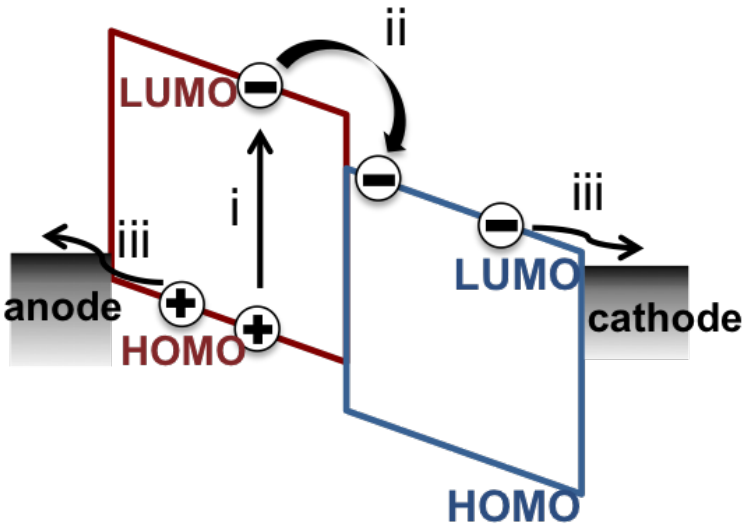

Figure 1.2: (i) photon is absorbed by a donor or acceptor molecule to create an exciton, which then diffuses to the donor-acceptor interface, (ii) exciton dissociates by electron transfer from the donor to the acceptor to create a CT state, which then dissociates to create free charge carriers, and (iii) charge carriers are transported through their respective phases towards the electrodes and extracted from the active layer at the electrodes.

The efficiency of solar cells is directly proportional to three parameters of open-circuit voltage (V_{OC}), short-circuit current (J_{SC}), and fill factor (FF), and the product of these values is equal to the maximum power output density, P_{max}, of the cell. Power conversion efficiency is determined as the ratio between P_{max} and the incident power density of illumination, P_{in}. V_{OC} generally follows the energy difference between the highest occupied molecular orbital (HOMO) of the donor material and the lowest unoccupied molecular orbital (LUMO) of the acceptor material.[25] It is also affected by the rates of carrier generation and recombination, the presence of energetic tail states or trap states, and in some cases by intermolecular interactions that effectively shift the donor ionization potential and the acceptor electron affinity.[26–28] J_{SC} is most strongly affected by the rate of generation, which depends on the combination of total film absorption and the

efficiency with which excitons reach donor-acceptor interfaces, and requires the presence of an energetic driving force for charge separation.[29,30] Fill factor, which is given by the ratio $\frac{P_{max}}{J_{SC} \times V_{OC}}$, depends on the efficient extraction of photo-generated carriers from the device.[31–33] This extraction efficiency relies in part on the charge carrier mobilities of the electron (acceptor) and hole (donor) transport materials, and generally improves with the presence of crystalline or relatively pure aggregate domains in the BHJ blend. Given the competing demands of these device parameters, optimizing overall device efficiency requires carefully controlled nanoscale phase separation that is balanced to maintain efficient charge generation while suppressing recombination. Controlling film morphology is the most prevailing issue in OPVs, and its complexity has attracted considerable efforts in synthesis, molecular design, material processing, device engineering, and theoretical modeling.

1.3 Permissions and Attributions

This dissertation contains adapted reproductions of works written by the author.

1. Chapter 1 is partially adapted with permission from Collins *et al.*, Small is Powerful: Recent Progress in Solution-Processed Small Molecule Solar Cells. *Advanced Energy Materials* **2017**, *7*, 1602242. Copyright 2017, Wiley-VCH.

2. Chapter 3 has been adapted with permission from Collins *et al.*, Understanding Open-Circuit Voltage Loss Through the Density of States in Organic Bulk Heterojunction Solar Cells. *Advanced Energy Materials* **2016**, *6*, 1501721. Copyright 2016, Wiley-VCH.

3. Chapter 4 is adapted with permission from Takacs, Collins *et al.*, Mapping Orientational Order in a Bulk Heterojunction Solar Cell with Polarization-Dependent

Photoconductive Atomic Force Microscopy. *ACS Nano* **2014**, *8*, 8141. Copyright 2014, American Chemical Society.

4. Chapter 5 is adapted with permission from Collins *et al.*, Real-time Observation of Ion Motion in Conjugated Polyelectrolytes with Kelvin Probe Force Microscopy. *Advanced Electronic Materials* **2017**, *3*, 1700005.

1.4 Summary of Chapters

Chapter 2

Some of the experimental methods used in the course of this dissertation warrant a more thorough background. In Chapter 2 following, we provide a more fundamental description of the physical phenomena, methods, and assumptions involved in the techniques most central to this work. With this background, the reader may obtain a clearer understanding of the experiments described in Chapters 3, 4, and 5. The techniques discussed here include impedance spectroscopy, Kelvin probe, Kelvin probe force microscopy, and photoconductive atomic force microscopy.

Chapter 3

This chapter presents a thorough study of the effect of energetic disorder on the open-circuit voltage in organic solar cells through a study of six bulk heterojunction blends based on small molecule donor materials. After providing introduction and background on energetic disorder in organic semiconductors, characterization of the density of states is presented using different techniques including Fourier transform photoelectron spectroscopy (FTPS), Kelvin probe, current-voltage characteristics, and impedance spectroscopy. The results are analyzed to present an estimate of the impact of energetic

disorder on voltage loss.

Chapter 4

This chapter describes a method for analyzing orientational order in bulk heterojunction solar cells with symmetry-breaking, polarization-dependent photoconductivity. The technique is carried out on a high performance solar cell blend, along with an unoptimized condition of that same blend and a neat film of donor material. This technique reveals latent liquid crystalline order that is present in the donor material regardless of whether it is blended with PCBM acceptor. The degree of orientational order is estimated through a quantitative analysis of the strength of polarization-dependent photocurrent.

Chapter 5

In the final chapter, Kelvin probe force microscopy (KPFM) is used to study the relaxation of mobile ions in bias-stressed conjugated polyelectrolytes. The ion motion is tracked by observing the channel potential over time, and the data are analyzed to yield a decay transient for a population of mobile ions near the electrode interface. Monte Carlo modeling is used to reproduce these decay data as a function of the mobility and free ion carrier density. Impedance spectroscopy is used to determine the apparent ionic conductivity in these materials, revealing a trend that is consistent with the KPFM ion decay data.

References

1. Peet, J.; Kim, J. Y.; Coates, N. E.; Ma, W. L.; Moses, D.; Heeger, A. J.; Bazan, G. C. *Nat Mater* **2007**, *6*, 497–500.

2. Zhao, J.; Li, Y.; Yang, G.; Jiang, K.; Lin, H.; Ade, H.; Ma, W.; Yan, H. *Nature Energy* **2016**, *1*, 15027.

3. *Stability and Degradation of Organic and Polymer Solar Cells: Krebs/Stability and Degradation of Organic and Polymer Solar Cells*; Krebs, F. C., Ed.; John Wiley & Sons, Ltd: Chichester, UK, 2012.

4. Scholes, G. D.; Rumbles, G. *Nat Mater* **2006**, *5*, 683–696.

5. Shirakawa, H.; Louis, E. J.; MacDiarmid, A. G.; Chiang, C. K.; Heeger, A. J. *J. Chem. Soc., Chem. Commun.* **1977**, 578–580.

6. Mott, N. F. *Journal of Non-Crystalline Solids* **1968**, *1*, 1–17.

7. Pasveer, W. F.; Cottaar, J.; Tanase, C.; Coehoorn, R.; Bobbert, P. A.; Blom, P. W. M.; de Leeuw, D. M.; Michels, M. A. J. *Phys. Rev. Lett.* **2005**, *94*, 206601.

8. Mikhnenko, O. V.; Blom, P. W. M.; Nguyen, T.-Q. *Energy Environ. Sci.* **2015**, *8*, 1867–1888.

9. Lin, J. D. A.; Mikhnenko, O. V.; Chen, J.; Masri, Z.; Ruseckas, A.; Mikhailovsky, A.; Raab, R. P.; Liu, J.; Blom, P. W. M.; Loi, M. A.; García-Cervera, C. J.; Samuel, I. D. W.; Nguyen, T.-Q. *Mater. Horiz.* **2014**, *1*, 280–285.

10. Matsuo, Y.; Sato, Y.; Niinomi, T.; Soga, I.; Tanaka, H.; Nakamura, E. *J. Am. Chem. Soc.* **2009**, *131*, 16048–16050.

11. Brédas, J.-L.; Cornil, J.; Heeger, A. J. *Adv. Mater.* **1996**, *8*, 447–452.

12. Knupfer, M. *Appl. Phys. A* **2003**, *77*, 623–626.

13. Alvarado, S. F.; Seidler, P. F.; Lidzey, D. G.; Bradley, D. D. C. *Phys. Rev. Lett.* **1998**, *81*, 1082–1085.

14. Deibel, C.; Mack, D.; Gorenflot, J.; Schöll, A.; Krause, S.; Reinert, F.; Rauh, D.; Dyakonov, V. *Phys. Rev. B* **2010**, *81*, 085202.

15. Tang, C. W. *Applied Physics Letters* **1986**, *48*, 183–185.

16. Sariciftci, N. S.; Smilowitz, L.; Heeger, A. J.; Wudl, F. *Science* **1992**, *258*, 1474–1476.

17. Haugeneder, A.; Neges, M.; Kallinger, C.; Spirkl, W.; Lemmer, U.; Feldmann, J.; Scherf, U.; Harth, E.; Gügel, A.; Müllen, K. *Phys. Rev. B* **1999**, *59*, 15346–15351.

18. Benson-Smith, J. J.; Goris, L.; Vandewal, K.; Haenen, K.; Manca, J. V.; Vanderzande, D.; Bradley, D. D. C.; Nelson, J. *Adv. Funct. Mater.* **2007**, *17*, 451–457.

19. Loi, M. A.; Toffanin, S.; Muccini, M.; Forster, M.; Scherf, U.; Scharber, M. *Adv. Funct. Mater.* **2007**, *17*, 2111–2116.

20. Hwang, I.-W.; Soci, C.; Moses, D.; Zhu, Z.; Waller, D.; Gaudiana, R.; Brabec, C. J.; Heeger, A. J. *Adv. Mater.* **2007**, *19*, 2307–2312.

21. Kanai, Y.; Grossman, J. C. *Nano Lett.* **2007**, *7*, 1967–1972.

22. Drori, T.; Sheng, C.-X.; Ndobe, A.; Singh, S.; Holt, J.; Vardeny, Z. V. *Phys. Rev. Lett.* **2008**, *101*, 037401.

23. Collins, S. D.; Ran, N. A.; Heiber, M. C.; Nguyen, T.-Q. *Adv. Energy Mater.* **2017**, *7*, 1602242.

24. Deibel, C.; Dyakonov, V. *Rep. Prog. Phys.* **2010**, *73*, 096401.

25. Scharber, M. C.; Mühlbacher, D.; Koppe, M.; Denk, P.; Waldauf, C.; Heeger, A. J.; Brabec, C. J. *Adv. Mater.* **2006**, *18*, 789–794.

26. Sweetnam, S.; Graham, K. R.; Ngongang Ndjawa, G. O.; Heumüller, T.; Bartelt, J. A.; Burke, T. M.; Li, W.; You, W.; Amassian, A.; McGehee, M. D. *J. Am. Chem. Soc.* **2014**, *136*, 14078–14088.

27. Lange, I.; Kniepert, J.; Pingel, P.; Dumsch, I.; Allard, S.; Janietz, S.; Scherf, U.; Neher, D. *J. Phys. Chem. Lett.* **2013**, *4*, 3865–3871.

28. Collins, S. D.; Proctor, C. M.; Ran, N. A.; Nguyen, T.-Q. *Adv. Energy Mater.* **2016**, *6*, 1501721.

29. Gao, F.; Inganäs, O. *Phys. Chem. Chem. Phys.* **2014**, *16*, 20291–20304.

30. Liu, J.; Chen, S.; Qian, D.; Gautam, B.; Yang, G.; Zhao, J.; Bergqvist, J.; Zhang, F.; Ma, W.; Ade, H.; Inganäs, O.; Gundogdu, K.; Gao, F.; Yan, H. *Nature Energy* **2016**, *1*, 16089.

31. Würfel, U.; Neher, D.; Spies, A.; Albrecht, S. *Nat Commun* **2015**, *6*, 6951.

32. Bartelt, J. A.; Lam, D.; Burke, T. M.; Sweetnam, S. M.; McGehee, M. D. *Adv. Energy Mater.* **2015**, *5*, 1500577.

33. Neher, D.; Kniepert, J.; Elimelech, A.; Koster, L. J. A. *Scientific Reports* **2016**, *6*, 24861.

Chapter 2

Bulk and Nanoscale Optoelectronic Characterization Methods

2.1 Impedance Spectroscopy

Impedance spectroscopy is a method commonly used to determine complex impedance and capacitance of a semiconductor or insulator as a function of frequency. An impedance analyzer is used to extract the real and imaginary components of impedance by analyzing the relationship between an AC applied potential and the corresponding AC current through the sample. For test samples prepared with a simple metal-insulator-metal or metal-semiconductor-metal architecture, capacitance can then calculated from the complex impedance by treating the entire sample system as a parallel R-C (resistor-capacitor) circuit. A perfect insulator will have effectively infinite resistance, (or at least immeasurably high resistance), such that the system can be described using only a capacitor. A semiconductor, having finite resistance, instead exhibits a complex impedance that arises from both resistive and capacitive elements. Analysis is often carried out by straightforward analysis of the raw real, imaginary, or complex impedance/capacitance plotted

vs frequency, and analytical models are developed to make physically-based corrections to the data. Alternatively, circuit models containing a more complicated array of circuit elements, including multiple parallel pathways or distributed elements that reflect disorder within the system, have sometimes been used to interpret data—care should be taken, however, to make sure that such circuits have a basis in physical reality. Analysis of impedance and capacitance spectra provides information about parameters such as charge transfer resistance, charge carrier density, and relative permittivity. When mobile ions are present, these spectra also may provide information on parameters such as ionic conductivity or ionic double-layer capacitances.

A significant challenge with many impedance data lies in the interpretation. Frequency plays a critical role in connecting the physical processes taking place within a system to the impedance data. For instance, systems such as organic bulk heterojunction blends may have multiple types of charge carriers that move in response to the probing AC field with different rates or with a distribution of hopping speeds. In most undoped organic semiconductors, low-mobility charge carriers are unable to exhibit a polarization response to high frequency voltage oscillations (>100 kHz), and thus the real impedance at high frequencies reflects resistance from the electrodes and wires. With decreasing frequency, these carriers eventually follow the probing voltage, eventually dominating the observed resistance. When the value of $\frac{1}{f}$ exceeds the characteristic time of the charge hopping process, the real impedance reflects the sum of contributions from the series and charge transport resistances (assuming no other contributions occur at low frequencies). Along these lines, the capacitance spectrum can be used to extract different information about a system depending on the frequency. In the high frequency condition described above, the sample film can effectively be treated as an insulating dielectric layer, and the capacitive response thus comes purely from charging the capacitor formed between the conductive electrodes. As the slower charge carriers in the film begin to respond with

decreasing frequency, a corresponding chemical capacitance occurs due to the spatial rearrangement of charge. As will be described in Chapter 3 and its appendix, the chemical capacitance in bulk-heterojunction solar cells induced by a combination of charge injection from the contacts and photogeneration of carriers can be used to probe the charge carrier density at open circuit voltage.

Impedance analysis holds a number of advantages over strictly DC methods of measuring conductivity. This is particularly true when a hysteretic response occurs, such as in systems with ionic carriers that build up at the electrodes and oppose the applied field given sufficient time to rearrange. An AC probe of this system invokes no net movement of ionic charges within a period of oscillation, and thus the likelihood that the system is changed by the measurement is decreased. Impedance spectroscopy has been used to characterize the transport of ions within polymer electrolytes, which are strictly ionic conductors. Insights gained from this analysis include the nature of the hopping transport, the thermal activation of ionic carriers, and the dependence of these properties on various characteristics of the mobile ions.[1] The same analyses can also be applied to studying systems with mixed ionic and electronic conductivity, so long as ionic conductivity is sufficiently high compared to electronic conductivity.[2] In this case, it becomes important to bring together multiple lines of evidence to be certain that ions are being observed in the system. These considerations will be further discussed in Chapter 5 and its appendix.

2.2 The Kelvin Probe Technique for Measuring Surface Potential

The Kelvin probe technique originates from experimental observations of William Thomson (Lord Kelvin) that two conductors connected to a common ground build up a surface potential proportional to the difference in their work functions. A practical measurement of work function can be carried out via this phenomenon by forming a parallel plate, air-gap capacitor between a conductive probe and a conductive test sample. In this configuration, electrons transfer from the low work function conductor to the high one, resulting in a charged capacitor. When a potential is applied to the probe that is equal and opposite to the contact potential difference (CPD), the capacitance vanishes, as illustrated in **Figure 2.1**. In order to find the CPD, the Kelvin probe setup must be designed to directly or indirectly detect the applied potential at which the charge on the capacitor is minimized, and this is usually accomplished by monitoring the disappearance of the electric field formed between the plates through one of a few different methods. For the measurements carried out in Chapter 3, a variation of Kelvin probe called 'off-null' detection is used.[4] In this technique, the instrument measures the flow of current toward and away from an oscillating conductive probe as it vibrates above the sample surface (f = 70 Hz). The electric field between probe and sample is in this case exaggerated by applying a backing voltage of large positive and negative values. A calibration curve relating the current flow to the probe and the backing potential is established by the system, and the backing potential equal and opposite to the contact potential difference is determined through interpolation of this calibration plot. This method is impressive for its ability to limit noise to as low as 1 mV.

The Kelvin probe technique has been shown as a valid way of measuring the potential of semiconductors, but where the CPD provides the surface Fermi level, or the average

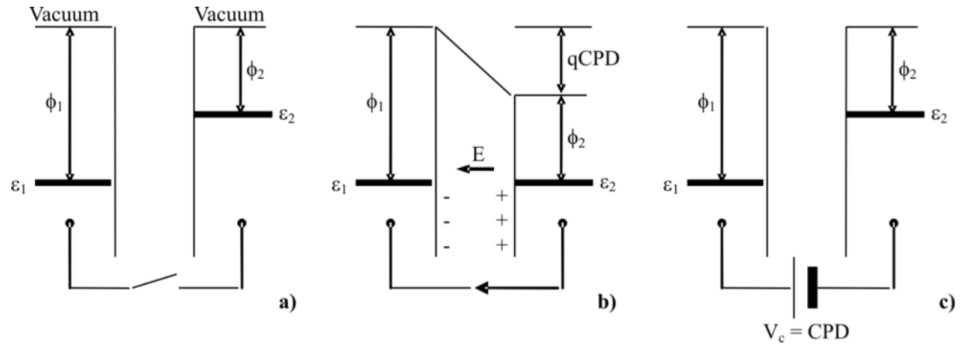

Figure 2.1: a) Two materials 1 and 2 with different work functions ϕ_1 and ϕ_2, corresponding to the energy difference between the Fermi level, E_F, and the vacuum level. b) When the two materials are electrically contacted, electrons flow from 2 to 1 until the Fermi levels are aligned, leading to a contact potential V_b. The charges present in the two materials causes an electric field E. q: electron charge; CPD: contact potential difference. c) The electric field is removed by applying an external potential V_c, which equals the contact potential difference. Reproduced with permission.[3] Copyright 2006, Wiley-VCH.

potential energy of electronic carriers at the surface. In a doped semiconductor, this level is controlled by the dopant concentration. For undoped organic semiconductors, which are essentially intrinsic, it is required that the semiconductor is prepared on a conductive substrate in order to allow for the necessary charging and discharging of the surface to take place quickly enough. The observed Fermi level at the surface of an organic semiconductor (OSC) film has several dependencies, including the energetic structure of the semiconductor, the work function of the underlying conductor, and the thickness of the film. When a conductor with a work function (WF) inside the bandgap of the OSC and sufficiently far away from the ionization potential (IP) and electron affinity (EA) is used, referred to as the vacuum-limited case, the surface Fermi level is equal to the underlying conductor's WF. As the conductor WF approaches the energy levels of the OSC, a charge transfer reaction occurs, eventually pinning the Fermi level to within the tail of the HOMO or LUMO. A quasi-Ohmic contact is formed in semiconductors when the WF of the substrate approaches the pinning level in the HOMO or LUMO. This trend is shown

for polymer semiconductors in **Figure 2.2**, where a 'Z'-shaped plot of polymer WF vs substrate WF shows a vacuum level-aligned region of slope unity and pinned regions of slope zero. When an Ohmic substrate electrode is used, it is possible to probe details of

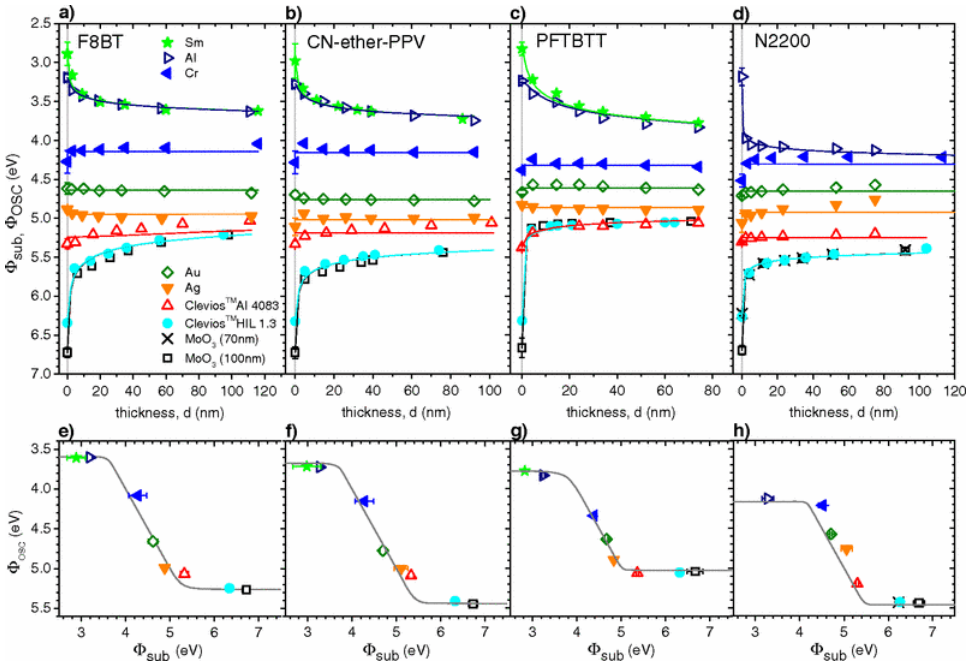

Figure 2.2: a-d) work function of conjugated polymers for a range of thicknesses on substrates of varying work function. e-h) Z-curve plots, showing work function observed at the surface of 70 nm films of respective polymer as a function of substrate work function. Reproduced with permission.[5] Copyright 2011, American Physical Society.

the OSC energetic structure by observing the thickness-dependent WF. Analytical and numerical methods can be applied to recreate the effective band-bending profile obtained from the thickness-dependent WF, where the output of the fit describes the density of states (DOS) of the OSC.[5] Generally speaking, the severity of the band bending observed over a distance of hundreds of nanometers from the semiconductor-conductor interface is directly proportional to the disorder in the DOS of the semiconductor. Further detail on fitting the effective band bending profile is described in further detail in Chapter 3 and its Appendix.

2.3 Kelvin Probe Force Microscopy (KPFM)

Kelvin probe force microscopy (KPFM) is a variation on the Kelvin probe technique that measures surface potential with resolution on the order of an atomic force microscope (AFM) tip. Like the general Kelvin probe technique described previously, the contact potential difference (CPD) is measured by sensing the electric field between a conductive probe and a test sample.[6–8] In KPFM, the CPD is determined through a feedback mechanism that applies a backing potential to the probe to minimize electrostatic interactions. In most implementations of KPFM, the AFM is operated in 'tapping' mode using a high spring constant, n-Si cantilever-tip assembly. In tapping mode, an oscillating voltage is applied to piezoelectric mounts that shake the cantilever at its resonant frequency. This induces a smooth, periodic physical oscillation of the tip, where the tip makes contact with the surface at the bottom of its oscillatory path. A laser reflected off of the cantilever tracks the amplitude of the oscillation, while a piezo with very fine vertical (z-direction) resolution (< 1 nm) is used to maintain a constant amplitude when the tip is in intermittent contact with a sample. As the probe is raster-scanned, z-piezo moves the tip assembly up and down in response to surface features, outputting a topography image. In KPFM, two scanning passes are made: first topography, then potential. Due to the weakness of van der Waals (vdW) at long range, the potential scan is performed in lift mode to ensure that the tip only feels electrostatic forces between tip and sample. The second pass is done at a constant lift height between 10-50 nanometers above the surface, which is maintained by driving the z-piezo using the data from the topography scan.

During the potential scan, instead of using the shake piezos as with the topography scan, an AC voltage is applied to the tip at or below its resonance frequency. When a CPD exists between tip and sample, this AC voltage causes the cantilever to oscillate,

and this oscillation disappears in the the absence of a CPD. The CPD can be determined through a feedback mechanism that applies a voltage to the tip, instigating a nulling effect on the electrostatic forces between the probe and sample. In this dissertation, a mode called amplitude modulation KPFM, or AM-KPFM, is used. Here, the nulling effect is measured by monitoring the disappearance of cantilever oscillation through its amplitude. There are some important limitations which must be discussed. First, one of the main assumptions of the CPD measurement is that one has an isolated set of parallel plates between tip and sample. However, the cone of the AFM tip and the cantilever itself have been shown to exert long-range electrostatic forces on the sample in AM-KPFM, thereby affect the amplitude of the tip during the potential scan.[9] This introduces a broadening effect on the potential that limits the resolution to 100-200 nm. An alternative method called frequency modulation KPFM (FM-KPFM), which uses the electrostatic force *gradient* rather than the force, avoids the effects of tip geometry, and is therefore preferable for quantitative measurements with high spatial resolution. However, FM-KPFM scanning must be carried out at a much slower rate than AM-KPFM in order to obtain high accuracy. For the work described in this dissertation, which studies the movement of ions within an ion-functionalized polymer layer, AM-KPFM is in fact preferable for its ability to be carried out on shorter timescales. A more detailed description of the experimental approach to studying dynamic processes with AM-KPFM is presented in Chapter 5 and its appendix.

2.4 Photoconductive Atomic Force Microscopy

Photoconductive atomic force microscopy (pc-AFM) is a technique for measuring the local photoconductivity of a sample using a contact-mode AFM probe as an electrode.[10,11] The current measured at a given location depends on the local charge mobility, carrier

density, and injection barriers at each electrode. For photoactive materials, photoconductivity results from an increase in photogenerated charge carriers (and an increase in mobility, when it is density-dependent). This photoconductivity reflects both the local absorption of light and the efficiency with which carriers are generated. When applied to the study of organic bulk heterojunction devices, different information can be learned about a system depending on the details of the pc-AFM experimental setup and the architecture of the test sample.

Generally speaking, pc-AFM is a method of measuring the current-voltage characteristics of a nanoscale solar cell device, where the local photocurrent reflects variations in blend composition, structural order, or vertical phase separation within the film. In most studies, samples are prepared in a manner keeping with solar cell devices, where the active layer is cast onto a conductive electrode. Depending on the work functions of the electrodes (the substrate and the conductive probe), the nanoscale device can function as a double- or single-carrier diode. In the work described in Chapter 4, the electrodes used in the study of a bulk heterojunction active layer are both of high work function, leading to a single carrier, hole-only device architecture. Furthermore, a reverse bias is applied, such that the system of AFM tip and sample effectively act as a photodetector. A lower limit to the magnitude of 'photodetectivity' is established through the measurement of dark current at the biases used in illuminated experiments. In the experiments shown in Chapter 4, the dark current lies at or below the detection limit of the AFM controller, suggesting that the analyses of photocurrent aren't adversely affected by injection (dark) current.

A detailed description of the principles connecting polarization-dependent photoconductivity to the structural details of a film is provided in Chapter 4. To provide a better understanding of the experiment, a schematic of the home-built optical setup used to provide high-purity, plane polarized light with a direction synchronized to the scanning

software is provided here in **Figure 2.3**. All of the procedures described here were carried out in conjunction with an Asylum MFP3D-BIO AFM instrument. Figure 2.3 shows a top-down view of the equipment used and its arrangement, which are laid out on a small optical table. While the setup can accommodate a number of different light sources, laser diodes are used for a number of reasons, including their relatively high intensity in a small package, low-voltage operation, and low cost. As shown in Figure 2.3, the laser diode is blocked by optional beam blockers, which can be used to switch between two different light sources. The light source is fed into a polarizer cube, where plane-polarized light is admitted along the beam line (or reflected, depending on the direction of approach) from the polarizer cube, and is directed into a liquid-crystalline retarder. Within this retarder, molecules reorient in response to an applied voltage, causing light passing through to be twisted (these molecules absorb very little visible light). Circularly polarized light emerges from the retarder, where the angle of the p- component depends on the original angle of the component and the bias applied (*i.e.*, the degree of twisting). A Fresnel rhomb then causes the light to undergo two internal, 45-degree reflections that remove most of the s-component introduced by the retarder, improving plane polarization purity. Finally, the light is directed toward a mirror and sent to an inverted microscope located below the AFM. The light source is then guided into position by carefully adjusting the location of the optical table relative to the microscopes light inlet. The retarder must be calibrated to determine voltages that provide the desired polarization angle at the location of the sample. The angle and purity of the polarization is initially measured prior to feeding into the microscope, but is later measured using a linear polarizer and photodiode placed at the sample stage. If any adjustments are made to the system, in particular to the position of any components on the table or the optical table itself, recalibration is necessary in order to accurately know the polarization purity, polarization angle, light intensity, etc.

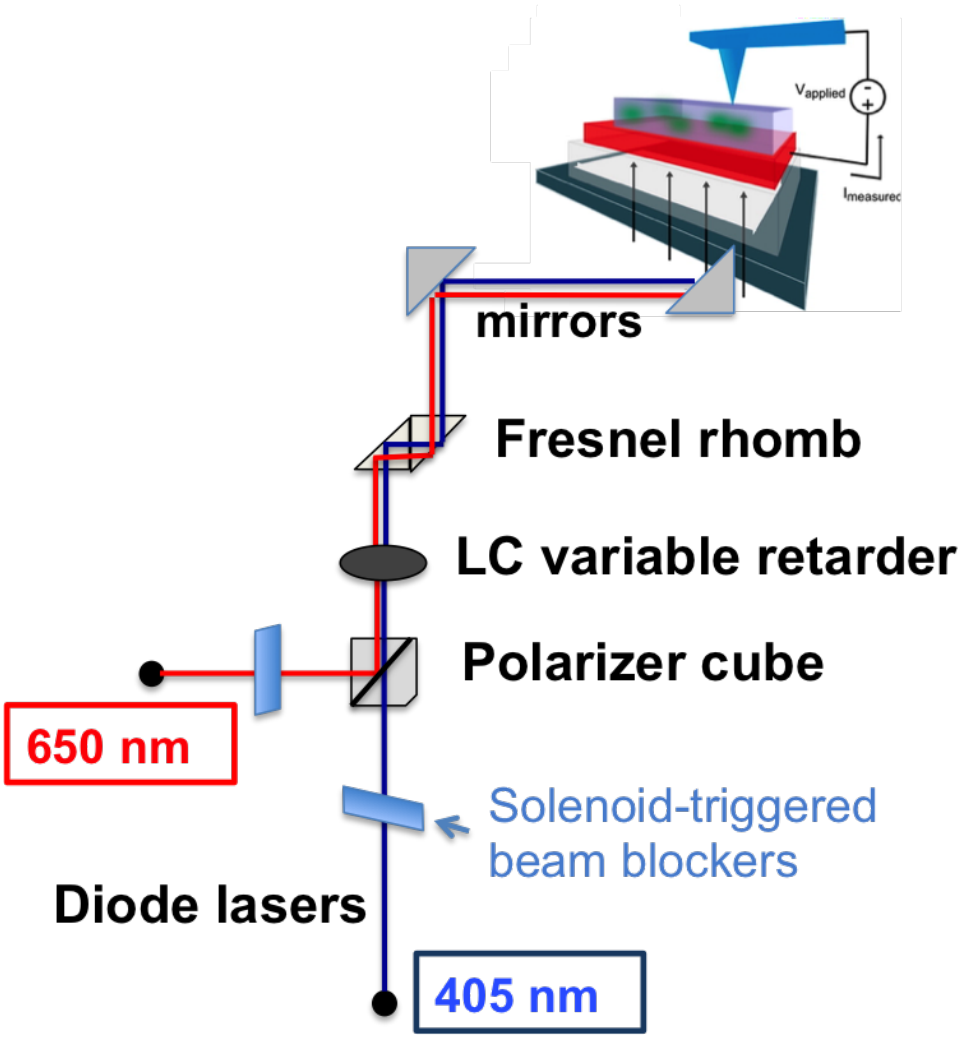

Figure 2.3: Schematic diagram of polarization optical setup used in Chapter 4.

Chapter 3

Understanding Open Circuit Voltage Loss Through the Density of States in Organic Bulk Heterojunction Solar Cells

Research in organic photovoltaics (OPVs) has recently brought about single-junction cells with >10% power conversion efficiency (PCE),[1–3] yet significant energy loss occurs even in high-performing systems due to low open-circuit voltage (V_{OC}). Theoretically, V_{OC} is limited by the photovoltaic gap, *i.e.*, the difference between the energy of the highest occupied molecular orbital of the donor ($HOMO_D$) and the lowest unoccupied molecular orbital of the acceptor ($LUMO_A$). In general, energy losses are attributed to the high rate of recombination in bulk-heterojunction (BHJ) blend systems. Compared to the energy of the charge transfer state (E_{CT}), which is effectively an in-situ measure of the photovoltaic gap that properly reflects energetic shifts that may occur upon blending, nearly all systems show energy losses ranging from 0.5 - 0.7 eV.[4,5] Understanding and

mitigating this large loss in voltage is a key component of reaching higher efficiency regimes. In addition to recombination, another factor that can vary significantly between systems and that is critical to the magnitude of loss is energetic disorder, i.e., broadening of the $HOMO_D$ and $LUMO_A$ density of states (DOS) distributions that results in a significant population of trap-like states well within the photovoltaic gap.[6–8] In order to properly quantify to what extent disorder and recombination contribute to the total loss, a comprehensive picture of donor and acceptor energetics is needed, but this remains difficult to obtain in working solar cells. Here, we address the problem of voltage loss through a detailed study of energetic disorder in BHJ solar cells utilizing small molecule donors. We demonstrate that losses due to energetic disorder and to the recombination strengths of the blends can be separated and quantified by combining techniques to establish a picture of the energetics over the full range of relevant states. With this approach, we obtain a better understanding of the complex factors leading to the observed V_{OC} in organic solar cells.

Organic semiconductors show a high degree of energetic disorder compared to their crystalline inorganic counterparts. This disorder is strongly influenced by structural features, where a wide array of intra- and intermolecular interactions in a morphologically diverse film gives rise to a broadening of the distribution of electronic states. In characterizing this disorder, there is some debate on whether a Gaussian or an exponential function—or a combination of these two—most appropriately describes the shape of the DOS.[9–23] Regardless of the functional shape, increased broadening of the DOS invariably pushes tail states further into the bandgap, and this leads to strong correlations between disorder and charge carrier mobility in diodes and organic field-effect transistors,[9] and between disorder and voltage losses in solar cells.[7,24] The picture is more complicated in BHJ devices, where the mixing of donor and acceptor components introduces donor-acceptor interfacial interactions, and can create a wide array of morphologies within

the active layer. Recent work has indeed shown that blends exhibit significant changes in energetics compared to neat films of donor and acceptor, and that the energetics depend significantly on blend ratio, thermal processing, and the relationship between donor and acceptor molecular structures.[24,25] These findings demonstrate that in order to understand the impact of disorder on V_{OC} with any certainty, in-situ measurements that determine the energetic distributions present within a given BHJ morphology are necessary. To demonstrate the general relationship between V_{OC} and disorder in a BHJ blend, **Figure 3.1** shows representative $HOMO_D$ and $LUMO_A$ distributions of varying disorder under open-circuit conditions. At forward bias conditions under illumination, the common Fermi level separates into hole and electron quasi Fermi levels, $E_{F,h}$ and $E_{F,e}$, respectively, and the energy separating these levels is equal to qV_{OC} at open-circuit, where q is the electronic charge.[6,26] Because the density of carriers in OPVs is typically low, only a relatively small portion of the DOS is occupied, causing $E_{F,e}$ and $E_{F,h}$ to reside far within the tail (Figure 3.1a). As the density obtained at open-circuit increases, $E_{F,e}$ and $E_{F,h}$ separate further, and thus V_{OC} also increases. The impact of varying disorder on V_{OC} is depicted for exponential DOS distributions in Figure 3.1b and for Gaussian distributions in Figure 3.1c. While the trend of higher disorder leading to lower V_{OC} is consistent, there are important differences in how these two models describe the effect of disorder and recombination on V_{OC} and thus they are not interchangeable.[7] Lange, et al,[24] recently demonstrated that the shape of the DOS tail can be differentiated experimentally from the dependence of V_{OC} on the hole (p) and electron (n) densities at open-circuit, where $V_{OC} \propto kT\ln(np)$ for a Gaussian and $V_{OC} \propto mkT\ln(np)$ for an exponential with $m \geq 1$. Although the DOS is more commonly described by the Gaussian disorder model, a number of recent reports have also shown an exponential DOS tail in polymer:fullerene blends, [18–20,22,23,27,28] based on measurements of charge carrier density at V_{OC}, transient absorption, and photothermal deflection spectroscopy. These results

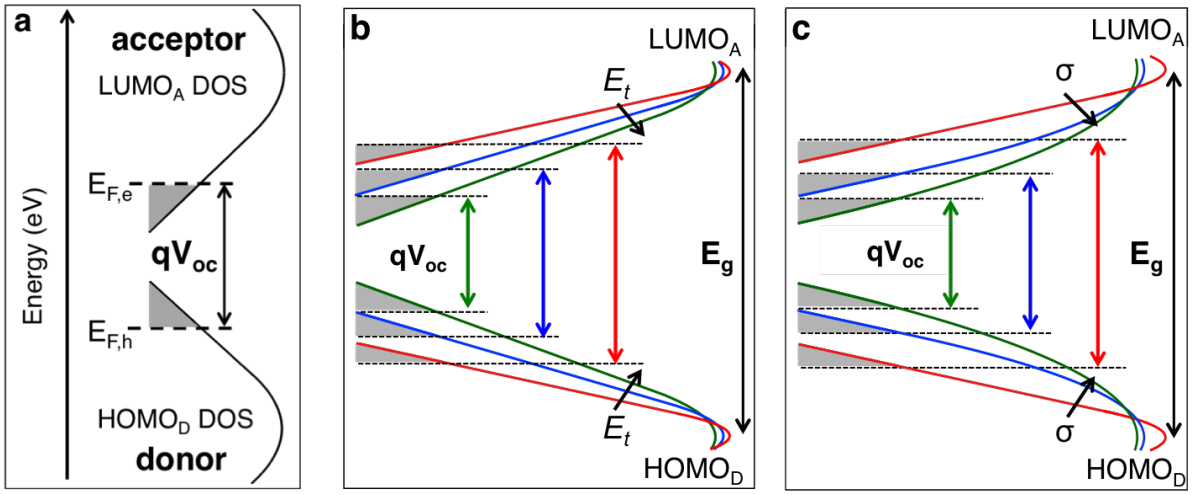

Figure 3.1: **a)** Illustration of density of states (DOS) distributions of donor HOMO ($HOMO_D$) and acceptor LUMO ($LUMO_A$) on log-lin scale. $E_{F,e}$ and $E_{F,h}$ are the electron and hole quasi Fermi energies at V_{OC}, respectively. Shaded areas show the portion of the DOS that is occupied by charge carriers at V_{OC}. **b)** $HOMO_D$ and $LUMO_A$ DOS distributions with a range of exponential widths, E_D and E_A, respectively, and a constant photovoltaic gap E_g. The corresponding V_{OC} is shown for each E_D (E_A) value to show the direct impact of disorder on V_{OC} at a constant charge carrier density. **c)** $HOMO_D$ and $LUMO_A$ DOS distributions with a range of σ values for fully Gaussian DOS distributions.

strongly suggest that a strictly Gaussian depiction of the DOS may neglect details that are critical for understanding V_{OC}. In this paper, all systems show behavior consistent with an exponential DOS tail, and so the focus will remain on the exponential model, which has been derived in detail elsewhere.[7,24] By adapting the expression derived in [24], the V_{OC} can be related to the occupation of exponential $HOMO_D$ and $LUMO_A$ distributions as:

$$qV_{OC} = E_g + E_A \ln\left(\frac{n}{N_0}\right) + E_D \ln\left(\frac{p}{P_0}\right) \tag{1}$$

where E_D/E_A is the characteristic width of the $HOMO_D/LUMO_A$distribution and P_0/N_0 is the maximum hole/electron density at $qV_{OC} = E_g$. Using the common assumption that electron and hole densities are equal ($n = p$) under illumination at open-circuit

conditions, and assuming $N_0 = P_0$, Equation (1) can then be simplified to obtain:

$$qV_{OC} = E_g + m_{DA}kT \ln\left(\frac{n_{oc}}{N}\right) \tag{2}$$

where n_{oc} is the single carrier density at open-circuit, $N = N_0 = P_0$, $m_{DA}kT$ is the combined donor-acceptor disorder ($m_{DA} \geq 2$), k is the Boltzmann constant, and T is temperature. A more detailed derivation of equations relating V_{OC} to the occupation of exponential (or Gaussian) DOS distributions is provided in Appendix A.1. In this work, we explore the connection between disorder and open-circuit voltage losses in organic bulk heterojunction solar cell devices by combining several techniques to determine bulk-averaged energetic distributions. We now provide a brief overview of our experimental approach. Voltage losses are considered relative to the photovoltaic gap, E_g, which we estimate here as the energy of the charge transfer state, E_{CT}. E_{CT} is shown elsewhere to serve as a reasonable estimate of the E_g in OPVs by the convergence of temperature-dependent V_{OC} and E_{CT} values at $T = 0\ K$.[5,29] E_{CT} is determined in this work from the analysis of external quantum efficiency (EQE) and electroluminescence (EL) spectroscopy. We combine current-voltage characteristics and impedance spectroscopy to obtain V_{OC} as a function of n_{oc}, where charge density is modulated by varying incident light intensity. These data are then fit to the model shown in Equation 2 to obtain the effective combined disorder in $HOMO_D$ and $LUMO_A$ tails within the range of carrier densities induced under illumination at open-circuit. To determine the respective contributions of $HOMO_D$ and $LUMO_A$ to the overall disorder, an analysis of band bending within the active layer is carried out using Kelvin probe, which is a capacitive, non-contact measurement that provides the work function or Fermi energy at the surface of a semiconductor. The band bending profile, $\phi(x)$, is experimentally determined from the thickness dependence of the Fermi energy, which is then modeled to estimate disorder

within the tail of the DOS distribution.[17] The work function of the electrode controls the type of carrier diffusing from the electrode into the film, thus allowing selective probing of disorder in $HOMO_D$ or $LUMO_A$.[24] Based on these characterizations, the effect of 'excess' disorder in donor and acceptor phases on the total voltage loss in each system is assessed, allowing further insight into the critical role that tail states play in limiting V_{OC}.

3.1 Molecular Structures and Energy Levels

To better facilitate a narrow focus, each of the systems chosen for this study has been previously characterized elsewhere. **Figure 3.2** shows the structures of the donor and acceptor materials used. The donors consist of three small-molecule derivatives with diketopyrrolopyrrole (DPP) cores that each obtain moderate device performance—2,5-dihexyl-3,6-bis[4-(5-hexyl-2,2′-bithiophene-5 yl)-phenyl]pyrrolo[3,4-c]-pyrrole-1,4-dione (**DPP1**), DPP—OT—3,6-bis(5-(benzofuran-2-yl)thiophen-2-yl)-2,5-bis(2-ethylhexyl) pyrrolo[3,4-c]pyrrole-1,4-dione (**DPP2**), and 2,5-di-(2-ethylhexyl)-3,6-bis-(5″-n-hexyl –[2,2′,5′,2″]terthiophen-5-yl)–pyrrolo[3,4-c]pyrrole-1,4-dione (**DPP3**)—and the high performing 7,7′-(4,4-bis(2-ethylhexyl)-4H-silolo[3,2-b:4,5-b′]dithiophene-2,6-diyl)bis(6-fluoro-4-(5′-hexyl-[2,2′-bithiophen]-5-yl)benzo[c][1,2,5]thiadiazole (**DTS**), which were blended with either phenyl-C_{71}-butyric acid methyl ester (**$PC_{71}BM$**) or the n-type polymer poly[N,N′-bis(2-octyldodecyl)-1,4,5,8-naphthalenedicarboximide-2,6-diyl]-alt-5,5′-(2,2′-bithiophene) (**N2200**). HOMO and LUMO energy levels estimated from photoelectron spectroscopy (PES) and optical bandgap measurements (E_{opt}), provided in Table 3.1, are obtained from the indicated reference.[30–36] Solar cell devices were prepared according to procedures reported elsewhere,[30–34] and as described in the Experimental section below. **Figure 3.3** shows J-V curves for all six blend systems measured at varying light intensities.

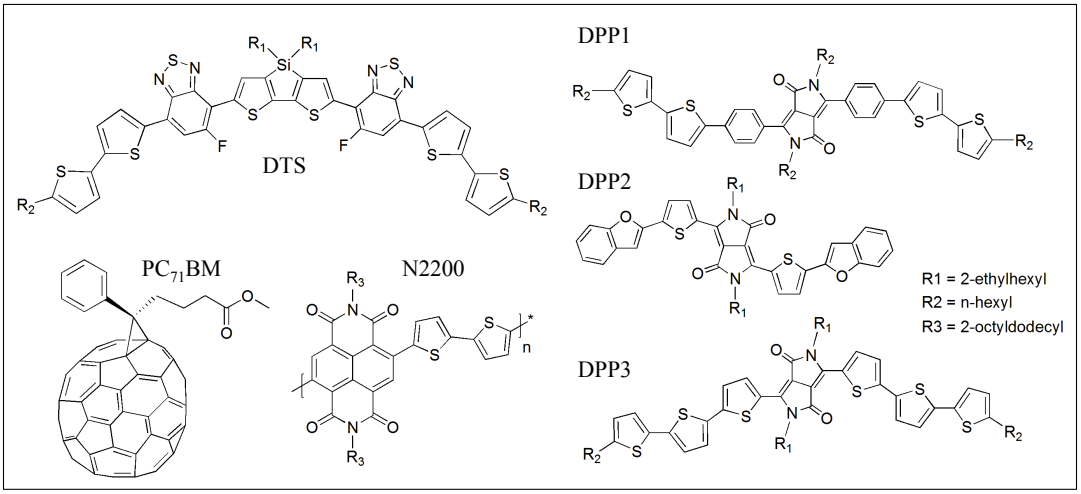

Figure 3.2: Chemical structures of donor and acceptor molecules.

Table 3.1: Energy Levels and Bandgaps of Donor and Acceptor Materials.

Material	HOMO (UPS)	LUMO (UPS + E_{opt})	LUMO (IPES)	E_{opt} (donor)	$E_{g,PES}$ (blend)	Reference
DPP1	-5.16	-3.32	–	1.84	1.35	[31]
DPP2	-5.20	-3.45	–	1.75	1.39	[30]
DPP3	-5.00	-3.4	–	1.60	1.19	[33]
DTS	-5.05	-3.5	–	1.55	1.24	[37]
$PC_{71}BM$	-5.90	–	-3.89	–	–	[35]
N2200	-5.45	-4.0	–	–	1.05	[36]

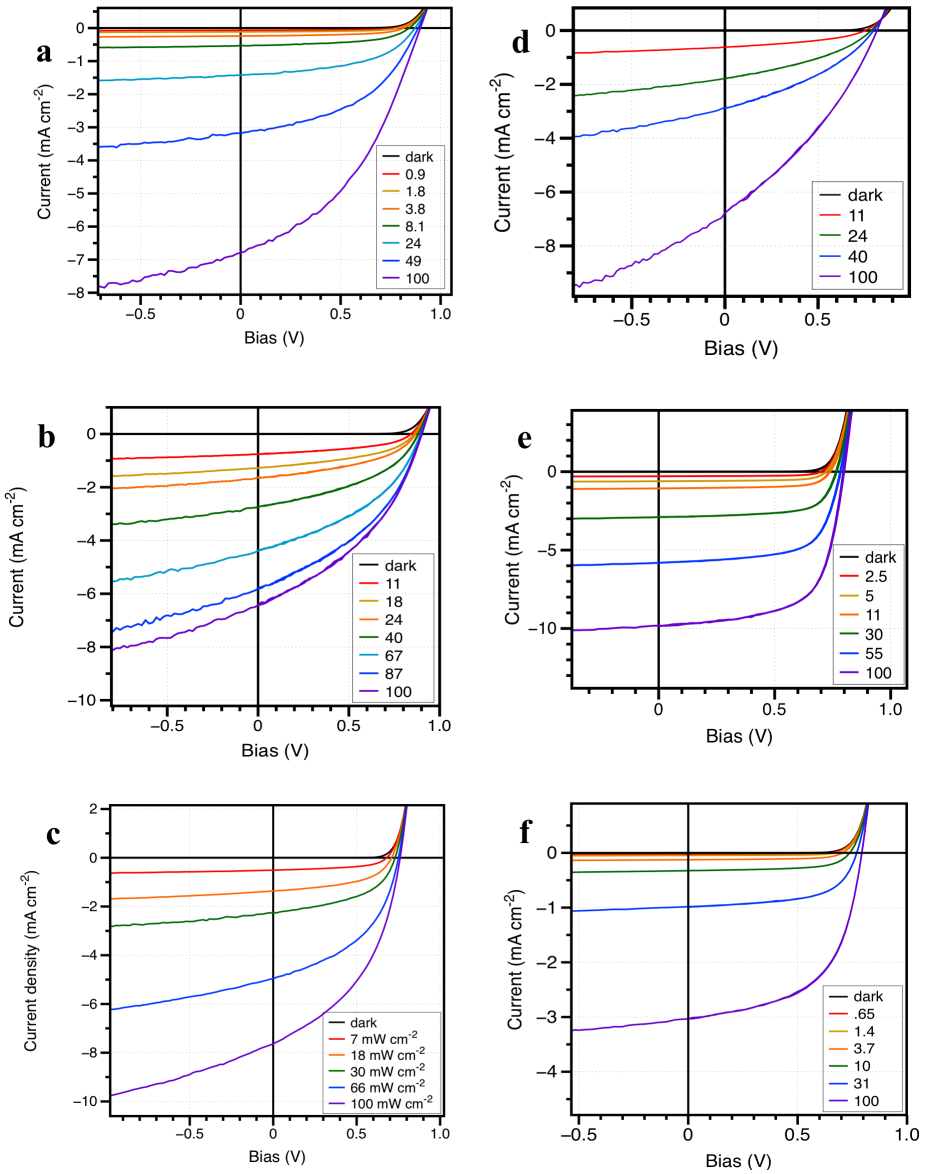

Figure 3.3: J-V curves taken over a range of inicident light intensities, indicated in units of mW cm^{-2}, for a) DPP1:$PC_{71}BM$, b) DPP2:$PC_{71}BM$, c) DPP3:$PC_{71}BM$, d) as-cast DTS:$PC_{71}BM$, e) optimized DTS:$PC_{71}BM$, and f) DTS:N2200 devices. The V_{OC} values obtained at 1-sun illumination are within $\pm$ 0.02 V of those previously reported using the same preparation conditions.

3.2 Donor-Acceptor Charge Transfer State Energies

To establish an in-situ estimate of the photovoltaic gap, E_{CT} was determined in each blend using the approach of Vandewal *et al.*, adapted from Marcus Theory, in which photocurrent produced from CT state absorption is described by the equation:

$$EQE(E) = \frac{f}{E\sqrt{4\pi\lambda kT}} \exp\left(\frac{-(E_{CT} + \lambda - E)^2}{4\lambda kT}\right). \quad (3)$$

Here, the parameter f represents the relative strength of CT state absorption, λ is the reorganization energy, and kT is the thermal voltage. **Figure 3.4** shows EQE spectra for each blend as measured by Fourier transform photoelectron spectroscopy (FTPS), which allows for sensitive detection of current produced from sub-bandgap spectral features. The data are fit with E_{CT}, λ, and f as free parameters, and the best fit is included on each of the spectra. Where possible, electroluminescence (EL) spectra were also included to improve accuracy in fitting λ, as the energy difference between absorption and emission maxima in Marcus Theory is equal to 2λ. It should be noted that, as a consequence of designing donor and acceptors to maximize V_{OC} by minimizing the offset between donor and acceptor LUMO levels, it is often the case that E_{CT} approaches the optical bandgap one of the blend components. This can cause the shoulder associated with CT absorption in the EQE spectrum to become partially or even completely obscured by current generation from singlet absorption, and this was observed particularly in the DTS:N2200 blend (Figure 3.4f). Due to the low band gap of N2200 ($\sim$ 1.45 eV), the absorption of the CT in DTS:N2200 could not be clearly resolved, and therefore a lower bound of 1.38 eV was estimated from combined analysis of EQE and EL measurements.

Figure 3.5a shows the E_{CT} values plotted as a function of V_{OC}, along with a linear

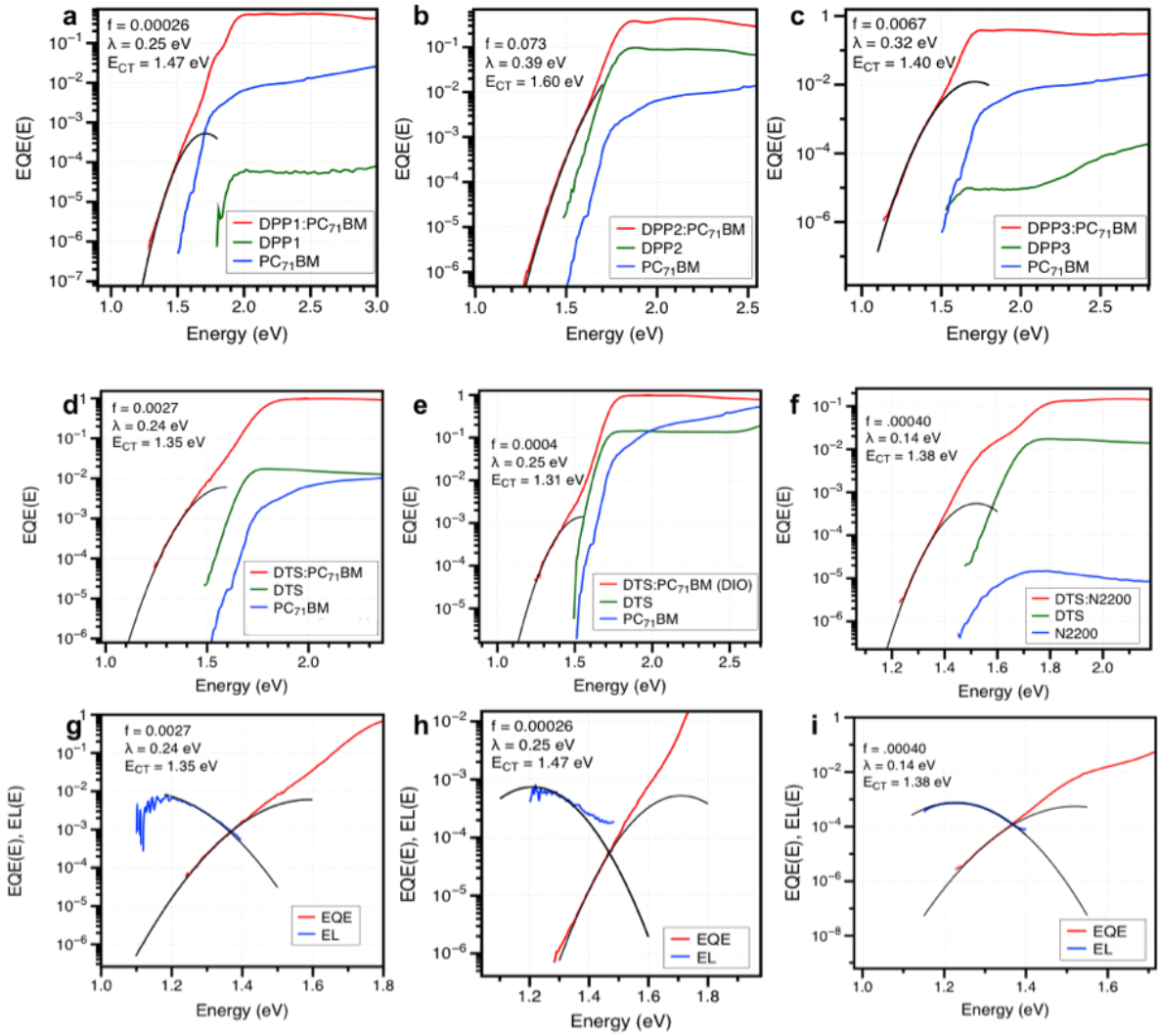

Figure 3.4: a-f) Neat and blend EQE spectra with fits to Equation (3) for all donor:acceptor systems, and comparison of blend EL and EQE spectra provided for (g) DTS:$PC_{71}BM$, (h) DPP1:$PC_{71}BM$, and (i) DTS:N2200. EL measurements are included in cases where the CTS emission could be obtained experimentally. Fits to the spectra are performed as previously described by Vandewal *et al.*,[29] where λ represents reorganization energy, f is the coupling constant, and E_{CT} is the midpoint between emission and absorption energy maxima of the charge transfer state. Fitting parameters f, λ, and E_{CT} are provided on each plot.

best fit line of $E_{CT} = qV_{OC} + 0.58eV$, which is similar to the trend observed elsewhere for polymer:fullerene blends.[4] Also plotted in Figure 3.5a are $E_{g,PES}$ and $\Delta E_{F,dark}$ as a function of V_{OC}, which are, respectively, the photovoltaic gap estimated ex-situ from

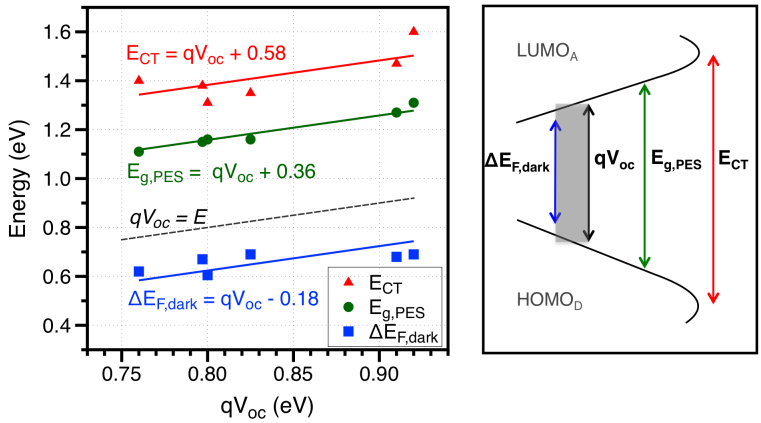

Figure 3.5: a) Plot of E_{CT}, E_g, PES, and $\Delta E_{F,dark}$ vs. the measured V_{OC} at 1 sun illumination. $\Delta E_{F,dark}$ is determined by Kelvin probe measurements of Fermi level in the dark for device films on high and low work function electrodes. b) Schematic showing the general relationship between the parameters in a) and $HOMO_D$ and $LUMO_A$ DOS distributions. The schematic is intended only to provide a general estimate for the position at which each measurement probes the DOS.

photoelectron spectroscopy (PES) of neat films from values in Table 3.1 and the difference in Fermi levels between blends cast on high and low work function electrodes measured by Kelvin probe. The significance of $\Delta E_{F,dark}$ is described in further detail below. These three measurements—E_{CT}, $E_{g,PES}$, and $\Delta E_{F,dark}$—reflect the respective regions of the $HOMO_D$ and $LUMO_A$ DOS distributions that determine them, as illustrated in **Figure 3.5b**: E_{CT} the center or maximum ($\sim 10^{20}\ cm^{-3}$), $E_{g,PES}$ the low-energy cutoff of $HOMO_D$ or $LUMO_A$ in the PES spectrum ($\sim 10^{19}\ cm^{-3}$), and $\Delta E_{F,dark}$ the deep tail of the DOS ($\sim 10^{15}\ cm^{-3}$). While on average all three values track well with the V_{OC}, individual variability from these trendlines can be significant. In particular, V_{OC} losses with respect to E_{CT}/q range from 0.51 V to 0.69 V for these cells. Highlighting this variability is not intended to suggest that these analyses are problematic. Rather, the variations result from differences in disorder and/or charge density at V_{OC} that are only apparent with further characterization, as will be illustrated herein.

3.3 Charge Carrier Density at V_{OC} from Capacitance-Voltage Measurements

In order to understand the variability in voltage loss, the distribution of electronic states within the photovoltaic bandgap was explored by measuring the relationship between charge carrier density and the V_{OC}. To modulate charge density together with V_{OC}, the incident light intensity was varied from 1 mW cm^{-2} to 100 mW cm^{-2} (Figure 3.3). At each light intensity, capacitance-voltage characteristics were obtained by impedance spectroscopy (IS) using a procedure similar to that reported by Proctor, *et al.*[33] **Figure 3.6** shows capacitance-voltage plots for varied light intensity, where the capacitance is extracted from a simple circuit model fit to a parallel RC circuit. The total device capacitance, C_{total}, is the sum of contributions from the geometrical capacitance of the electrodes, C_g, and the chemical capacitance of the active layer, C_μ. At far reverse bias in the dark, the active layer becomes depleted of charge and the total capacitance approaches C_g, becoming saturated at a voltage $V = V_{sat}$. The dielectric constant of each blend was then calculated from the geometric capacitance as $\epsilon_r = d/A \cdot C_g$, and will be discussed in further detail below. C_μ was calculated by subtracting the geometric capacitance from the total capacitance. Integrating C_μ with respect to voltage from V_{sat} to biases within the operating range then gives the bias-dependent charge density in the bulk of the active layer:

$$n(V) = n_{sat} + \frac{1}{qAL}\int_{V_{sat}}^{V} C_\mu \, dV \tag{4}$$

where A is the device area, L is the thickness of the active layer, and n_{sat} is the charge present within the device at V_{sat}. The chemical capacitance at V_{sat}, represented by C_{sat},

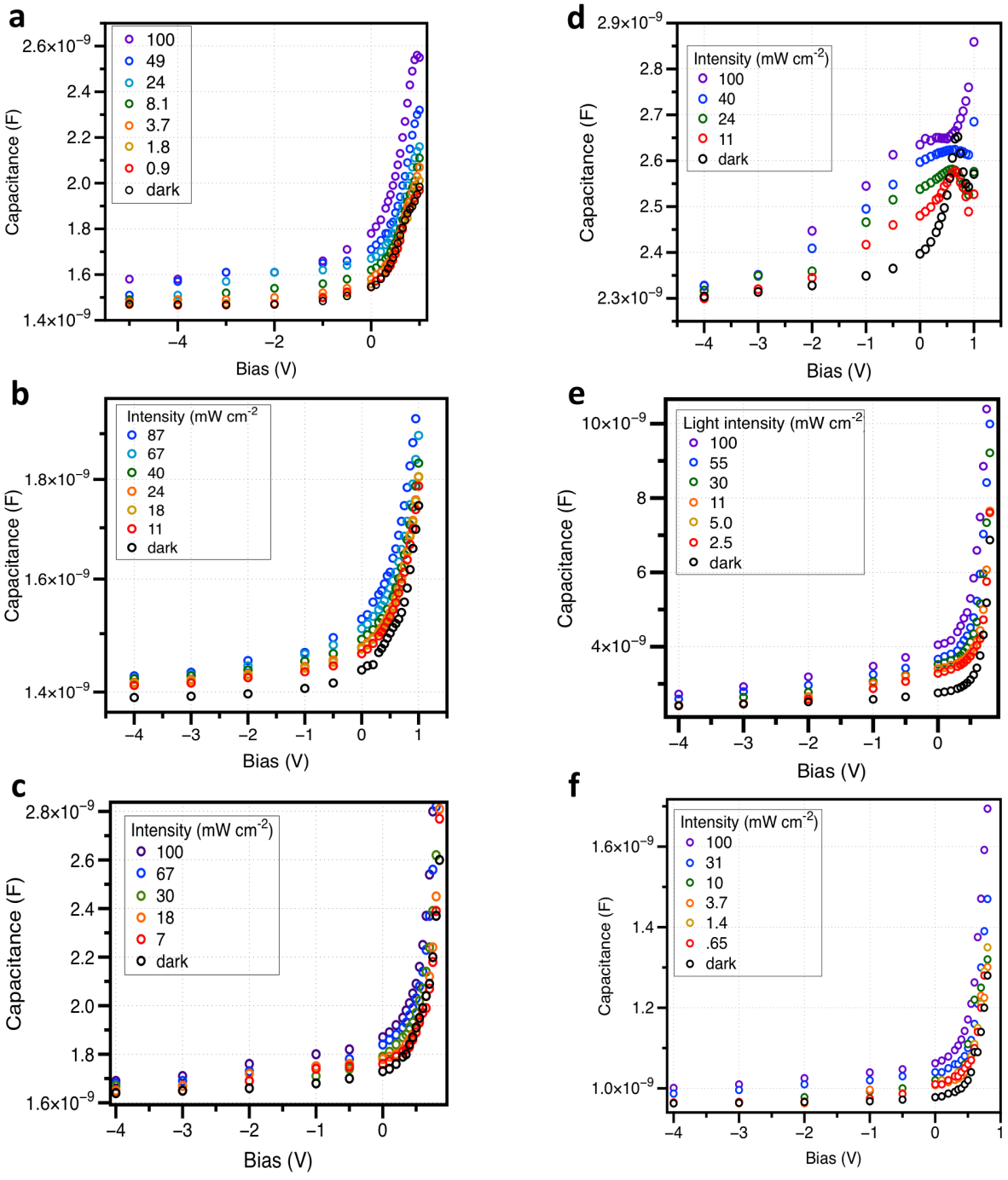

Figure 3.6: Capacitance measured by impedance spectroscopy plotted vs. voltage at varying light intensities and in the dark for a) DPP1:PCBM, b) DPP2:PCBM, c) DPP3:PCBM, d) DTS:PCBM 0% DIO, e) DTS:PCBM 0.4% DIO, and f) DTS:N2200.

is used to determine n_{sat} by the equation:

$$n_{sat} = \frac{1}{qAL} C_{sat} \cdot (V_{OC} - V_{sat}) \tag{5}$$

From the data in Figure 3.6, which represent C_{total}, C_{μ} was determined by subtracting C_g. The carrier density at open-circuit, n_{oc}, was then determined according to Equation (4) by numerical integration. **Figure 3.7** shows V_{OC} plotted against n_{oc} for each of the six solar cell blend systems (small symbols). Each data set is fit to Equation (2) (lines), and the value of the resulting disorder parameter, $m_{DA}kT$, is provided in Table 3.2. For all of the blends containing $PC_{71}BM$, good fits are obtained to an exponential dependence of V_{OC} on charge density. Also shown in Figure 3.7 are the values for $\Delta E_{F,dark}$ plotted at n_{dark}, given in the plot as large symbols. While these points are excluded from the fit to Equation (2), it is of note that they are found to be in good agreement with the extrapolated fits. The exponential tails can then reasonably be described out to n_{dark}, effectively increasing the measurable range of the DOS tail to densities about an order of magnitude lower. In order to observe a larger range of densities, the energetics were also analyzed at equilibrium, *i.e.*, in the dark with no applied DC bias. Even absent doping, the amount of charge present in organic solar cells (OSCs) at equilibrium is substantial, on the order of 10^{15} cm^{-3} in a 100 nm active layer with Ohmic contacts.[17,18,24] This is due to the spontaneous diffusion of electrons/holes from the low/high work function electrodes into tail states of the $LUMO_A$/$HOMO_D$. As with the illuminated impedance measurements, the charge density at equilibrium, n_{dark}, was determined by integrating the capacitance-voltage plot, described in further detail below. The difference in Fermi level between a device active layer cast on a low or a high work function electrode, as determined by Kelvin probe, corresponds to the approximate separation between the $LUMO_A$ and $HOMO_D$ distributions at n_{dark}, and is

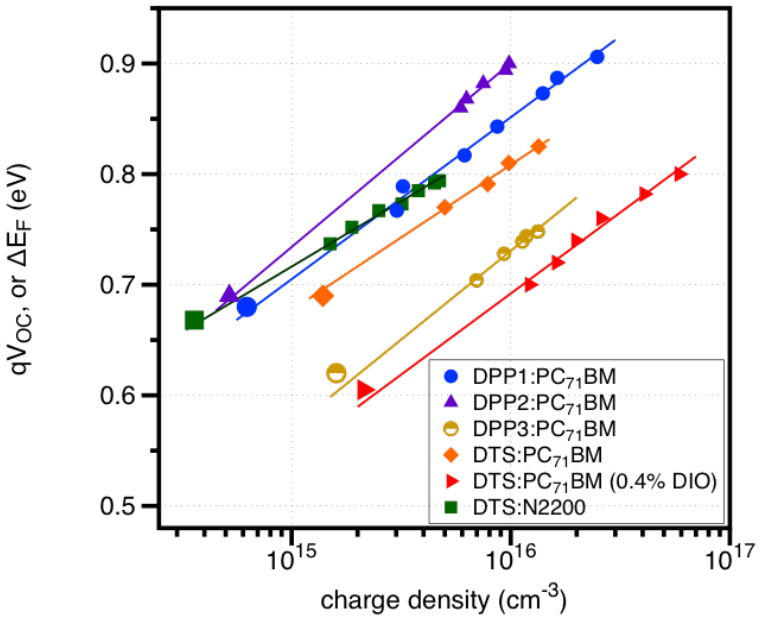

Figure 3.7: Open-circuit voltage vs. charge density for each of the blend systems. Each data set is fit to Equation (4). The larger points represent $\Delta E_{F,dark}$ plotted at n_{dark}, and provide an estimate of the energetics at the lower charge density present in the Kelvin probe experiment. The larger points were not included in the fit.

designated as $\Delta E_{F,dark}$. While the samples used to determine n_{dark} and $\Delta E_{F,dark}$ are not identical—active layers with and without an evaporated top contact, respectively—the single electrode architecture is expected to induce the same charge distribution for the charge carrier of interest, assuming that morphology remains similar and all electrodes are quasi-Ohmic.[24]

3.4 Quantifying Disorder from Band Bending Near Quasi-Ohmic Electrodes

To obtain a better understanding of the observed trends in $m_{DA}kT$, the disorder in the $HOMO_D$ and $LUMO_A$ DOS distributions was determined from Kelvin probe measurements of band bending. The band bending profile, $\phi(x)$, can be fit to an analytical

Table 3.2: E_{CT}, n_{oc}, and disorder parameters from impedance spectroscopy and Kelvin probe.

Blend	V_{OC} (V)	E_{CT} (eV)	$m_{DA}kT$ (meV)	n_{oc} (cm^{-3})	E_A (meV)	E_D (meV)
DPP1:$PC_{71}BM$	0.91	1.47	64 ± 3	2.5×10^{16}	27	40
DPP2:$PC_{71}BM$	0.91	1.60	72 ± 5	1.0×10^{16}	27	43
DPP3:$PC_{71}BM$	0.76	1.40	69 ± 5	1.4×10^{16}	41	26
DTS:$PC_{71}BM$	0.82	1.35	57 ± 3	1.3×10^{16}	25	31
DTS:$PC_{71}BM$(0.4% DIO)	0.80	1.31	64 ± 3	5.9×10^{16}	37	29
DTS:N2200	0.80	1.38	51 ± 2	4.7×10^{15}	24	26

model describing the transfer of charge from the electrode to the organic layer,[17,38] shown here for an exponential HOMO DOS distribution:

$$d = \sqrt{\frac{2E_D\epsilon_r\epsilon_0}{q^2N}}\exp\left(\frac{|\phi(d)|}{2E_D}\right)\times\arccos\left[\exp\left(-\frac{|\phi(d)|}{2E_D}\right)\right] \quad (6)$$

In Equation (6), d is the thickness of the film, E_D is the exponential disorder parameter in $HOMO_D$, ϵ_r is the relative dielectric constant, ϵ_0 is the vacuum permittivity, N is the DOS maximum, and $\phi(d)$ is the net potential shift at distance d from the electrode, where $\phi(0) = 0$. **Figure 3.8** shows the Fermi level of blends of DTS:$PC_{71}BM$ cast with and without DIO onto PEDOT:PSS or aluminum as a function of thickness. Fits to Equation (6) are shown as lines in Figure 3.8 with the disorder parameters obtained for donor (E_D) and acceptor (E_A) noted in the graph. The band bending data for the remaining blend systems are also provided in **Figure 3.9**, and the corresponding E_D and E_A values are summarized in Table 3.2. In these plots, it is important to note that the band bending profile can be highly sensitive to film thickness below 10 nm, and also that the assumption of a consistent morphology across all film thicknesses may

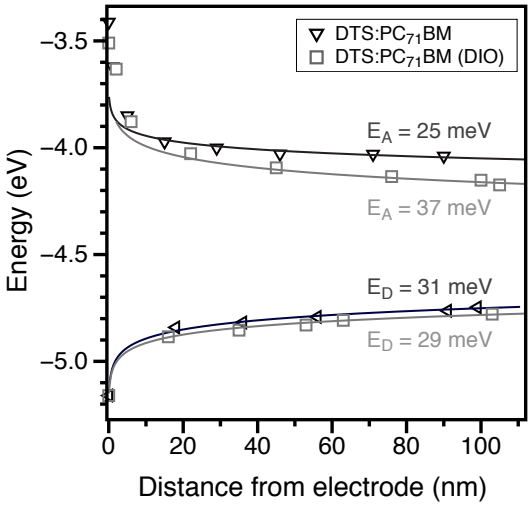

Figure 3.8: Band bending profile of DTS:$PC_{71}BM$ blends with and without additive, cast on PEDOT:PSS (WF = 5.2 eV) and aluminum (WF = 3.4 eV). The low WF of aluminum substrates is likely due to the presence of a thin surface oxide layer.

not always be correct.[12,24] Still, the trends in disorder provide useful insight into the relationship between blend morphology and the energetics in each phase (Figure 3.8), and for the contribution of donor or acceptor to the total disorder in each blend (Table 3.2). Furthermore, when the sum of E_D and E_A (E_{DA}) is plotted against $m_{DA}kT$ for each of the fullerene blend systems in **Figure 3.10**, the reasonable agreement between these values indicates that it is indeed the combined disorder of tail states in the donor and acceptor domains that determine the charge carrier density dependence of the V_{OC}.

Close inspection of the E_D and E_A values in Table 3.2 provides insight into the origins of energetic disorder across material systems. For example, in the most disordered blend system, DPP2:$PC_{71}BM$ ($m_{DA}kT$ = 72 meV), our results suggest that disorder in the donor material has a larger contribution to the total disorder and consequent voltage losses (E_D = 43 meV, Figure 3.9). In contrast, the disorder in the tail of the $PC_{71}BM$ LUMO in this blend is low (E_A = 27 meV), similar to what is observed in DTS:$PC_{71}BM$ without additive (E_A = 25 meV), DPP1:$PC_{71}BM$ (E_A = 27 meV), DPP2:$PC_{71}BM$ (E_A

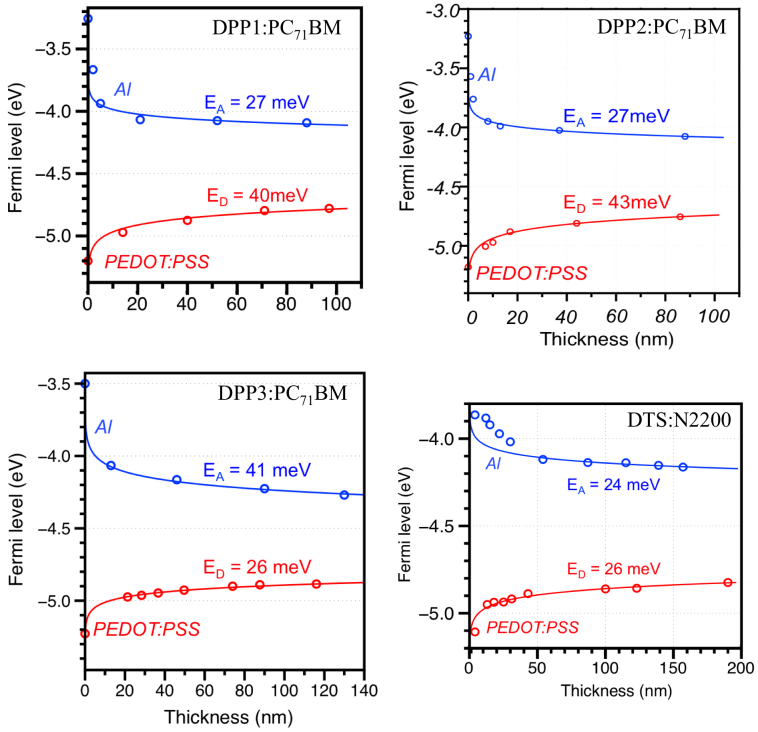

Figure 3.9: Thickness-dependent Fermi level measurements as determined by Kelvin probe for DPP1:$PC_{71}BM$, DPP2:$PC_{71}BM$, DPP3:$PC_{71}BM$, and DTS:N2200 blend films cast on Aluminum or PEDOT:PSS. Solid lines show fit to Equation (6) from the main text, and the resulting disorder parameter is shown on the graph. For DTS:N2200, a significant deviation is observed from the model at thicknesses below 50 nm, which was likely the result of either incomplete coverage or morphology that no longer resembles that found in the device.

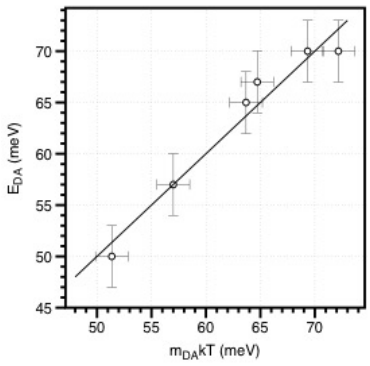

Figure 3.10: E_{DA}, the sum of E_D and E_A determined from thickness-dependent Kelvin probe measurements, plotted vs. $m_{DA}kT$ for each of the blend systems. The line $E_{DA} = m_{DA}kT$ is shown to guide the eye.

= 27 meV), and DTS:N2200 (E_A = 24 meV). These are considerably lower disorder values than the apparent disorder of the $PC_{71}BM$ LUMO in optimized DTS:$PC_{71}BM$ (E_A = 37 meV) or DPP3:$PC_{71}BM$ (E_A = 41 meV). Looking at the E_D values in Table 3.2, the disorder in the donor phase shows an opposing trend, with the exception of DTS:N2200, where E_D is higher for most blends with low E_A and is closer to kT when disorder in the fullerene phase increases. It is clear from the individual domain disorder values in Table 3.2 that donor and acceptor disorder values are not correlated, and that higher disorder in one phase may be enough to significantly limit the V_{OC}. In the most energetically ordered system, DTS:N2200, both E_D (26 meV) and E_A (24 meV) are near kT (26 meV), which is the theoretical lower limit for electronic disorder in an occupied exponential distribution of tail states. Thus, the V_{OC} of DTS:N2200 may not limited by disorder, but rather by the relatively low yield of free carriers at steady-state open-circuit conditions (see Figure 3.7).

3.5 Energetic Disorder and Fullerene Aggregation in DTS:$PC_{71}BM$

The DTS:$PC_{71}BM$ system provides an interesting case for examining the relationship between energetic disorder, processing conditions, and solar cell performance. The addition of DIO has been shown to increase DTS crystallinity, enhance phase separation, and improve PCE from about 2% to 7%.[37,39] Figure 3.8 shows that the value of E_A increases from about 25 meV to 37 meV, while E_D is slightly decreased from 31 meV to 29 meV. The lower energy $PC_{71}BM$ LUMO states apparent from Kelvin probe measurements are a signature of PCBM aggregation[24,25] and are consistent with the findings of Mukherjee *et al.* that showed $PC_{71}BM$ aggregation in DTS:$PC_{71}BM$ increases upon addition of

DIO.[40] The addition of lower lying states from aggregated fullerenes effectively increases the bulk electronic disorder as the acceptor phase becomes a mix of aggregated and unaggregated states. Ultimately, the effect of increased disorder and decreased E_{CT} on the V_{OC} of the DIO-processed DTS:$PC_{71}BM$ system relative to the 0% DIO DTS:$PC_{71}BM$ system is largely masked by the enhanced yield of free carriers at V_{OC}, with charge density increasing from 1.3×10^{16} cm^{-3} to 5.9×10^{16} cm^{-3}. Intriguingly, lower energy $PC_{71}BM$ LUMO tail states were also observed upon additive processing of blends containing the silaindacenodithiophene-based donor, p-SIDT$(FBTTh_2)_2$ (SIDT), shown in **Figure 3.11**. A correlation between improved photocurrent yield at short-circuit and the appearance of low-lying PCBM tail states can also be observed in SIDT:$PC_{71}BM$,[41] as well as elsewhere in polymer:fullerene systems.[24] Considering these observations in the context of recent

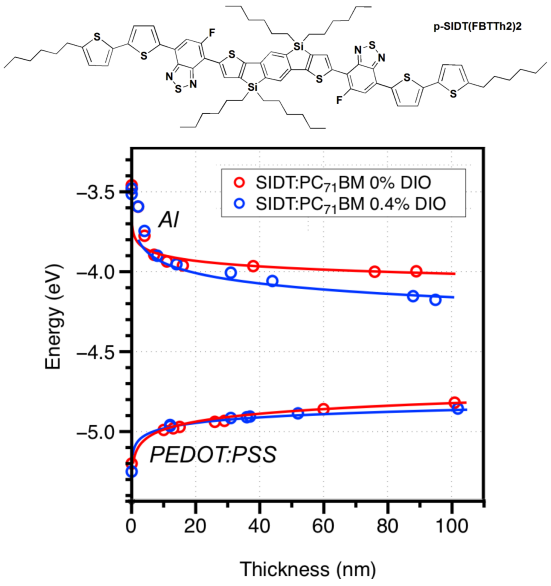

Figure 3.11: Molecular structure of p-SIDT$(FBTTh_2)_2$ (SIDT) and thickness-dependent Fermi level measurements as determined by Kelvin probe for SIDT:PCBM blends cast with and without 0.4% DIO on Aluminum or PEDOT:PSS. A significant decrease in V_{OC} from 1.00 V to 0.91 V reported in [41] for this system is likely attributable to the change in PCBM energetics that occurs here as a result of additive processing.

studies may help to clarify the role of the PCBM DOS distribution in the photogeneration

process. It was recently suggested by Gelinas and coworkers that fullerene aggregation is critical to improving the efficiency of additive-processed DTS:PCBM, as it facilitates ultrafast separation of the CT charge pair through delocalization of the electron across aggregated PCBM.[42] The lower energy PCBM LUMO states from aggregated PCBM apparent in Kelvin probe measurements thus may be linked to fast and efficient charge separation. The higher lying PCBM LUMO states seen in DTS:PCBM and SIDT:PCBM processed without additive also indicates that states near the donor-acceptor interface lie above those within fullerene aggregates, creating a favorable spatial inhomogeneity in the PCBM DOS tail, which would also be consistent with the argument that mixed phases and disorder in general help facilitate charge separation.[43–47] In this way, the nanoscale details of PCBM energetics may contribute to its unique success in OPVs, which is an important consideration in the continued search for suitable PCBM replacements. It should be noted, however, that the improved device performance associated with increased aggregation of PCBM evidently comes at the cost of increased energy losses attributable to disorder, as illustrated by our results.

3.6 Quantifying Voltage Losses from Disorder & Recombination

We have so far demonstrated that significant variations in disorder occur within the systems studied, and that trends in V_{OC} losses can be broadly understood as resulting from higher disorder and/or low charge carrier density at V_{OC}. To tie these obervations to the goal of reaching lower V_{OC} losses, it is then useful to quantify the impact of disorder on the loss in each system. To allow for this, we must first make the assumption that the function used to fit the DOS at low densities (Figure 3.7) applies to the entire DOS

tail. While this represents an extrapolation beyond the measured range, we will however demonstrate that it provides a remarkably consistent connection between energetic measurements, and is therefore a compelling way of considering V_{OC} loss with respect to the DOS in these OPVs. Treating E_{CT} as the effective upper limit to V_{OC},[5,29] we express the density dependence of V_{OC} (Figure 3.7) as loss relative to E_{CT}, or ΔV_{OC}. Equation (2) is rearranged to obtain ΔV_{OC} as a function of disorder ($m_{DA}kT$) and density (n_{oc}):

$$\Delta V_{OC} = m_{DA} kT \ln\left(\frac{n_{oc}}{N}\right) \tag{7}$$

In **Figure 3.12a**, ΔV_{OC} is plotted as a function of density and fit to Equation (8).

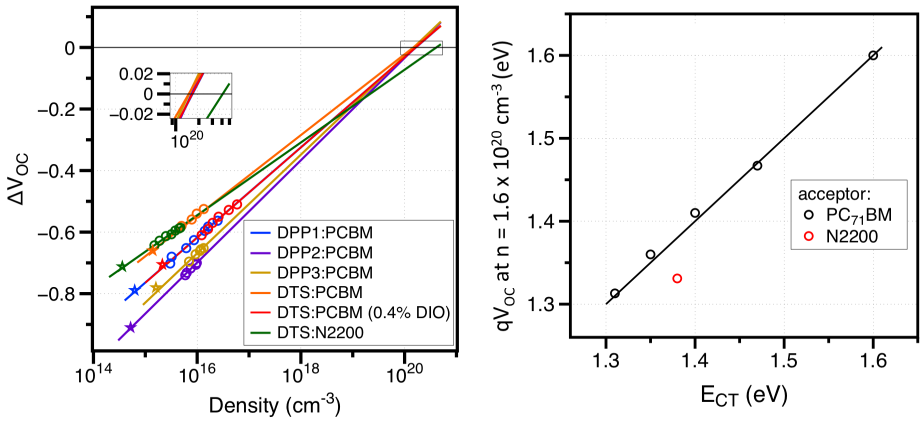

Figure 3.12: a) V_{OC} loss ΔV_{OC} relative to E_{CT} plotted as a function of n_{oc}, with fits to Equation (8) extrapolated to beyond $\Delta V_{OC} = 0$. b) Calculated value of qV_{OC} at $N = 1.6 \times 10^{20}$ cm^{-3} plotted against the measured E_{CT} value for each system. The data closely follow the line $qV_{OC}(N) = E_{CT}$ for the five blends containing $PC_{71}BM$, but DTS:N2200 deviates significantly due to a higher apparent value of N (4.1×10^{20} cm^{-3}).

Extrapolating these fits shows that the point of zero loss occurs over a small range of density values near 10^{20} cm^{-3}. All 5 blends containing $PC_{71}BM$ as acceptor appear to converge when $N = 1.6 \times 10^{20}$ cm^{-3}. By extrapolating the fits to Equation (2) in Figure 3.7 to this value, one obtains a qV_{OC} is within $\pm$ 0.01 eV of E_{CT} for all five

of these systems, as summarized by **Figure 3.12b**. Although a direct measurement of N is outside the scope of this work, it is remarkable that the value with the best correlation to the data is consistent with analysis of temperature-dependent current-voltage characteristics in neat organic semiconductor films.[10,11,14] To illustrate the relative impact of variations in disorder and recombination, we calculate how much the 'excess' disorder contributes to ΔV_{OC}. While it is not possible to deconvolute the effect that low-lying tail states may also have on the rate of recombination, we consider instead how much V_{OC} is lost at 1-sun illumination simply due to the difference between the observed disorder and a proposed minimum disorder. Here, we take the minimum exponential width of a HOMO or LUMO tail state distribution to be the thermal voltage, kT, and thus the minimal slope of V_{OC} vs density in a semilog plot is equal to $2kT$. We designate the contribution of excess disorder to ΔV_{OC} as $V_{disorder}$, and subtract this contribution from ΔV_{OC} to yield the remainder of the loss, V_{rec}. V_{rec} then represents the voltage loss determined by the balance between generation and recombination rates at V_{OC} given minimal disorder. Details of these calculations are provided in Appendix A.2, and values for $V_{disorder}$ and V_{rec} are provided in **Table 3.3**. From this treatment, we see that a system with minimal disorder such as DTS:N2200 suffers no additional disorder-induced loss, while DPP2:$PC_{71}BM$ suffers about 0.2 V in additional V_{OC} loss due to a high degree of disorder in the donor phase (see Table 3.2). Previous reports have found that in most OPV systems bimolecular recombination is the dominant charge recombination mechanism at open circuit.[7,26,48] It follows that the recombination rate, R, can be described as $R = \gamma n_{oc}^2$, where γ is the bimolecular recombination rate coefficient. At open-circuit, generation equals recombination (G = R), therefore the loss due to

recombination can be expressed as:[7]

$$V_{rec} = kT \ln\left(\frac{G}{\gamma N^2}\right) \tag{8}$$

The logarithmic dependence of V_{rec} on G and γ indicates that only very large changes in the kinetics of generation and recombination will have substantial effects on the V_{OC}, which helps to explain the relatively small range of voltage losses reported to date in OPV systems.[4] To better understand the origin of V_{rec} in the systems studied here, G and γ were estimated from the saturated photocurrent and n_{oc} accounting for voltage dependent generation,[34,48] following previously described procedures[34] (see Appendix A.3). The generation rate varies by a factor of ∼3.6 between systems, while γ is found to range by a factor of ∼40, as shown in Table 3.3. From this analysis, it is evident that it is primarily the very low γ in the DIO processed DTS:$PC_{71}BM$ system that enables the relatively low V_{rec}. While good agreement is found here between previous reports of γ in DPP3:$PC_{71}BM$ and DTS:$PC_{71}BM$,[33,34] it is worth noting that higher γ values for the DTS:$PC_{71}BM$ (DIO) system have also been reported.[34,49] The origin of the discrepancy is unclear, although contrast to previous reports, the γ value for DTS:$PC_{71}BM$ (DIO) reported in this study is consistent with analytical and empirical models that describe the relatively high fill factor and low V_{OC} losses in this system.[7,50]

A high rate of bimolecular recombination is the primary source of energy loss in all the systems studied here, leaving considerable room to improve V_{OC} by reducing this rate. Increasing the high frequency dielectric constant has been proposed as a way to dramatically reduce γ at open-circuit,[51] and it is now emerging as a popular strategy for increasing V_{OC}. While a conclusive model that describes how the dielectric constant affects solar cell performance and V_{OC} has not yet been demonstrated, increasing ϵ_r is at least expected to correlate with decreased voltage loss. This correlation is indeed

Table 3.3: Voltage loss relative to E_{CT} at 1 sun illumination (ΔV_{OC}), voltage losses due to disorder ($V_{disorder}$) and recombination (V_{rec}), rates of generation (G) and recombination (γ) at open-circuit, and the relative dielectric constant (ϵ_r) of each blend.

Blend	ΔV_{OC} (V)	$V_{disorder}$ (V)	V_{rec} (V)	G (10^{21} cm^{-3} s^{-1})	γ (cm^{-3} s^{-1})	ϵ_r
DPP1:$PC_{71}BM$	0.57	0.12	0.45	3.2	5.2×10^{-12}	3.7
DPP2:$PC_{71}BM$	0.69	0.20	0.49	3.1	3.1×10^{-11}	3.2
DPP3:$PC_{71}BM$	0.57	0.17	0.47	4.2	2.4×10^{-11}	3.5
DTS:$PC_{71}BM$	0.57	0.06	0.47	6.6	3.7×10^{-11}	3.7
DTS:$PC_{71}BM$(DIO)	0.10	0.10	0.41	8.7	2.5×10^{-12}	4.1
DTS:N2200	0.58	∼0	0.58	2.3	9.8×10^{-11}	2.8

observed when V_{rec} is plotted vs. ϵ_r in **Figure 3.13a**, where a linear best fit to the data has a slope of -0.088 V, suggesting a strong decrease in V_{OC} loss with dielectric over the measured regime of ϵ_r values. A corresponding exponential decrease in γ with ϵ_r can also be seen in **Figure 3.13b**, but it is important to note that the effect of morphology and other material properties cannot be fully distinguished from the effect of dielectric in this case. In fact, one of the factors correlated to a reduction in the rate of recombination, increased PCBM aggregation, may also lead to an increased blend dielectric, and it is therefore not possible to establish any causal relationship here between V_{rec} and ϵ_r. Still, a qualitatively similar result was observed by Cho *et al.*, when increasing ϵ_r in a donor polymer from 3.9 to 5 through the addition of polar side-chains.[52] They observed an 80 mV increase of V_{OC} in bilayer solar cells with increased ϵ_r, which they attributed to a significant increase in carrier lifetime. In our case, the fit to V_{rec} vs. ϵ_r (Figure 3.13b) predicts an increase of 98 mV over the same interval, and after accounting for differences in the rate of generation (see Figure A.2), a 70 mV increase is predicted for the same change in ϵ_r. While the correlation between these results is encouraging, future work will

focus on extending the analysis to high-dielectric blends ($\epsilon_r \geq 5$), and will also decouple the effects of morphology and ϵ_r on the rate of recombination through the study of bilayer devices. It should be noted that one of the demonstrated methods for increasing ϵ_r—introducing polar moieties onto side chains—has the potential to increase energetic disorder by disrupting side chain ordering, and therefore properly understanding the sources of voltage loss in a device is critical when assessing the effect of ϵ_r on V_{OC}.

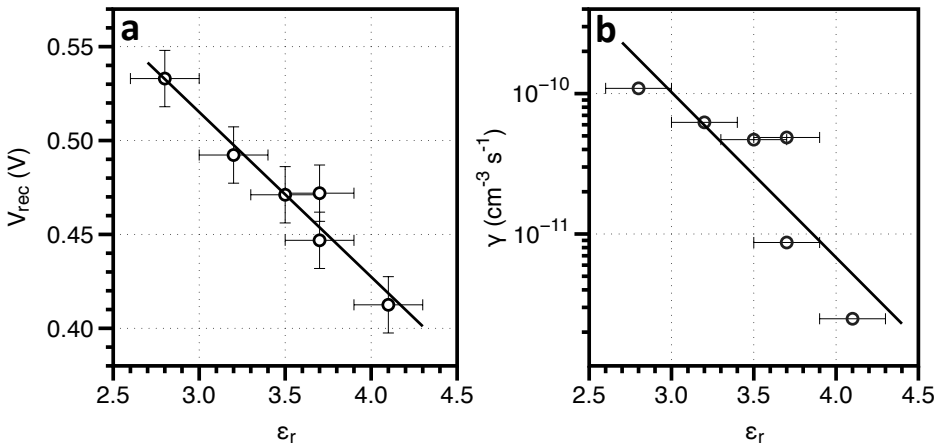

Figure 3.13: a) V_{rec} plotted vs. dielectric constant, ϵ_r, with linear best fit (slope = -0.088 V). b) Recombination rate, γ, plotted vs. ϵ_r with exponential fit to guide the eye. The largest deviation from the fit occurs for DTS:$PC_{71}BM$ without DIO, for which, unlike all other systems, morphology is not optimized through annealing or additive processing.

3.7 Conclusions

In this work, the density of states was characterized in a number of small molecule BHJ solar cells, allowing voltage loss to be quantitatively separated into contributions due to excess disorder and to recombination. Kelvin probe measurements revealed that disorder in donor and acceptor phases was in many cases not correlated, and that disorder in just one of the blend components could lead to significantly reduced V_{OC}. Interestingly, $PC_{71}BM$ aggregation was tied to increased energetic disorder, but also to a concomitant

decrease in the rate of recombination, suggesting that there may be a trade-off between an improved yield of free carriers and disorder-induced V_{OC} loss. The rate of charge carrier recombination at open-circuit was estimated to vary by two orders of magnitude among the systems studied, leading to significant variation in voltage loss from ca. 0.41 to 0.58 V after accounting for the effect of energetic disorder. While disorder was found to contribute as much as 0.2 V of V_{OC} loss in the most extreme example, the relative absence of disorder-induced loss in some systems showed that disorder is not a limiting factor in every case. In the highest performing system, DTS:$PC_{71}BM$ processed with 0.4% DIO, a low voltage loss of 0.51 V compared to E_{CT} was found to be a result of both low energetic disorder and a low rate of recombination. The low recombination in this system was linked not only to the phase separation, fullerene aggregation, and donor crystallinity shown elsewhere for this system, but also to the high dielectric constant of the blend. Comparing all systems, increasing dielectric constant was concomitant with a linear decrease in recombination-induced voltage loss and an exponentially decreasing rate of bimolecular recombination.

3.8 Experimental Section

Film and device preparation: All films were prepared on Corning 1737 glass substrates patterned with 140 nm of ITO, which were scrubbed with detergent and sonicated in acetone and isopropanol. Solar cell device substrates were treated with O_2-plasma for 5 minutes, coated with a 40 nm PEDOT:PSS (Clevios P VP AI 4083) layer, and annealed in air for 20 minutes at 140 °C. Active layers were prepared in a N_2-filled glovebox with solution conditions reported elsewhere.[30–34] For devices with the donor DTS, a 15 nm layer of Ca was thermally evaporated before depositing a 100 nm Al cathode. All other devices utilized only a 100 nm aluminum layer as the top contact. Cathodes were defined by shadow

mask to yield device areas of 6.0 mm^2 for DTS:$PC_{71}BM$ prepared with 1,8-diiodooctane and 4.5 mm^2 for all others. Films for Kelvin probe measurements were prepared concurrently with devices from the same solutions and cast on either PEDOT:PSS or 100 nm aluminum substrates using the same post-deposition treatments. For Kelvin probe band bending studies, thickness was varied by serial dilution. Layer thicknesses were measured using an Ambios XP-100 stylus profilometer. $PC_{71}BM$ was purchased from Nano-C (Westwood, MA, USA), and used as received. N2200 was provided by Polyera Corporation (Skokie, IL, USA), also used as received. DPP1, DPP2, DPP3, and DTS were prepared in house according to procedures reported elsewhere.[30,37,53,54]

Solar cell device J-V: Device characteristics were measured under illumination by a simulated 100 mW cm^{-2} AM1.5G light source using a 300 W Xe arc lamp with an AM 1.5 global filter. Solar-simulator irradiance was calibrated using a standard silicon photovoltaic with a protective KG1 filter calibrated by the National Renewable Energy Laboratory. EQEs were determined using a 75W Xe source, monochromator, optical chopper, lock-in amplifier, and a National Institute of Standards and Technology calibrated silicon photodiode was used for power-density calibration. Light intensity was varied with neutral density filters.

Impedance spectroscopy: Impedance of solar cell devices was measured using a Solartron 1260 impedance analyzer, applying an AC amplitude of 20mV from 50Hz to 1MHz, with backing DC biases from -4 V to 1 V. The frequency dependence of the real and imaginary components of impedance was then used to determine both the spectral capacitance and the capacitance from equivalent circuit analysis. J-V characteristics were collected before and after each set of impedance measurements to ensure the stability of the V_{OC}. Care was taken to ensure that the solar cell devices were not affected by leakage currents, which can dominate behavior at low light intensities when the shunt resistant is low.[55]

Kelvin probe measurements: Contact potential difference (CPD) values were measured

with an SKP 5050 (KP Technology, UK) Kelvin probe in an N_2-filled glovebox (<1 ppm O_2) with a stainless steel tip 2 mm in diameter. CPD values are obtained from the average of 144 points taken over a 1.2 mm × 1.2 mm scanning area. The probe work function was calibrated against freshly cleaved highly-oriented pyrrolitic graphite (HOPG), which was assumed to have a work function of 4.6 eV.[56]

Fourier transform external quantum efficiency: External quantum efficiency (EQE) for all solar cells was measured using a 75 W Xe light source, monochromator, optical chopper, and a lock-in amplifier. Power-density calibration of the EQE characteristics was achieved using a calibrated National Institute of Standards and Technology silicon photodiode. For the sub-bandgap EQE, higher sensitivity settings were used with a longer time delay between measurement points.

Electroluminescence Spectroscopy: Electroluminescence (EL) spectra were measured using a Si CCD array detector cooled to -70 °C. Emission from the devices was aligned to the CCD entrance slit with a series of focusing lenses. In all cases, spectra were collected at the lowest applied bias with detectable emission. All emission spectra were corrected for detector sensitivity with a black body spectrum.

References

1. Kan, B.; Zhang, Q.; Li, M.; Wan, X.; Ni, W.; Long, G.; Wang, Y.; Yang, X.; Feng, H.; Chen, Y. *J. Am. Chem. Soc.* **2014**, *136*, 15529–15532.

2. Liu, Y.; Zhao, J.; Li, Z.; Mu, C.; Ma, W.; Hu, H.; Jiang, K.; Lin, H.; Ade, H.; Yan, H. *Nat Commun* **2014**, *5*, DOI: 10.1038/ncomms6293.

3. Kan, B. et al. *J. Am. Chem. Soc.* **2015**, DOI: 10.1021/jacs.5b00305.

4. Graham, K. R.; Erwin, P.; Nordlund, D.; Vandewal, K.; Li, R.; Ngongang Ndjawa, G. O.; Hoke, E. T.; Salleo, A.; Thompson, M. E.; McGehee, M. D.; Amassian, A. *Adv. Mater.* **2013**, *25*, 6076–6082.

5. Vandewal, K.; Tvingstedt, K.; Gadisa, A.; Inganäs, O.; Manca, J. V. *Nat Mater* **2009**, *8*, 904–909.

6. Bisquert, J.; Garcia-Belmonte, G. *J. Phys. Chem. Lett.* **2011**, *2*, 1950–1964.

7. Blakesley, J. C.; Neher, D. *Phys. Rev. B* **2011**, *84*, 075210.

8. Maurano, A.; Hamilton, R.; Shuttle, C. G.; Ballantyne, A. M.; Nelson, J.; O'Regan, B.; Zhang, W.; McCulloch, I.; Azimi, H.; Morana, M.; Brabec, C. J.; Durrant, J. R. *Adv. Mater.* **2010**, *22*, 4987–4992.

9. Kuik, M.; Wetzelaer, G.-J. A. H.; Nicolai, H. T.; Craciun, N. I.; De Leeuw, D. M.; Blom, P. W. M. *Adv. Mater.* **2014**, *26*, 512–531.

10. Craciun, N. I.; Wildeman, J.; Blom, P. W. M. *Phys. Rev. Lett.* **2008**, *100*, 056601.

11. Pasveer, W. F.; Cottaar, J.; Tanase, C.; Coehoorn, R.; Bobbert, P. A.; Blom, P. W. M.; de Leeuw, D. M.; Michels, M. A. J. *Phys. Rev. Lett.* **2005**, *94*, 206601.

12. Oehzelt, M.; Koch, N.; Heimel, G. *Nat Commun* **2014**, *5*, DOI: 10.1038/ncomms5174.

13. Torricelli, F.; Kovács-Vajna, Z. M.; Colalongo, L. *Organic Electronics* **2009**, *10*, 1037–1040.

14. Fishchuk, I. I.; Kadashchuk, A. K.; Genoe, J.; Ullah, M.; Sitter, H.; Singh, T. B.; Sariciftci, N. S.; Bässler, H. *Phys. Rev. B* **2010**, *81*, 045202.

15. Pingel, P.; Neher, D. *Phys. Rev. B* **2013**, *87*, 115209.

16. Oelerich, J. O.; Huemmer, D.; Baranovskii, S. D. *Phys. Rev. Lett.* **2012**, *108*, 226403.

17. Lange, I.; Blakesley, J. C.; Frisch, J.; Vollmer, A.; Koch, N.; Neher, D. *Phys. Rev. Lett.* **2011**, *106*, 216402.

18. Shuttle, C. G.; Treat, N. D.; Douglas, J. D.; Fréchet, J. M. J.; Chabinyc, M. L. *Adv. Energy Mater.* **2012**, *2*, 111–119.

19. MacKenzie, R. C. I.; Shuttle, C. G.; Chabinyc, M. L.; Nelson, J. *Adv. Energy Mater.* **2012**, *2*, 662–669.

20. Gong, W.; Faist, M. A.; Ekins-Daukes, N. J.; Xu, Z.; Bradley, D. D. C.; Nelson, J.; Kirchartz, T. *Phys. Rev. B* **2012**, *86*, 024201.

21. MacKenzie, R. C. I.; Kirchartz, T.; Dibb, G. F. A.; Nelson, J. *J. Phys. Chem. C* **2011**, *115*, 9806–9813.

22. Beiley, Z. M.; Hoke, E. T.; Noriega, R.; Dacuña, J.; Burkhard, G. F.; Bartelt, J. A.; Salleo, A.; Toney, M. F.; McGehee, M. D. *Adv. Energy Mater.* **2011**, *1*, 954–962.

23. Tachiya, M.; Seki, K. *Phys. Rev. B* **2010**, *82*, 085201.

24. Lange, I.; Kniepert, J.; Pingel, P.; Dumsch, I.; Allard, S.; Janietz, S.; Scherf, U.; Neher, D. *J. Phys. Chem. Lett.* **2013**, *4*, 3865–3871.

25. Sweetnam, S.; Graham, K. R.; Ngongang Ndjawa, G. O.; Heumüller, T.; Bartelt, J. A.; Burke, T. M.; Li, W.; You, W.; Amassian, A.; McGehee, M. D. *J. Am. Chem. Soc.* **2014**, *136*, 14078–14088.

26. Garcia-Belmonte, G.; Bisquert, J. *Applied Physics Letters* **2010**, *96*, 113301.

27. Street, R. A.; Krakaris, A.; Cowan, S. R. *Adv. Funct. Mater.* **2012**, *22*, 4608–4619.

28. Foertig, A.; Rauh, J.; Dyakonov, V.; Deibel, C. *Phys. Rev. B* **2012**, *86*, 115302.

29. Vandewal, K.; Gadisa, A.; Oosterbaan, W. D.; Bertho, S.; Banishoeib, F.; Van Severen, I.; Lutsen, L.; Cleij, T. J.; Vanderzande, D.; Manca, J. V. *Adv. Funct. Mater.* **2008**, *18*, 2064–2070.

30. Walker, B.; Tamayo, A. B.; Dang, X.-D.; Zalar, P.; Seo, J. H.; Garcia, A.; Tantiwiwat, M.; Nguyen, T.-Q. *Advanced Functional Materials* **2009**, *19*, 3063–3069.

31. Lin, J. D. A.; Liu, J.; Kim, C.; Tamayo, A. B.; Proctor, C. M.; Nguyen, T.-Q. *RSC Adv.* **2014**, *4*, 14101–14108.

32. Li, Z.; Lin, J. D. A.; Phan, H.; Sharenko, A.; Proctor, C. M.; Zalar, P.; Chen, Z.; Facchetti, A.; Nguyen, T.-Q. *Adv. Funct. Mater.* **2014**, *24*, 6989–6998.

33. Proctor, C. M.; Kim, C.; Neher, D.; Nguyen, T.-Q. *Adv. Funct. Mater.* **2013**, *23*, 3584–3594.

34. Proctor, C. M.; Albrecht, S.; Kuik, M.; Neher, D.; Nguyen, T.-Q. *Adv. Energy Mater.* **2014**, *4*, 00230.

35. Nakanishi, R.; Nogimura, A.; Eguchi, R.; Kanai, K. *Organic Electronics* **2014**, *15*, 2912–2921.

36. Yan, H.; Chen, Z.; Zheng, Y.; Newman, C.; Quinn, J. R.; Dötz, F.; Kastler, M.; Facchetti, A. *Nature* **2009**, *457*, 679–686.

37. van der Poll, T. S.; Love, J. A.; Nguyen, T.-Q.; Bazan, G. C. *Advanced Materials* **2012**, *24*, 3646–3649.

38. Ottinger, O. M.; Melzer, C.; von Seggern, H. *Journal of Applied Physics* **2009**, *106*, 023704–023704–5.

39. Love, J. A.; Proctor, C. M.; Liu, J.; Takacs, C. J.; Sharenko, A.; van der Poll, T. S.; Heeger, A. J.; Bazan, G. C.; Nguyen, T.-Q. *Adv. Funct. Mater.* **2013**, *23*, 5019–5026.

40. Mukherjee, S.; Proctor, C. M.; Tumbleston, J. R.; Bazan, G. C.; Nguyen, T.-Q.; Ade, H. *Adv. Mater.* **2015**, *27*, 1105–1111.

41. Love, J. A.; Nagao, I.; Huang, Y.; Kuik, M.; Gupta, V.; Takacs, C. J.; Coughlin, J. E.; Qi, L.; van der Poll, T. S.; Kramer, E. J.; Heeger, A. J.; Nguyen, T.-Q.; Bazan, G. C. *J. Am. Chem. Soc.* **2014**, *136*, 3597–3606.

42. Gélinas, S.; Rao, A.; Kumar, A.; Smith, S. L.; Chin, A. W.; Clark, J.; van der Poll, T. S.; Bazan, G. C.; Friend, R. H. *Science* **2014**, *343*, 512–516.

43. Burke, T. M.; McGehee, M. D. *Adv. Mater.* **2014**, *26*, 1923–1928.

44. Groves, C. *Energy Environ. Sci.* **2013**, *6*, 1546–1551.

45. van Eersel, H.; Janssen, R. A. J.; Kemerink, M. *Advanced Functional Materials* **2012**, *22*, 2700–2708.

46. Bartelt, J. A.; Beiley, Z. M.; Hoke, E. T.; Mateker, W. R.; Douglas, J. D.; Collins, B. A.; Tumbleston, J. R.; Graham, K. R.; Amassian, A.; Ade, H.; Fréchet, J. M. J.; Toney, M. F.; McGehee, M. D. *Adv. Energy Mater.* **2013**, *3*, 364–374.

47. Kaake, L. G.; Jasieniak, J. J.; Bakus, R. C.; Welch, G. C.; Moses, D.; Bazan, G. C.; Heeger, A. J. *J. Am. Chem. Soc.* **2012**, *134*, 19828–19838.

48. Credgington, D.; Jamieson, F. C.; Walker, B.; Nguyen, T.-Q.; Durrant, J. R. *Adv. Mater.* **2012**, *24*, 2135–2141.

49. Zalar, P.; Kuik, M.; Ran, N. A.; Love, J. A.; Nguyen, T.-Q. *Adv. Energy Mater.* **2014**, *4*, 00438.

50. Bartesaghi, D.; Pérez, I. d. C.; Kniepert, J.; Roland, S.; Turbiez, M.; Neher, D.; Koster, L. J. A. *Nat Commun* **2015**, *6*, DOI: 10.1038/ncomms8083.

51. Koster, L. J. A.; Shaheen, S. E.; Hummelen, J. C. *Adv. Energy Mater.* **2012**, *2*, 1246–1253.

52. Cho, N.; Schlenker, C. W.; Knesting, K. M.; Koelsch, P.; Yip, H.-L.; Ginger, D. S.; Jen, A. K.-Y. *Adv. Energy Mater.* **2014**, *4*, 01857.

53. Tamayo, A. B.; Dang, X.-D.; Walker, B.; Seo, J.; Kent, T.; Nguyen, T.-Q. *Applied Physics Letters* **2009**, *94*, 103301.

54. Kim, C.; Liu, J.; Lin, J.; Tamayo, A. B.; Walker, B.; Wu, G.; Nguyen, T.-Q. *Chem. Mater.* **2012**, *24*, 1699–1709.

55. Proctor, C. M.; Nguyen, T.-Q. *Applied Physics Letters* **2015**, *106*, 083301.

56. Beerbom, M. M.; Lägel, B.; Cascio, A. J.; Doran, B. V.; Schlaf, R. *Journal of Electron Spectroscopy and Related Phenomena* **2006**, *152*, 12–17.

Chapter 4

Mapping Orientational Order in a Bulk Heterojunction Solar Cell using Polarization-Dependent Photoconductive Atomic Force Microscopy

Both research and commercial interest in organic photovoltaics (OPVs) continue to increase as power conversion efficiencies (PCEs) exceed 10%.[1] The best of these devices are based on the bulk heterojunction (BHJ) concept where electron donor and acceptor self-assemble in three-dimensions. Ideally, photo-excitations are within about 20 nm of a donor/acceptor heterojunction and undergo charge-separation. Once separated, a built-in field drives the electron (hole) through continuous pathways of acceptor (donor) molecules over a distance of order 100 nm to be collected at the cathode (anode). The self-organization of the solid thin-film plays a critical role in the opto-

electronic function of these devices. Consequently, great effort has been made to optimize morphology through improved purity, changes in molecular structure, and processing of the blend films.[2] Recently, solution-processable, small molecule donor materials like 7,7′-(4,4-bis(2-ethylhexyl)-4H-silolo[3,2-b:4,5-b′]dithiophene-2,6-diyl)bis(6-fluoro-4-(5′-hexyl-[2,2′-bithiophen]-5-yl)benzo[c][1,2,5]thiadiazole), p-DTS(FBTTh$_2$)$_2$ (shown in **Figure 4.1**), have become an attractive alternative to polymer donor materials due to their facile synthesis, high purity, and competitive PCE.[3–13] Using the electron acceptor [6,6]-phenyl-C$_{70}$-butyric acid methyl ester (PC$_{71}$BM) and appropriate processing conditions, the PCE can exceed 7%. Previous studies have shown that processing can strongly alter donor crystallinity and crystallite size, influencing the opto-electronic performance, but much still remains to understand about these well-performing systems. Interestingly, in addition to the small donor crystallites, structural studies demonstrate the existence of in-plane ordering on a second length-scale in p-DTS(FBTTh$_2$)$_2$ (*vide infra*) and similar, isomorphic derivatives—a micron-scale orientational order of donor material.[13] This orientational order exists not only in the pure donor films, but also in BHJ blends as part of the nano-structured donor/acceptor network. The connection of this micron-scale order to the opto-electronic function has yet to be explored and represents an intriguing aspect of these well-performing materials.[13,14]

Here we investigate the connection of long-range order and the opto-electronic properties using a new technique: polarization-dependent, photoconductive atomic force microscopy (pd-pcAFM). The pd-pcAFM method combines the well-established pcAFM technique,[15–19] a probe of nano-scale photocurrent and electronic transport, with the polarization-dependent optical absorption of most organic molecules to investigate local orientational order. In traditional pcAFM, a small bias is applied between a conductive AFM probe and a planar bottom electrode while illuminating the sample via an inverted optical microscope, as illustrated in **Figure 4.2**. Photons absorbed throughout the active

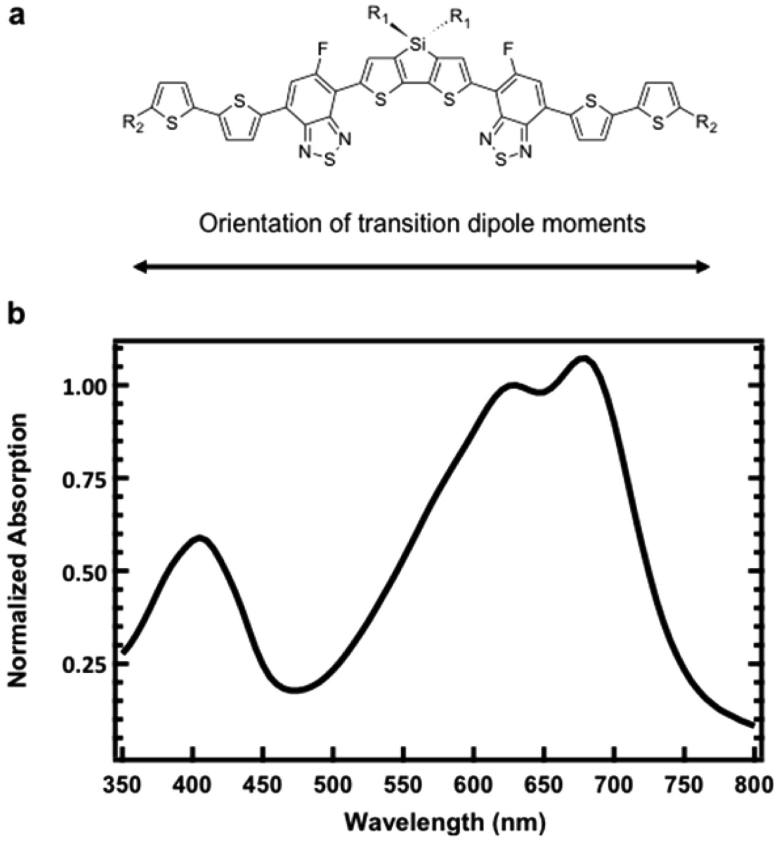

Figure 4.1: a) Molecular structure of p-DTS(FBTTh$_2$)$_2$. R$_1$ = 2-ethylhexyl, R$_2$ = n-hexyl. b) Thin-film absorption spectrum of a p-DTS(FBTTh$_2$)$_2$. Gas-phase, single molecule density functional theory calculations (Appendix B.1) show the transition dipole moments are parallel to the molecular long-axis for the conformation in part (a). It is noted that μL remains along the molecular long-axis for other low-lying molecular conformations likely present in the thin-film; however, the direction of the higher-energy transitions may be more complicated.

layer can lead to photogenerated free-carriers, which are transported through the three-dimensional morphology and collected by the tip. The bias is chosen to selectively collect photogenerated electrons or holes and it is small to ensure minimal injection of carriers into the active layer.[16] Photocurrent is then mapped out over the active layer surface at high spatial resolution ($\sim$20 nm), enabling detailed study of nano-scale opto-electronic properties under a variety of operating conditions and elucidating the link between nano-scale electronic properties and macroscopic device performance. The pd-pcAFM method

adds a new dimension to pcAFM data acquisition and interpretation. Monochromatic, polarized light with a controllable in-plane polarization direction is used to illuminate the sample at normal incidence. The light polarization introduces molecular orientation dependence into the photon absorption and charge-generation rate; multiple photocurrent maps of the same sample area are then acquired for different polarization directions. The polarization-dependence of the local photocurrent reflects the degree of nano-scale orientational order and provides a link between morphology and opto-electronic properties at a spatial resolution beyond the diffraction limit of an optical microscope. Polarized pho-

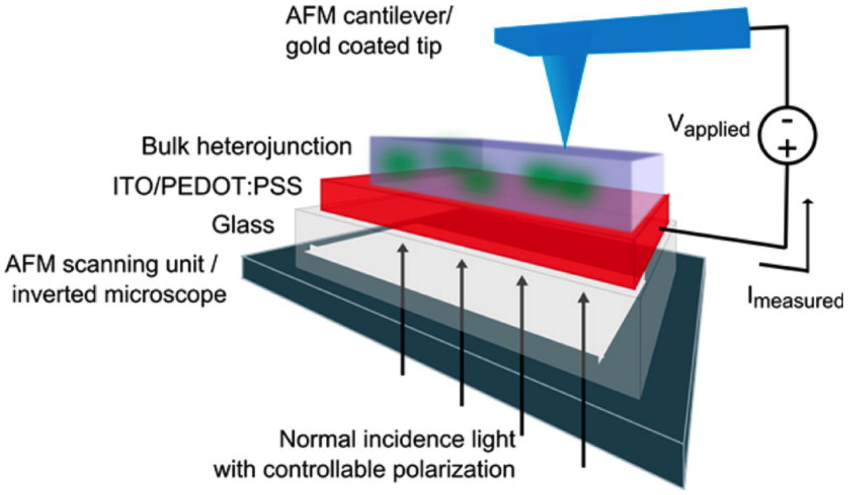

Figure 4.2: A schematic of polarization-dependent photoconductive AFM. The p-DTS$(FBTTh_2)_2$:$PC_{71}BM$ BHJ sample is mounted atop an inverted microscope with the illumination through the glass/ITO/PEDOT:PSS layers. The gold-coated AFM tip is brought into contact with the BHJ layer to act as the back electrode. A small bias is applied between the tip and ITO electrode and the photocurrent is measured while scanning the tip across the sample. The wavelength and incident polarization vector, which lies in the sample plane, are computer controlled.

tocurrent images were collected from p-DTS$(FBTTh_2)_2$ BHJ films as well as from pure donor film. We show that polarization-dependent, micron-scale charge-generation exists in all samples as a consequence of the local alignment of the transition dipoles. Maps of the orientational order are in qualitative agreement with complementary dark-field transmission electron microscopy (TEM) experiments and suggest a liquid crystalline order of

the donor material exists within all thin-films. From analysis of pd-pcAFM data, a lower bound on the average nano-scale order parameter is estimated to be 0.3, suggesting a large degree of local alignment. These results demonstrate the utility of pd-pcAFM in probing anisotropy in the opto-electronic properties and morphology.

4.1 Optical absorption of pure donor and BHJ blend films

The thin-film absorption spectrum of pristine p-DTS($FBTTh_2$)$_2$ shows two major absorption bands around 410 and 670 nm characteristic of the intra-molecular donor-acceptor interactions as well as a vibronic replica ($\sim$620 nm), consistent with aggregation in the solid-state (Figure 4.1b). Following the time-dependent density functional theory calculations of Zhugayevych, *et al.*,[20] the orientation and amplitude of the transition dipole moments of a single molecule were calculated at a CAM-B3LYP/6-31G* level of theory in the conformation previously observed in the single-crystal structure (Figure 4.1a). The calculated transition dipole moments within the low- and high-energy bands lie along the molecular long-axis. Detailed spectroscopic analysis of similar materials found the inter-molecular interactions are relatively weak;[21] thus, approximating the transition dipole moment of the crystal along the molecular long axes is expected to be sufficient for the purposes of this study. Light absorption is expected to follow the usual $cos^2(\theta)$ dependence for θ, the angle between the incident polarization vector and the transition dipole. Since the purpose of the study reported herein is to elucidate the connection between the nano-scale opto-electronic properties and morphology in BHJ films, [6,6]-phenyl-C_{61}-butyric acid methyl ester ($PC_{61}BM$) was substituted for $PC_{71}BM$ to suppress absorption from the fullerene, but with no loss in generality (Table 4.1).

Table 4.1: Solar cell device parameters as a function of solvent additive concentration and fullerene derivative. [Z]Device parameters reproduced from Reference [4].

v/v % DIO	Acceptor	J_{SC} (mA cm^{-2})	Fill-factor (%)	V_{OC} (mV)	PCE %
0.4%[Z]	$PC_{71}BM$	12.8	68	809	7.0
0%[Z]	$PC_{71}BM$	6.6	36	780	1.8
0.4%	$PC_{61}BM$	10.46	67	803	5.7

4.2 Thin-film morphology

To put the development of the pd-pcAFM technique in the proper context and preface the peculiar opto-electronic properties, transmission electron microscopy (TEM) is used to establish the co-existence of a complex nano-structure and long-range orientational order within the optimized blend film. **Figure 4.3a** shows a typical high-resolution TEM (HRTEM) image of a p-DTS($FBTTh_2$)$_2$:$PC_{61}BM$ blend film with 0.4% v/v 1,8-diiodooctane (DIO) as a co-solvent. These processing conditions have been found empirically to yield the best PCE (Table 4.1).[4] TEM gives a projection of the structure through the full thickness of the film (∼80 nm) and has been used to great effect to understand the ordering in organic systems.[22–26] The lattice planes of the donor crystallites, corresponding to alkyl-stacking, with a d-spacing of 2.2 nm, are the most obvious feature under these imaging conditions, although it should also be understood that only fibers satisfying the Bragg condition are visible. Previous studies show that these fibers extend throughout the thickness of the film, bending and twisting in three dimensions.[27] While the relative orientations of nearby fibers are likely partially correlated, many directions are still observed locally. The nominal width of the fibers in this 'rice-grain' structure is 10-20 nm,[27] length-scales commonly believed to best balance charge-generation and charge-transport in small-molecule and polymer active layers.[2,3,28]

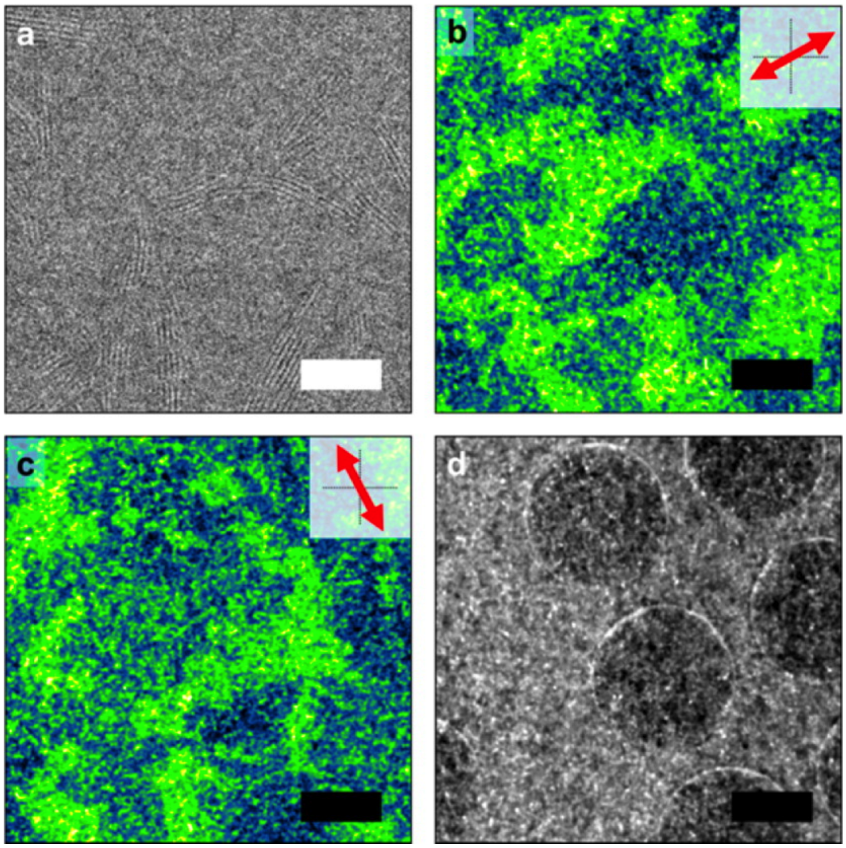

Figure 4.3: a) HRTEM image showing lattice planes, d-spacing of 2.2 nm, of fiber-like structures in a p-DTS(FBTTh$_2$)$_2$:PC$_{61}$BM film processed with 0.4% v/v DIO. b-c), Dark-field images of orthogonal crystallite directions at a fixed location. The image intensity, in order of increased scattering, goes black, blue, green, yellow, white. Micron-scale order is visible along with smaller, randomly oriented crystallites. d) Sum of the twelve dark-field images covering all in-plane directions at the same location. Only the 2 μm holes of the TEM grid are visible, suggesting the micron-scale order covers the film. The white (black) scale bar is 30 nm (1.2 μm).

The situation is quite different for crystallites of the donor molecule that $\pi - \pi$ stack in-plane (d-spacing of $\sim$3.6 Å); dark-field TEM can be used to image the micron-scale orientational order of this crystal population.[13,26] In a single dark-field TEM image, bright regions denote crystalline regions with an in-plane orientation. This orientation is determined by the position of a small aperture in the back focal plane of the objective lens and can be easily controlled as to probe any in-plane orientation. Twelve total dark-field images at a fixed location were taken to cover all in-plane crystallite orientations. Two images with orthogonal crystallite directions are shown in Figure 4.3b and Figure 4.3c, respectively. Both show micron-scale structures consistent with agglomerates of smaller crystallites in similar orientations, along with speckles resulting from quasi-randomly oriented crystallites. The two images are nearly complementary, that is bright regions in Figure 4.3b, denoting crystallites oriented in a particular direction, correlate well with dark regions in the Figure 4.3c, signifying an absence of crystallites oriented in a perpendicular direction. In total, the micron-scale locally oriented features cover the blend film as evidenced by the uniformity of the summed images (Figure 4.3d) and an animation of the azimuthal dark-field image series showing the smooth deformations in the local crystal orientation.[29] Thus, the donor self-organizes on both nanometer and micron length-scales in a well-performing device. For reference, the BHJ processed without the solvent additive shows no fiber-like texture in the HRTEM images and no indication of significant phase separation is observed—consistent with the lower device performance (Table 4.1).[27] Interestingly, this film also shows long-range order of the in-plane $\pi - \pi$ stacking population as well and is of similar length-scale to the optimized BHJ (Figure B.6). The diffraction and order of the pristine donor film is exceptional compared to either of the BHJ blends and the length-scale of the long-range order is increased. Dark-field images of orthogonal crystallite orientations with complementary coverage are presented in **Figure 4.4**. These images suggest orientational order over several microns

and the sum of the azimuthal dark-field image series (Figure 4.4c) is uniform except for a few dark regions. These dark regions are likely also crystalline, but may be either slightly misoriented such that the Bragg condition is no longer satisfied or in a different orientation. HRTEM images show large-crystals with a d-spacing of 2.2 nm, although they are relatively rare and cover a small fraction of the film. An example of such a crystal is shown in Figure 4.4d. The results indicate that while the fullerene and solvent additives strongly modify the self-assembly process within these blends, long-range order is intrinsic to the donor material.

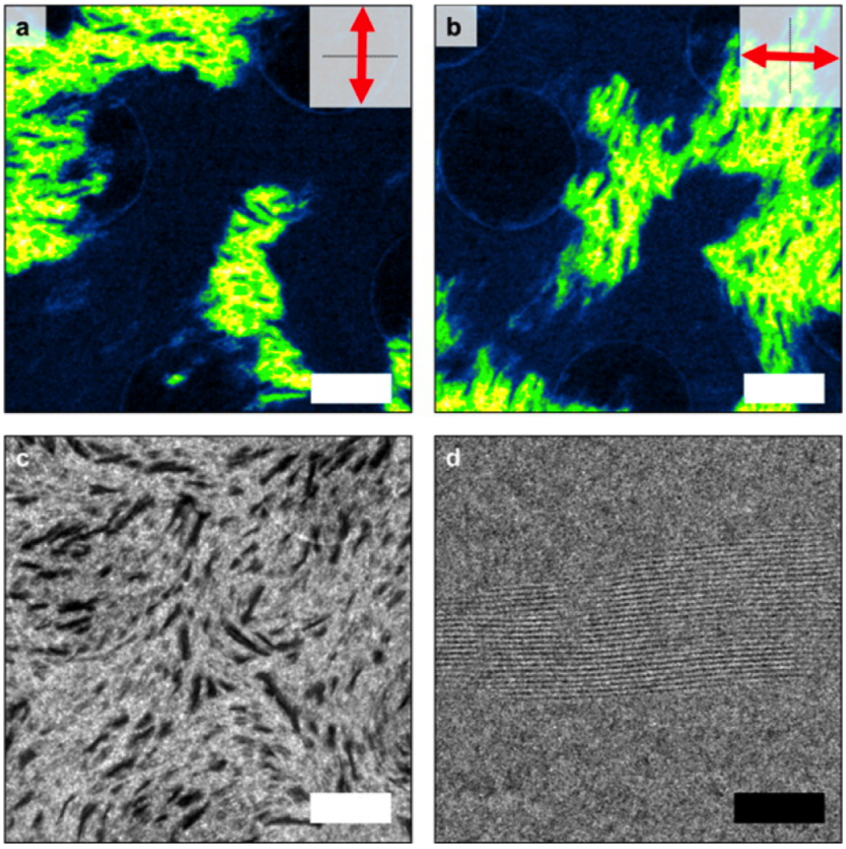

Figure 4.4: a-b) Dark-field images of pure p-DTS(FBTTh$_2$)$_2$ films with orthogonal orientations. Red arrows show the approximate in-plane crystallite orientation. c) Sum of the twelve dark-field images which cover all possible in-plane crystallite orientations. d) HRTEM image showing a portion of a large crystallite with a d-spacing of 2.2 nm. Such crystals are relatively rare. The white (black) scale bar is 1.2 μm (35 nm).

4.3 Polarization-dependent photoconductive AFM

The common local orientation of the donor molecules implies alignment of their transition dipoles and locally anisotropic optical properties. It follows that the local optical absorption and charge-generation depends on the incident light polarization in a manner reflective of the underlying molecular orientation and local morphology. To simultaneously measure the polarization-dependence of the nano-scale photocurrent and minimize drift during pd-pcAFM acquisition, scanning is interleaved in the +y direction with a combination of four in-plane polarization directions and/or wavelengths. After deinterleaving, the pixel resolution of each photocurrent map is 512 px×128 px with a physical aspect ratio of 1:1. A positive bias ranging between 0.5 and 1.5 V was applied to the substrate such that the gold-coated tip selectively probes the local photogenerated hole current, making it most sensitive to the donor material. The contribution of charge injection (*i.e.*, the dark current) is small compared to the photocurrent contrast. In effect, the nano-scale device is analogous to a photodetector and the response depends on local charge-generation and charge-collection. Fortunately, the charge-generation rate is expected to be proportional to the optical absorption and the charge-collection is approximately independent of the illumination conditions; thus, relative changes in the polarization-dependent photocurrent reflect the local molecular orientation at each point on the sample. The p-DTS(FBTTh$_2$)$_2$:PC$_{61}$BM BHJ films processed with and without the solvent additive show micron-scale photocurrent anisotropy for both polarized 650 nm and 405 nm wavelengths (**Figure 4.5** and **Figure 4.6**). Along a fixed polarization direction, both wavelengths give rise to near identical micron-scale structure consistent with the transition dipoles being co-linear with the molecular long-axis and oriented in-plane. Significant changes in the photocurrent are also observed after rotating the in-plane polarization by 90°. This strongly indicates that the large-scale changes in the

photocurrent are not the result of dead regions within the device. If the local polarization-dependent optical absorption of the thin-film is proportional to $cos^2(\theta)$, an approximation that neglects self-absorption through the film thickness, optical interference effects, and any non-idealities in the photocurrent collection process, the sum of any orthogonal pair of photocurrent maps is complementary and the result is similar to the 'polarization-averaged' or unpolarized photocurrent response, *i.e.*, $cos^2(\theta) + cos^2(\theta + 90°) = 1$. For the BHJ film processed without the additive, the sums of the 650 nm and 405 nm orthogonal photocurrent maps are shown in Figure 4.5e and Figure 4.5f, respectively. Both summed images are nearly uniform on the micron scale, implying the polarization-averaged photo response is remarkably homogenous despite the large-scale structural heterogeneity. For the optimized BHJ, micron-scale structure is also visible in the polarized photocurrent maps in addition to nano-scale features that are presumably fluctuations in the local hole mobility related to donor-acceptor phase separation and the well-developed fiber morphology observed with TEM. Much of the large-scale structure is complementary. The sum of the orthogonal maps (Figure 4.6e) is more uniform than either individual photocurrent map, but the sum shows some residual large-scale inhomogeneity (Figure 4.6e) not present in photocurrent maps taken with unpolarized, highly-focused white-light illumination (Figure 4.6f). This residual inhomogeneity is believed to be linked to the exponential absorption through the film thickness, which leads to small distortions from the expected $cos^2(\theta)$ profile (Appendix B.5). Remarkably, the length-scales observed in the raw pd-pcAFM and dark-field TEM data qualitatively agree, but additional analysis will be required to directly compare the two techniques.

By assuming a simple model of the polarization-dependent photocurrent, the information from multiple photocurrent maps can be combined to estimate molecular orientation and the degree of orientational order at each point on the sample. Four photocurrent maps with in-plane polarization vectors of 0°, 45°, 90°, and 135° are fit to an isotropic

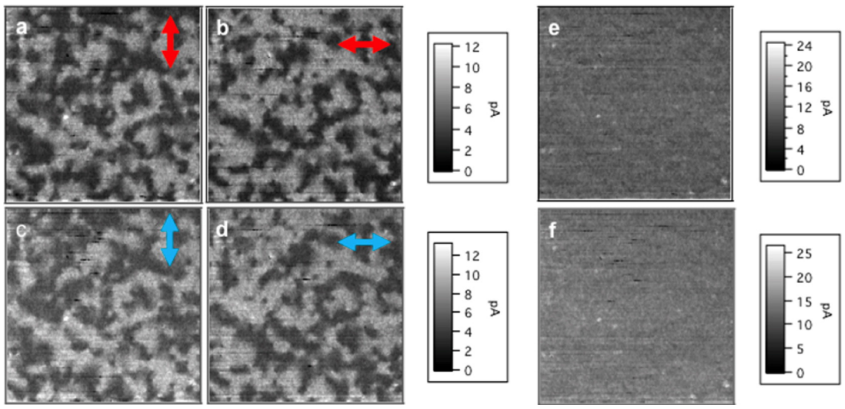

Figure 4.5: Two pairs of orthogonal, polarized photocurrent maps for incident 650 nm, parts a) and b), and 405 nm, parts c) and d), light all taken from the same location of a p-DTS(FBTTh$_2$)$_2$:PC$_{61}$BM BHJ film processed without the solvent additive. Both wavelengths show nearly identical, micron-scale anisotropy and complementary structure for the orthogonal polarization. The incident polarization direction and wavelength are indicated in the upper right of each image. The sum of the two orthogonal photocurrent maps at 650 nm, part e), and 405 nm, part f), are almost completely uniform. All images are 10 μm×10 μm in size.

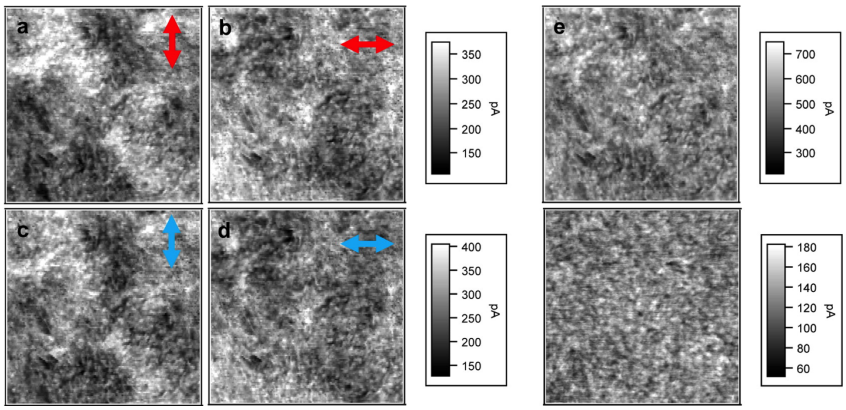

Figure 4.6: Two pairs of orthogonal, polarized photocurrent maps for incident a,b) 650 nm and c,d) 405 nm light, all taken from the same location of an p-DTS(FBTTh$_2$)$_2$:PC$_{61}$BM BHJ film with 0.4% v/v DIO. Both wavelengths show nearly identical, micron-scale anisotropy and complementary structure for the orthogonal polarization. The incident polarization direction and wavelength are indicated in the upper right of each image. The sum of the two orthogonal photocurrent maps at 650 nm, part e), is more uniform, similar to focused white light, part f), taken at another location on the sample. All images are 5 μm×5 μm in size.

background with a single dipole-like dependence as in Equation (1):

$$I(x, y; \beta) = A(x, y) + 2B(x, y) \cos^2(\beta - \phi(x, y)) \quad (1)$$

where the in-plane polarization direction is β, $I(x, y; \beta)$ is the local photocurrent, $A(x, y)$ is the polarization-independent current, and $2B(x, y)cos^2(\beta - \phi(x, y))$ is the polarization-dependent current contribution of molecules oriented at an angle $\phi(x, y)$. It is useful to equate $\phi(x, y)$ with the molecular director, which represents the average local orientation of the molecules at any point on the film. By assuming the photocurrent is proportional to the local absorbance, the local anisotropy can be used to define a lower bound on a two-dimensional orientational order parameter. The pointwise dichroic ratio, the ratio of the local absorbance parallel and perpendicular to the direction of molecular alignment, can be written as $R(x, y) = (A(x, y)+2B(x, y))/A(x, y)$, the ratio between the nano-scale photocurrents parallel and perpendicular to the local molecular director. The orientational order parameter can then be defined as $S =< (R(x, y) - 1)/(R(x, y) + 1) > (x, y)$ where a lower (upper) bound of S = 0 (S = 1) indicates a completely isotropic (oriented) structure at each point on the film.[28] This order parameter represents the average nano-scale alignment expected at any point on the sample and is applicable for films which are isotropic on macroscopic length-scales. By estimating the molecular director, the pd-pcAFM and dark-field TEM data can be compared side-by-side for the p-DTS($FBTTh_2$)$_2$:$PC_{71}BM$ BHJ processed with 0.4% v/v DIO. The local molecular orientation determined by pd-pcAFM is shown in **Figure 4.7a** using a 630 nm excitation wavelength. The map is a visualization of $\phi(x, y)$ in the form of a director field, a grid of short lines drawn parallel to the proposed molecular long-axis, and the micron-scale orientational order is clearly visible. It is worth noting that the film topography, which is acquired simultaneously with the pd-pcAFM data (Figure B.2b), is relatively smooth and

unremarkable in these BHJ samples with no clear indication of micron-scale orientational order. An equivalent analysis is performed for the dark-field image series (Appendix B.2) and the result is shown in **Figure 4.7b**. The length-scale and spatial structure from pd-pcAFM and dark-field TEM are qualitatively indistinguishable. This suggests the two radically different techniques likely probe a similar aspect of the internal order.

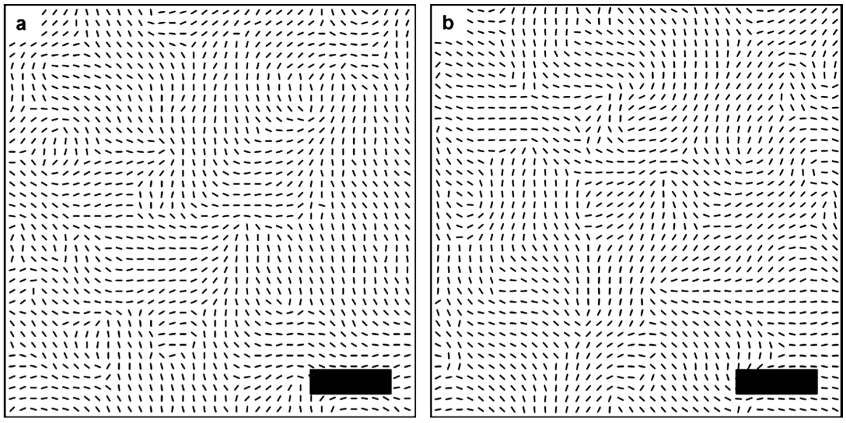

Figure 4.7: Director field constructed from (a) pd-pcAFM and (b) dark-field TEM images of a p-DTS(FBTTh$_2$)$_2$:PC$_{71}$BM BHJ film with 0.4% v/v DIO. The data are taken from separate but identically prepared samples. Both methods give comparable, micron-scale structure suggesting they probe the same internal order of the BHJ film. The scale bar is 1 μm.

In all films investigated the director fields are reminiscent of a liquid crystalline state. Detailed examination of the director fields at higher resolution shows what appear to be $\pm 1/2$ disclinations in all samples. A comparison between the p-DTS(FBTTh$_2$)$_2$:PC$_{71}$BM BHJ film with 0.4% v/v DIO and p-DTS(FBTTh$_2$)$_2$:PC$_{61}$BM BHJ film without solvent additive is shown in **Figure 4.8**. The disclinations occur frequently, often observed in conjugate pairs, with the distance between disclination cores sometimes less than 500 nm. Despite the differences in crystallinity, phase separation and device parameters, it seems the liquid crystalline nature associated with the $\pi-\pi$ stacking of p-DTS(FBTTh$_2$)$_2$ within the blends is independent of additive. For the pure film, along with the liquid crystalline structure, pinholes/defects in the film topography are observed in the cen-

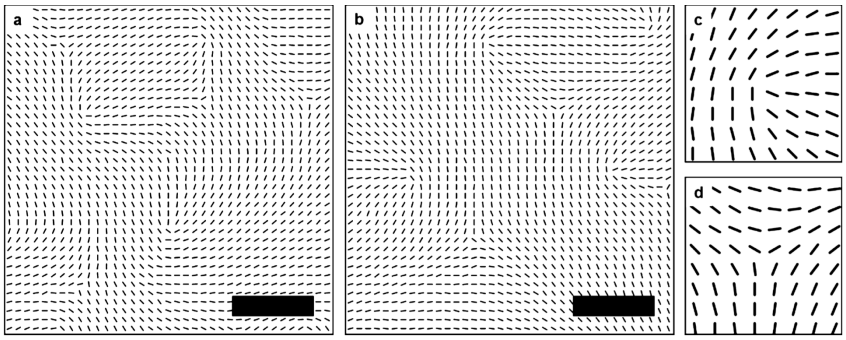

Figure 4.8: Reconstructed director field from high-resolution pd-pcAFM scans of a) p-DTS($FBTTh_2$)$_2$:$PC_{71}BM$ BHJ with 0.4% v/v DIO and b) p-DTS($FBTTh_2$)$_2$:$PC_{61}BM$ BHJ. Examples of $+1/2$ and $-1/2$ disclinations extracted from the p-DTS($FBTTh_2$)$_2$:$PC_{61}BM$ blend film are shown in c) and d), respectively. The scale bars are 500 nm.

ter of each imaged disclination. To demonstrate this correlation, the film topography is overlaid by the estimated molecular director ϕ(x,y) as shown in **Figure 4.9**. The molecular orientation is represented by both the short lines of the director field and a color-coded overlay of ϕ(x,y) to improve the effective resolution. As the topography is included primarily to show the pinholes/defects, the height is scaled from white (+5 nm) to black (-20 nm) with regions >20 nm below the film surface shown as solid blue. Some fine-grain structure is apparent in the topography but the film is smooth compared to other studies of p-DTS($FBTTh_2$)$_2$ where long-range order is directly apparent. During imaging, the pinholes/defects do change the contact with the AFM tip, which changes the photocurrent to some extent, but the polarization-dependence of the photocurrent is still readily apparent (Appendix B.4). From the pd-pcAFM data, the disclinations are clearly visible across the film. Remarkably, a pinhole/defect is observed at the center of each disclination, *i.e.*, a disclination core, and the depth tends to be >20 nm; however, not all surface defects/pinholes correspond to imaged disclinations. The formation of both the pinhole, a distortion of the film surface, and the disclination core, a line defect normal to film plane, are expected to cost energy. This observation of a pinhole/defect at the disclination core suggests that minimizing the length of the line defect by distort-

ing the surface lowers the overall cost of the disclination. The estimated lower bound

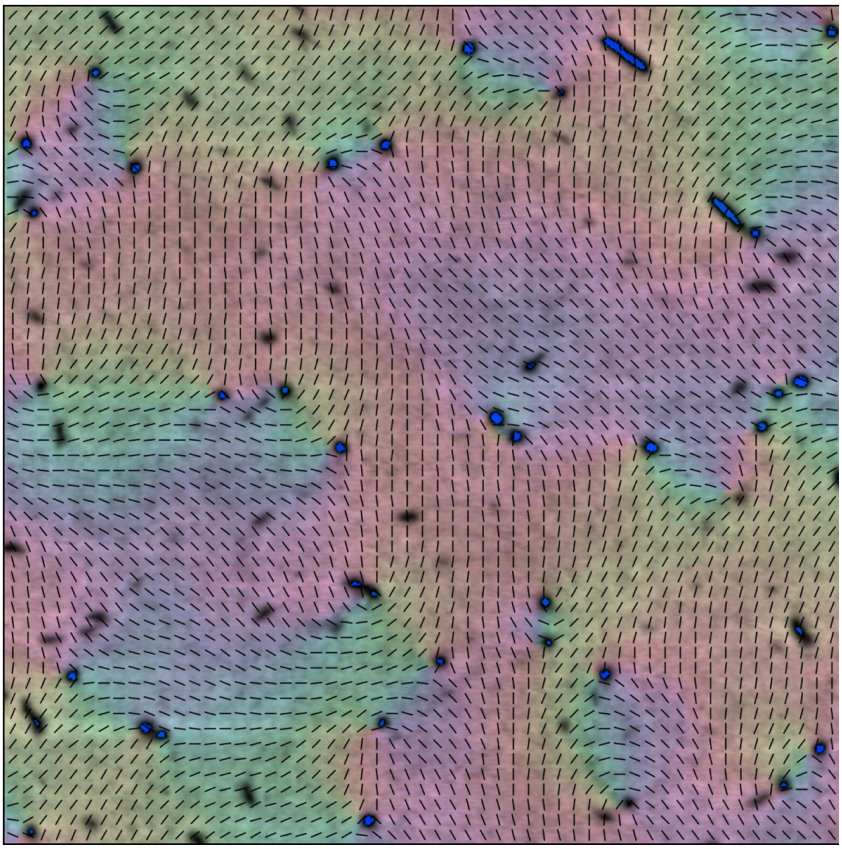

Figure 4.9: AFM topography of the pure p-DTS($FBTTh_2$)$_2$ film overlaid by the director field. As the resolution of the director field is limited to the size of the lines, ϕ(x,y) is included as a color overlay to improve the resolution. The topography appears in grey scale from +5 nm to -20 nm with anything less than -20 nm displayed as solid blue. The image is 10 μm×10 μm in size.

for the orientational order parameter is approximately 0.3 in all films, which suggests a significant fraction of local alignment and a remarkable level of structural organization over length-scales not typically considered in BHJ materials. The order parameter (photocurrent) exceeds 0.29 in the p-DTS($FBTTh_2$)$_2$:$PC_{71}BM$ BHJ device processed with 0.4% v/v DIO (∼170 pA at 2 V bias), 0.31 for the p-DTS($FBTTh_2$)$_2$:$PC_{61}BM$ BHJ device processed without DIO (∼10 pA at 1 to 1.5 V bias), and 0.31 for the pure p-DTS($FBTTh_2$)$_2$ film (about 5 pA at 1.5 V bias). For all films, it is important to note

that $R(x, y)$ shows some spatial dependence that appears correlated to surrounding features in the director field (Figure B.11). $R(x, y)$ is highest in the well-aligned regions with lower values in regions of higher bend/splay, which is consistent with a broader range of molecular orientations being present locally. In the BHJ films, it is interesting that the DIO, which is known to markedly change the timescale of the film formation process,[30] does not appear to significantly lower or raise the order parameter despite a nearly ten-fold increase in the photocurrent. We postulate that the liquid crystalline structure is a marker of an earlier lyotropic phase and its formation is independent of the additive. A better understanding as to the role of long-range order in OPVs may lead to improved material design and device processing. Polarization-dependent photocurrents are likely observable in a variety of materials with both linear[26,31–33] and circularly polarized light.[34] Although most commonly discussed in the context of organic field effect transistors,[33,35–40] orientational order may be beneficial for OPV devices—particularly for molecular semiconductors, which lack the intrinsic built-in connectivity of polymers. The local alignment may connect donor crystallites laterally through low-angle grain boundaries that provide alternative pathways to the anode.[13] Such effects could be important due to the highly anisotropic electronic properties of most organic crystals and the considerable effect grain boundaries are expected to have on charge-carrier transport. Alternatively, local orientational order can substantially reduce the absorption of unpolarized light (*e.g.*, sunlight) and lower the external quantum efficiency of optically thin or locally well-aligned devices, a concern particularly for directed morphologies, *e.g.*, lamellar block-copolymers[41–44] and liquid crystalline materials.[39,45] In a single-layer OPV device that is isotropic over macroscopic dimensions, the difference between polarized and unpolarized illumination is likely difficult to detect electronically; however, a subtle difference may be detectable in tandem devices, leading to an interesting class of polarization sensitive photodetectors. Such photodetectors would rely on the fact that in a

tandem device, one layer can polarize the light for the next, which creates spatial fluctuations in charge-generation rates between layers that increase if the light is polarized (the lateral conductivity in such systems must be sufficiently low so that the local imbalances appreciably lower the overall PCE). The pd-pcAFM results also suggest that exploiting polarization-dependent sample interactions may be useful in other scanning probe techniques such as photopotential fluctuation spectroscopy,[46] electric force microscopy,[47,48] and scanning kelvin probe microscopy to further probe the role of orientational order in organic semiconductors.[49] As a technique, pd-pcAFM is complementary to other high-resolution probes of molecular organization like TEM and soft x-ray scattering. With TEM, the existence of long-range order was inferred by local anisotropy in the $\pi-\pi$ scattering over microns, but the amplitude of the diffracted signal is not a reliable measure of local alignment. For example, the diffracted intensity visible in the dark-field image of the pure donor (Figure 4.4a-b) accounts for less than 3% of the incident beam and $\sim$0.3% in the BHJ films, making it challenging to balance electron beam damage and resolution.[24] In pd-pcAFM, the polarization-dependence is easily related to the degree of local alignment and the technique is not intrinsically destructive, leaving significant opportunities for further technique development with important insights likely to follow. Soft x-ray characterization[31,32] also relies on the polarization-dependent absorption of high-energy transitions, corresponding to ionization of core-electrons to unoccupied molecular orbitals ($\sim$290 eV), from monochromatic synchrotron sources. These high-energy dipole transitions are normal to the plane of conjugation[32] (*i.e.*, in the direction of $\pi-\pi$ stacking) and orthogonal to the visible-light transition moments for most conjugated molecules and polymers. This means pd-pcAFM probes orientational order in an orthogonal direction to scanning transmission X-ray microscopy, allowing access to new aspects of the molecular organization.

4.4 Conclusions

The pd-pcAFM technique was developed as a general method combining polarization-dependent light-matter interactions with nano-scale charge generation and transport. Application to a high-performance BHJ device (7.0% PCE) revealed micron-scale, liquid crystalline order is integrated within the complex donor/acceptor BHJ structure in addition to a lower PCE device and the pristine donor material. It was demonstrated that the polarization-dependence of the nano-scale photoconductivity can be used to reconstruct the local molecular orientation and estimate the orientational order parameter at high-spatial resolution. By connecting the polarization-dependent opto-electronic properties with complementary TEM results, we demonstrated that the BHJ is not a random formation of 'crystalline' and 'amorphous' structures but an elegant and multifaceted manifestation of self-assembly over a broad range of length-scales much larger than typically considered.

4.5 Experimental Section

Sample Fabrication: All active layers were spin cast at 1750 rpm from 35mg mL^{-1} of p-DTS($FBTTh_2$)$_2$:$PC_{61}BM$ or p-DTS($FBTTh_2$)$_2$:$PC_{71}BM$ (3:2 weight ratio) in chlorobenzene with 0.4% v/v 1,8-diiodoctane. Solutions were heated for several hours at 80 °C and residual solids filtered before casting on PEDOT:PSS coated glass/ITO substrates. After drying for 30 min, films were heated to 70 °C for 10 min under N_2 atmosphere. For solar cell devices, cathodes were deposited by sequential thermal evaporation of calcium (10 nm) and then aluminum (100 nm); the device properties were measured under 100 mW cm^{-2} simulated AM1.5G solar illumination.

TEM: TEM samples were prepared by delamination of the active layer in a DI water

bath and transferred to a C-Flat TEM grid. Low-dose HRTEM images were acquired using SerialEM under approximately parallel illumination: the sample is translated and allowed to stabilized mechanically, the instrumental response is matched to the 2.2 nm d-spacing, the beam is blanked and shifted electronically to an undamaged region, and the image is acquired.[50] The HRTEM total electron dosage is 670 e^- nm^{-2}. Dark-field images were acquired using a 10 μm objective aperture (angular admittance of 55°) also using a low-dose procedure. The twelve dark-field images were acquired in pseudo-random order, covering the half azimuth with an angular resolution of 15° and an accumulated electron dose of 200 e^- nm^{-2}. The very low dose per image is to prevent electron damage from biasing the image series; an additional pair of dark-field images replicating the conditions of the first two is always acquired at the end of the series to check for electron damage effects. All images were taken on an FEI Titan operating at 300kV. The dark-field images were first smoothed by a square window of 200 nm. For each image, the mean value was subtracted to account for small changes in radial distance between the center of the diffraction pattern and the center of the objective aperture. This normalizes out variations in inelastic scattering, which are approximately uniform at all points, admitted by the aperture as the in-plane direction is changed. The dominant scattering direction is extracted point-by-point and used to assign the molecular orientation.

pcAFM: The BHJ sample is deposited atop a glass/ITO/PEDOT:PSS electrode and mounted on an inverted optical microscope/AFM scanning stage. The inverted microscope illuminates the sample through the ITO/glass at normal incidence with a selectable 405, 633, or 650 nm polarized light. A gold-coated AFM probe acts as the back-electrode and a small voltage is applied to collect photogenerated carriers. The photocurrent map is built by scanning the tip back-and-forth in the x direction then incrementing the y direction and repeating until the full image is acquired. All pcAFM images were collected using an Asylum MFP3D (Oxford Instruments) mounted above an Olympus inverted

optical microscope located in an inert glovebox environment. Gold-coated silicon AFM tips with resonant frequency of ∼13kHz and force constant ∼0.2 N m^{-1} (Budget Sensors) were used in all imaging. In unpolarized photoconductive measurements, a Xe lamp light source (Newport Oriel Instruments) was focused through the inverted optical microscope into a light spot approximately 150 μm in diameter. For polarized measurements of $PC_{61}BM$ samples, 650 nm and 405nm laser diodes (Thorlabs CPS184 and CPS405, respectively) with optical shutters were combined using a cube polarizer onto a common optical axis. For polarized measurements of $PC_{71}BM$ samples, a 633 nm HeNe laser was used alone. The polarization was rotated using a liquid crystal variable retarder (Meadowlark) and 1/4 wave plate (Thorlabs FR600QM) giving a polarization purity better than 20:1. The polarization and/or wavelength are changed at the end of each trace in the +x direction, allowing time during the retrace for shutters and LC retarder to stabilize. All pd-pcAFM scans have an original resolution of 512×512 px. After deinterleaving, the resolution of the four individual photocurrent maps is 512×128 px. The estimated incident power density for all illumination sources was ∼5 W cm^{-2}.

References

1. You, J.; Dou, L.; Yoshimura, K.; Kato, T.; Ohya, K.; Moriarty, T.; Emery, K.; Chen, C.-C.; Gao, J.; Li, G.; Yang, Y. *Nature Communications* **2013**, *4*, 1446.

2. Hoppe, H.; Sariciftci, N. S. *J. Mater. Chem.* **2006**, *16*, 45–61.

3. Sun, Y.; Welch, G. C.; Leong, W. L.; Takacs, C. J.; Bazan, G. C.; Heeger, A. J. *Nat Mater* **2012**, *11*, 44–48.

4. van der Poll, T. S.; Love, J. A.; Nguyen, T.-Q.; Bazan, G. C. *Advanced Materials* **2012**, *24*, 3646–3649.

5. Wei, G.; Xiao, X.; Wang, S.; Sun, K.; Bergemann, K. J.; Thompson, M. E.; Forrest, S. R. *ACS Nano* **2012**, *6*, 972–978.

6. Walker, B.; Tamayo, A. B.; Dang, X.-D.; Zalar, P.; Seo, J. H.; Garcia, A.; Tantiwiwat, M.; Nguyen, T.-Q. *Advanced Functional Materials* **2009**, *19*, 3063–3069.

7. Bürckstümmer, H.; Tulyakova, E. V.; Deppisch, M.; Lenze, M. R.; Kronenberg, N. M.; Gsänger, M.; Stolte, M.; Meerholz, K.; Würthner, F. *Angew. Chem.* **2011**, *123*, 11832–11836.

8. Lee, O. P.; Yiu, A. T.; Beaujuge, P. M.; Woo, C. H.; Holcombe, T. W.; Millstone, J. E.; Douglas, J. D.; Chen, M. S.; Fréchet, J. M. J. *Adv. Mater.* **2011**, *23*, 5359–5363.

9. Li, W.; Kelchtermans, M.; Wienk, M. M.; Janssen, R. A. J. *J. Mater. Chem. A* **2013**, *1*, 15150–15157.

10. He, G.; Li, Z.; Wan, X.; Zhou, J.; Long, G.; Zhang, S.; Zhang, M.; Chen, Y. *J. Mater. Chem. A* **2013**, *1*, 1801–1809.

11. Liu, Y.; Chen, C.-C.; Hong, Z.; Gao, J.; Yang (Michael) Yang; Zhou, H.; Dou, L.; Li, G.; Yang, Y. *Scientific Reports* **2013**, *3*, 3356.

12. Lin, Y.; Li, Y.; Zhan, X. *Chem. Soc. Rev.* **2012**, *41*, 4245–4272.

13. Takacs, C. J.; Sun, Y.; Welch, G. C.; Perez, L. A.; Liu, X.; Wen, W.; Bazan, G. C.; Heeger, A. J. *J. Am. Chem. Soc.* **2012**, *134*, 16597–16606.

14. Jasieniak, J. J.; Hsu, B. B.; Takacs, C. J.; Welch, G. C.; Bazan, G. C.; Moses, D.; Heeger, A. J. *ACS Nano* **2012**, *6*, 8735–8745.

15. Coffey, D. C.; Reid, O. G.; Rodovsky, D. B.; Bartholomew, G. P.; Ginger, D. S. *Nano Lett.* **2007**, *7*, 738–744.

16. Dang, X.-D.; Tamayo, A. B.; Seo, J.; Hoven, C. V.; Walker, B.; Nguyen, T.-Q. *Adv. Funct. Mater.* **2010**, *20*, 3314–3321.

17. Groves, C.; Reid, O. G.; Ginger, D. S. *Acc. Chem. Res.* **2010**, *43*, 612–620.

18. Guide, M.; Dang, X.-D.; Nguyen, T.-Q. *Adv. Mater.* **2011**, *23*, 2313–2319.

19. Kamkar, D. A.; Wang, M.; Wudl, F.; Nguyen, T.-Q. *ACS Nano* **2012**, *6*, 1149–1157.

20. Zhugayevych, A.; Postupna, O.; Bakus II, R. C.; Welch, G. C.; Bazan, G. C.; Tretiak, S. *J. Phys. Chem. C* **2013**, *117*, 4920–4930.

21. Eisenmenger, N. D.; Su, G. M.; Welch, G. C.; Takacs, C. J.; Bazan, G. C.; Kramer, E. J.; Chabinyc, M. L. *Chem. Mater.* **2013**, *25*, 1688–1698.

22. Lovinger, A. J.; Katz, H. E.; Dodabalapur, A. *Chem. Mater.* **1998**, *10*, 3275–3277.

23. Voigt-Martin, I. G.; Garbella, R. W.; Schumacher, M. *Macromolecules* **1992**, *25*, 961–971.

24. Martin, D. C.; Chen, J.; Yang, J.; Drummy, L. F.; Kübel, C. *J. Polym. Sci. B Polym. Phys.* **2005**, *43*, 1749–1778.

25. Brinkmann, M.; Rannou, P. *Macromolecules* **2009**, *42*, 1125–1130.

26. Zhang, X.; Hudson, S. D.; DeLongchamp, D. M.; Gundlach, D. J.; Heeney, M.; McCulloch, I. *Adv. Funct. Mater.* **2010**, *20*, 4098–4106.

27. Love, J. A.; Proctor, C. M.; Liu, J.; Takacs, C. J.; Sharenko, A.; van der Poll, T. S.; Heeger, A. J.; Bazan, G. C.; Nguyen, T.-Q. *Adv. Funct. Mater.* **2013**, *23*, 5019–5026.

28. Thompson, B.; Fréchet, J. *Angewandte Chemie International Edition* **2008**, *47*, 58–77.

29. Takacs, C. J.; Collins, S. D.; Love, J. A.; Mikhailovsky, A. A.; Wynands, D.; Bazan, G. C.; Nguyen, T.-Q.; Heeger, A. J. *ACS Nano* **2014**, *8*, 8141–8151.

30. Perez, L. A.; Chou, K. W.; Love, J. A.; van der Poll, T. S.; Smilgies, D.-M.; Nguyen, T.-Q.; Kramer, E. J.; Amassian, A.; Bazan, G. C. *Adv. Mater.* **2013**, *25*, 6380–6384.

31. Collins, B. A.; Cochran, J. E.; Yan, H.; Gann, E.; Hub, C.; Fink, R.; Wang, C.; Schuettfort, T.; McNeill, C. R.; Chabinyc, M. L.; Ade, H. *Nature Materials* **2012**, *11*, 536–543.

32. McNeill, C. R.; Ade, H. *J. Mater. Chem. C* **2012**, *1*, 187–201.

33. Takacs, C. J.; Treat, N. D.; Krämer, S.; Chen, Z.; Facchetti, A.; Chabinyc, M. L.; Heeger, A. J. *Nano Lett.* **2013**, *13*, 2522–2527.

34. Savoini, M.; Biagioni, P.; Meskers, S. C. J.; Duò, L.; Hecht, B.; Finazzi, M. *J. Phys. Chem. Lett.* **2011**, *2*, 1359–1362.

35. Zhang, X.; Bronstein, H.; Kronemeijer, A. J.; Smith, J.; Kim, Y.; Kline, R. J.; Richter, L. J.; Anthopoulos, T. D.; Sirringhaus, H.; Song, K.; Heeney, M.; Zhang, W.; McCulloch, I.; DeLongchamp, D. M. *Nature Communications* **2013**, *4*, 2238.

36. Noriega, R.; Rivnay, J.; Vandewal, K.; Koch, F. P. V.; Stingelin, N.; Smith, P.; Toney, M. F.; Salleo, A. *Nat Mater* **2013**, *12*, 1038–1044.

37. Street, R. A. *Science* **2013**, *341*, 1072–1073.

38. Headrick, R. L.; Wo, S.; Sansoz, F.; Anthony, J. E. *Applied Physics Letters* **2008**, *92*, 063302.

39. Kim, B.-G.; Jeong, E. J.; Chung, J. W.; Seo, S.; Koo, B.; Kim, J. *Nat Mater* **online March 24, 2013**, *advance online publication*, DOI: 10.1038/nmat3595.

40. Diao, Y.; Tee, B. C.-K.; Giri, G.; Xu, J.; Kim, D. H.; Becerril, H. A.; Stoltenberg, R. M.; Lee, T. H.; Xue, G.; Mannsfeld, S. C. B.; Bao, Z. *Nat Mater* **2013**, *12*, 665–671.

41. Darling, S. B. *Energy Environ. Sci.* **2009**, *2*, 1266–1273.

42. Ku, S.-Y.; Brady, M. A.; Treat, N. D.; Cochran, J. E.; Robb, M. J.; Kramer, E. J.; Chabinyc, M. L.; Hawker, C. J. *J. Am. Chem. Soc.* **2012**, *134*, 16040–16046.

43. Johnson, K.; Huang, Y.-S.; Huettner, S.; Sommer, M.; Brinkmann, M.; Mulherin, R.; Niedzialek, D.; Beljonne, D.; Clark, J.; Huck, W. T. S.; Friend, R. H. *J. Am. Chem. Soc.* **2013**, *135*, 5074–5083.

44. Guo, C.; Lin, Y.-H.; Witman, M. D.; Smith, K. A.; Wang, C.; Hexemer, A.; Strzalka, J.; Gomez, E. D.; Verduzco, R. *Nano Lett.* **2013**, *13*, 2957–2963.

45. McCulloch, I.; Heeney, M.; Bailey, C.; Genevicius, K.; MacDonald, I.; Shkunov, M.; Sparrowe, D.; Tierney, S.; Wagner, R.; Zhang, W.; Chabinyc, M. L.; Kline, R. J.; McGehee, M. D.; Toney, M. F. *Nat Mater* **2006**, *5*, 328–333.

46. Luria, J. L.; Hoepker, N.; Bruce, R.; Jacobs, A. R.; Groves, C.; Marohn, J. A. *ACS Nano* **2012**, *6*, 9392–9401.

47. Smieska, L. M.; Pozdin, V. A.; Luria, J. L.; Hennig, R. G.; Hines, M. A.; Lewis, C. A.; Marohn, J. A. *Adv. Funct. Mater.* **2012**, *22*, 5096–5106.

48. Reid, O. G.; Rayermann, G. E.; Coffey, D. C.; Ginger, D. S. *J. Phys. Chem. C* **2010**, *114*, 20672–20677.

49. Chiesa, M.; Bürgi, L.; Kim, J.-S.; Shikler, R.; Friend, R. H.; Sirringhaus, H. *Nano Lett.* **2005**, *5*, 559–563.

50. Mastronarde, D. N. *Journal of Structural Biology* **2005**, *152*, 36–51.

Chapter 5

Real-Time Observation of Ion Motion in Conjugated Polyelectrolytes with Kelvin Probe Force Microscopy

5.1 Introduction

Conjugated polyelectrolytes (CPEs) are a unique class of materials whose semiconducting properties depend on the behavior of both electronic and ionic carriers. This mixed functionality arises from a chemical structure that comprises a conjugated polymer backbone and charge-functionalized alkyl side chains and counterions. CPEs are commonly used to modify electrode interfaces or as interlayers in organic light-emitting diodes,[1–6] organic transistors,[7] and organic[xiaAEM2011, 6,8–11] and perovskite[12] photovoltaic devices, where their solubility in polar solvents is well suited to fabricating solution-deposited multilayer structures with non-polar active layer materials. When used as thin

interlayers, the covalently linked charges on the CPE, together with their mobile counterions, adjust the energy level alignment between active layer and electrode. The cathode or anode functionality of the interlayer depends on the charge of the mobile species,[13,14] albeit with some exceptions.[15] Depending on the device application and CPE layer thickness, ions generate interfacial dipoles that are either static or that form dynamically through the rearrangement of mobile ions in an applied field.[1,6,16,17] The ions in CPEs also act as electrochemical dopants, and this occurs either as a result of rearranged mobile ions[18–20] or intrinsically, as with some anionic CPEs containing alkali metal counterions.[11] The capacity for high electrical conductivity and facile synthetic modification make CPEs promising for a number of mixed ionic electronic conductor (MIEC) device applications, including light-emitting electrochemical cells (LECs),[21–23] thermoelectrics,[24–26] biosensors,[27–29] supercapacitors,[30] and electronic ratchets.[31,32] For applications in electronic devices, it is important to understand both electronic charge and ion transport in CPEs. Techniques such as chronoamperometry,[19] pulsed bias sweeps,[20] and quantitative transient absorption[18] have typically been combined with modeling and simulation to describe electronic transport from current-voltage measurements. However, the presence of mixed electronic and ionic conductivity often complicates the transport description in CPEs. For example, ions can move under an applied field, causing current hysteresis in current density-voltage (J-V) sweeps. Ions can also increase electrical conductivity through doping that emerges as a result of redistribution of free counterions within the CPE bulk. Both the ionic and electronic transport properties therefore depend on the device history, making it difficult to extract parameters through methods described above. Correctly interpreting electronic transport from these experiments requires a known distribution of uncompensated ions, which is effectively the electrochemical doping profile. The extent of electrochemical doping in thick films (300-500 nm) of poly(fluorene-alt-co-phenylene) CPEs was estimated in hole-only diode structures through Mott-Guerney

analysis of very fast bias sweeps.[20] After bias stressing, changes in space charge limited current (SCLC) characteristics and capacitance measurements were consistent with doping through 80% of the film thickness. Another approach to estimating the doping profile was given by Walker and Lonergan,[18] who utilized quantitative cyclic voltammetry and polaron absorption to determine the total charge present in stressed CPE films. Based on the assumption of complete double-layer formation at the electrodes, the hole density profile was calculated from diffusion current to show moderate doping (10^{17}–10^{18} cm^{-3}) throughout the film. While both of these studies report an extensive electrochemical doping effect, they diverge in their description of the ionic dopant distribution and of bulk-limited electrical (hole) transport within stressed CPE films. Characterizing ion transport parameters in CPEs, specifically the conductivity, mobility, and the effective carrier concentration of the mobile ion species, can be particularly challenging. The typical approach of using transient current measurements can be instructive, and helps to at least establish qualitative trends in conductivity.[3,19,20,33,34] Impedance spectroscopy on parallel plate devices also provides an estimate of ionic resistivity in CPE films that can be carried out under low injection conditions, provided that the ionic conductivity can be definitively separated from that of electronic carriers. But determining an ionic mobility from conductivity also requires a known density of 'free' ions that is not trivially determined and does not necessarily follow from the total density of mobile ions, which is on the order of 10^{21} cm^{-3} in most CPEs. Rather, the density of free ions is lower than that because of the strong Coulombic binding interaction between ion pairs, which limits the number ions with sufficient energy to become free carriers at room temperature.[19,35] The binding energy is difficult to determine due to the complexity of the CPE environment, leading to ambiguity in the density of free ionic carriers that is a central problem in the study of CPE mobile ion transport properties. Quantifying ion transport in CPEs and other MIEC materials requires a method for circumventing or suppressing electrical

currents. Recently, the well known polymer:polyelectrolyte composite PEDOT:PSS was used to obtain high ionic and electrical conductivities in specialized, hydrated structures containing processed cellulose.[30] In order to measure ionic transport behavior, however, the authors replaced the conjugated polymer component with an insulating polymer. This highlights a challenge of studying mixed conductors, and particularly CPEs for which turning off electrical conductivity is not possible without significant changes to chemical structure. Elsewhere, the mobilities of cations in PEDOT:PSS have been measured by monitoring polaron absorption, which becomes quenched as cations diffuse into the material and compensate the sulfonate groups on the PSS.[27] While this technique provides a powerful method for observing the diffusion of extrinsic ions, it relies both on the high doping ratio and the lack of intrinsic mobile counterions in PEDOT:PSS, and therefore does not apply to the study of CPEs prepared with ion-blocking electrodes. Altogether, these limitations motivate the further development of in-situ techniques for observing ion rearrangement and transport in CPEs and in MIEC devices prepared with ion-blocking electrodes. In this paper, we study ion motion in CPEs by directly observing the time-dependent distribution of ions within CPE films using Kelvin probe force microscopy (KPFM). The KPFM technique uses electrostatic interactions to measure the contact potential difference between a sample and a conductive atomic force microscopy (AFM) tip. This technique has been used elsewhere to determine the operating mechanisms of planar light-emitting electrochemical cells[36–38] (LECs) and of ionic-organic ratchets,[31,32] systems that resemble CPEs in that they are prepared from a conjugated polymer mixed with a salt. In these devices, the distribution of resistive and conductive regions determined from the KPFM potential profile was used to identify lowered injection barriers, electrochemical doping,[36,39] and rectifying junctions.[31,32] Here, we use surface potential measurements to calculate the distribution of uncompensated ions—both covalently linked and mobile—within a planar, transistor-like device from the time

immediately following bias stressing until most ions return to their equilibrium positions. In addition, impedance spectroscopy of parallel plate device structures is also carried out to provide an independent measure of ionic conductivity. Monte Carlo (MC) simulations are then used to model the evolution of uncompensated ions during stress and relaxation, and these simulations allow the density of free ionic carriers and the ionic mobility to be estimated by fitting the experimental ionic relaxation behavior. Altogether, this work provides for the first time both an analysis of ion transport behavior in CPEs by multiple techniques and a direct visualization of the process of ion rearrangement.

To demonstrate the applicability of our approach to studying ion transport processes, we systematically study the impact of incremental changes in CPE chemical structure on the conductivity of mobile ions. CPEs containing a poly(fluorene-alt-co-phenylene) (PFP) conjugated backbone have been previously studied.[1,5,6,15,16,20,33] In this work, all six of the CPEs are built on a PFP backbone, but possess different side chain structures, as shown in **Figure 5.1**. PFN-P2-BIm_4, PFN-P4-BIm_4, and PFN-P6-BIm_4 are new structures. Each contains two phenyl-initiated side chains with 1, 2, or 3 alkoxy groups that are terminated by quaternary ammonium ions. The cations are paired with tetrakis(1-imidazolyl)borate (BIm_4^-), giving a ratio of 2, 4, and 6 mobile ions per monomer. The remaining three compounds studied here, referred to here as PFN-F, PFN-Br, and PFN-BIm_4, have identical polymer backbones and two alkyl side chains per monomer terminated by quaternary ammonium ions, but each contains a different mobile anion.

5.2 Visualizing ion distributions with KPFM

To study the one-dimensional movement of ions, KPFM measurements were carried out on planar, two-terminal devices with a 25 μm channel length and a geometry similar

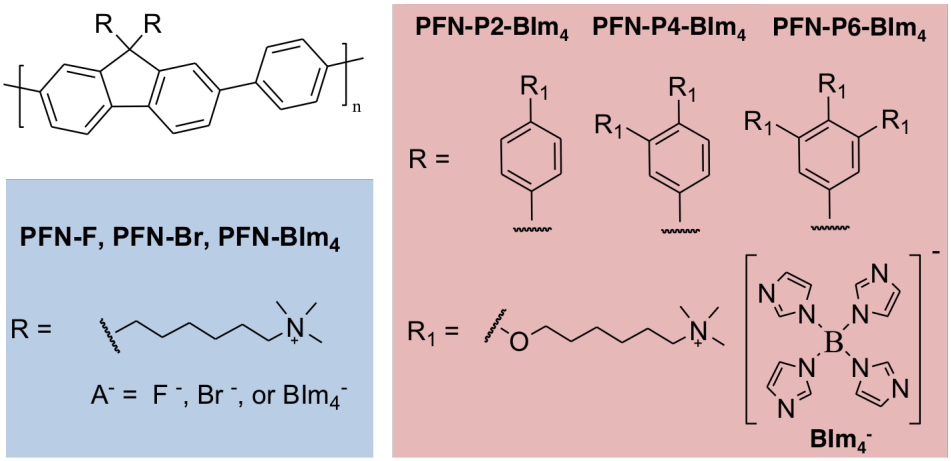

Figure 5.1: Chemical structures of the CPE materials. All compounds possess the same conjugated backbone structure, but vary in their side chain structure and ionic composition. PFN-F, PFN-Br, and PFN-BIm_4 are identical in structure except for their mobile counter anions, while PFN-P2-BIm_4, PFN-P4-BIm_4, and PFN-P6-BIm_4 each have 2, 4, or 6 covalently linked cations per monomer

to a field effect transistor (FET), but without a gate electrode. In this electrode configuration, applying a bias leads to a longitudinally distributed electric field. As with previous studies,[5,18,20] a relatively high strength of electric field ($10^4 - 10^5$ V cm^{-1}) was necessary to induce ion rearrangement. The associated voltages (60-200 V), applied from an external voltage source, cause a surface potential that exceeds the measurement range of the KPFM ($\pm$ 9 V). Therefore, the channel potential was measured immediately (<1 s) after removing the bias, and the distribution of ions was characterized through the subsequent period of relaxation. When both electrodes are grounded immediately following the bias stress ($t = 0$), a time-dependent potential profile of the channel is measured using KPFM. The time resolution dt is determined by the time of a line scan of the full channel (the CPE film between electrodes), and it is limited to $dt \sim$1 s by the scanning speed for which sufficient quality can be obtained. The measured potential profile of each line scan, $V(x,t)$, was used to calculate the electric field distribution, $E(x,t)$, and the charge density profile, $\rho(x,t)$, through the numerical derivative or second derivative,

respectively, according to the electrostatic 1-D Poisson equation:

$$\frac{dV(x,t)}{dx} = -E(x,t) \tag{1}$$

$$\frac{d^2V(x,t)}{dx^2} = \frac{-q\rho(x,t)}{\epsilon_0\epsilon_r} \tag{2}$$

Here, ϵ_0 is the permittivity of free space, ϵ_r is the relative dielectric constant, and q is the elementary charge. The observed distribution of charge in the film, $\rho(x,t)$, is due to uncompensated charges at the time of each line scan. These charges may represent ions and/or electronic carriers, as well as image charges within the electrode at the CPE-electrode interface. As we show below, one is able to determine the type of charged species by taking into account both the sign of charges and their position within the channel with respect to the applied stressing field. To illustrate how the data are interpreted, we first present the topography and potential profile as measured before the application of bias stress. **Figure 5.2a** and **Figure 5.2b** show height and surface potential images, respectively, obtained by KPFM on a PFN-Br film. The stability of the potential profile throughout the image, which is scanned from top to bottom, reflects an unchanging charge distribution throughout the scan. The potential profile and the calculated electric field and charge density profiles are plotted along with channel topography in **Figure 5.2c** as the average of 100 scan lines. The profile across the channel is approximately symmetric, being equal at the left and right gold electrodes and leveling off in the middle of the channel. The corresponding $\rho(x)$ trace shows a buildup of negative charge within the film near the electrode interfaces, possibly due to uncompensated Br^- ions. Adjacent to these ions along the metal-CPE interface is a narrow distribution of positive charge that is attributed to image charge induced by the nearby Br^- anions. The spontaneous

attraction of mobile ions to their image charges has been proposed elsewhere as the mechanism responsible for establishing interfacial dipoles in CPE interlayers, particularly in OPV applications at low external electric fields,[14,17] and this effect is observed for all of the cationic CPEs studied here. While the potential profile is similar to the band bending that often occurs due to diffused charge carriers,[40] a mismatch in work function between vacuum-deposited gold bottom contacts (∼4.7 eV)[41] and the deep HOMO energy level of PFP (5.6-5.8eV)[20,42] suggests that this effect is unlikely.

Figure 5.3a shows the time evolution of the potential profile in the channel for a PFN-P4-BIm_4 device beginning immediately after the release of a +150 V stress to the left electrode for 10 minutes. The y-axis in this colormap image represents both position and the approximate time after the release of the bias stress, where the 1 second between scan lines corresponds to a distance of ∼68 nm along the channel. In **Figure 5.3b**, line plots show the channel potential during the relaxation process, progressing from color red (∼1 second) to violet (161 seconds) by 2-second intervals. The potential in the channel near the stressed (left) and grounded (right) sides of the channel is initially opposite in curvature, but eventually approaches a symmetric shape similar to that observed in the unstressed PFN-Br device (Figure 5.2c). In **Figure 5.3c**, line plots show the evolution of charge density after releasing the stress, as calculated from Equation (2). The distribution of uncompensated charges is consistent with the polarization of BIm_4^- ions towards the positively stressed electrode, which leaves behind a population of uncompensated R-NMe_3^+ ions seen near the grounded electrode on the right. As in Figure 5.2c, charge within the electrodes is taken to represent image charges induced by ions near each interface. Even though accumulated mobile ions near the electrodes experience strong electrostatic and steric repulsion, the majority of the channel in which ions propagate during relaxation is charge-balanced. The stressed charge distribution in Figure 5.3c is qualitatively similar to the ion profile determined elsewhere through modeling of films

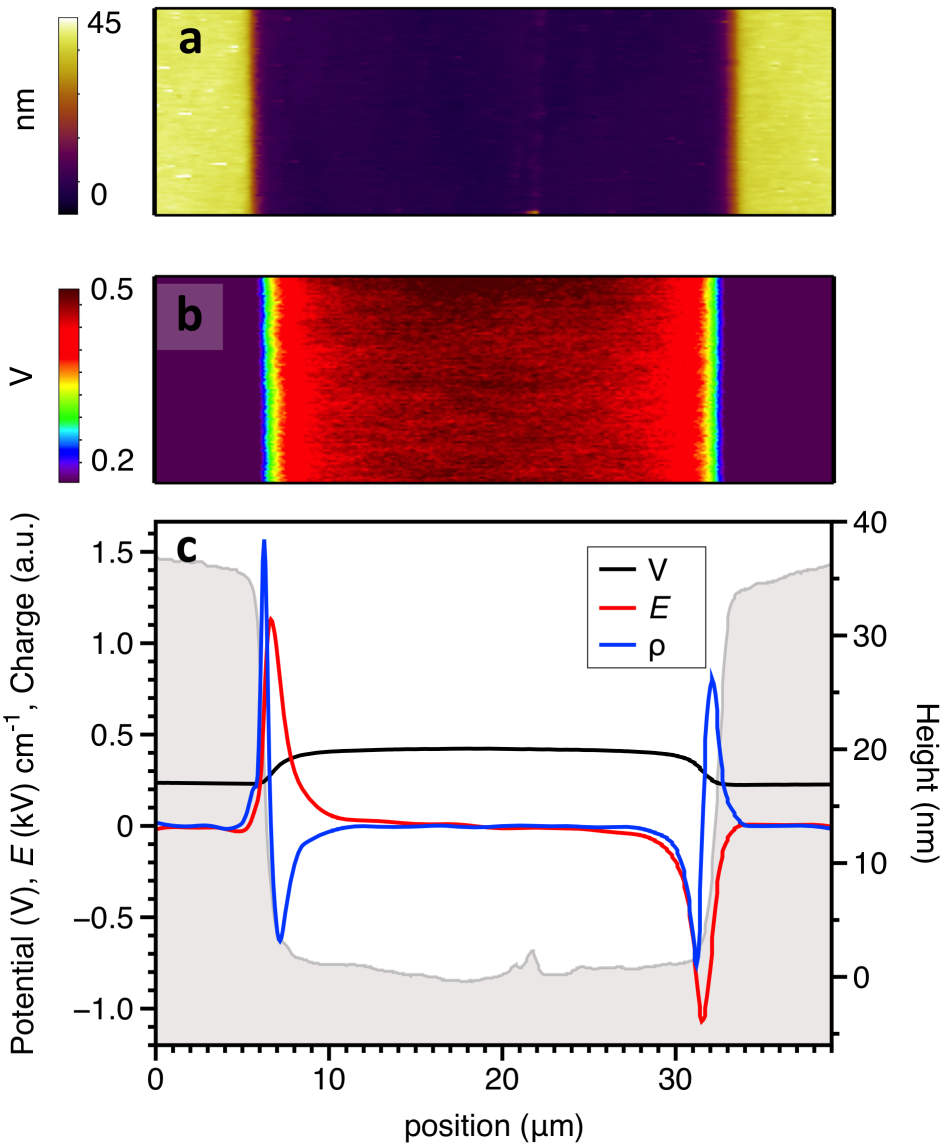

Figure 5.2: a) Height and b) potential colormap images obtained by KPFM of an unstressed, 20 nm PFN-Br film spin-casted onto a quartz substrate with 35 nm evaporated gold contacts. A 25 μm channel is created by a wire shadow mask held to the quartz surface. Total scan area is 39 μm x 7.5 μm. c) Plot of surface topography (gray) obtained as the average of 100 scan lines from a), along with contact potential difference (black), calculated electric field (red), and calculated charge density (blue) obtained from the same scanning region as in b).

with high ion density ($> 10^{21}$ cm^{-3}), in which interfacial double layers and an extensive neutral region were also observed.[43]

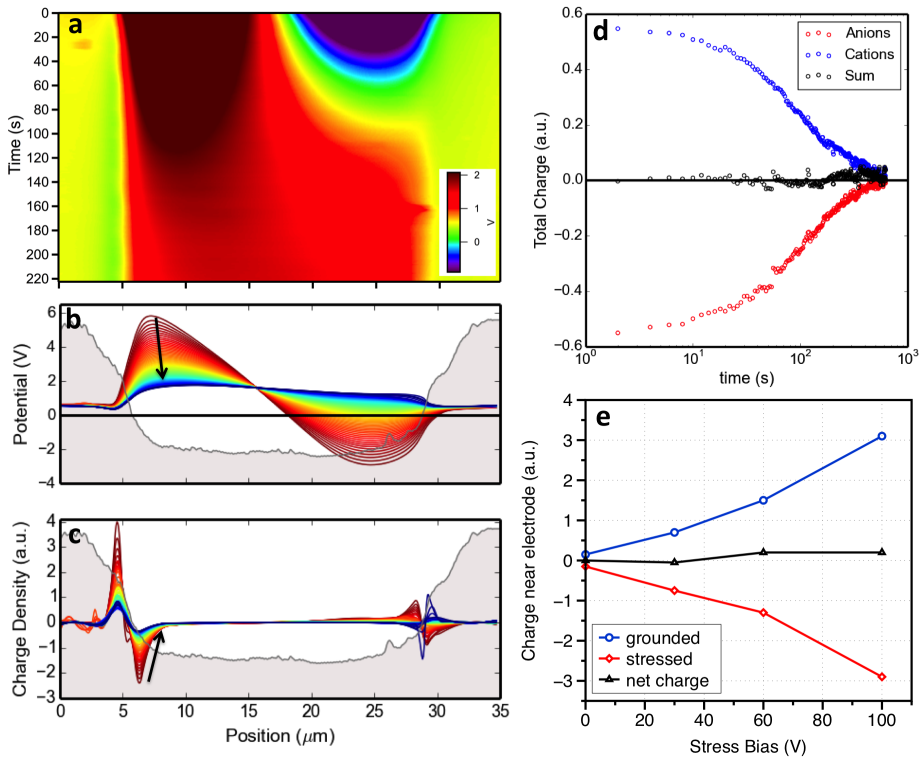

Figure 5.3: a) KPFM potential colormap image of a PFN-P4-BIm$_4$ film bias-stressed for 10 minutes at 150 V, where the left axis is transposed from position to time. Scan dimensions are 34.7 μm x 15 μm. b) Line plots of potential and c) calculated charge density taken at 2 second intervals from ~1 second (red) until ~161 seconds (violet) after removing the bias stress, with outline of channel topography shown for reference (channel height is 20 μm). d) Integrated anion (red), cation (blue), and total charge populations in the channel as a function of relaxation time. e) Total ionic charge near stressed (red) and grounded (blue) electrodes and total charge within channel at $t = 0$, plotted as a function of applied voltage for a 10 minute bias stress.

It is important to consider the extent to which injected charges affect the observed charge density profile. The current through the device was low, and decreased over the course of the bias stress until saturating at a constant value. This observation is consistent with ion migration, leading to a buildup of ions that eventually screens the internal field. The initial post-stressing charge distribution seen in Figure 5.3c (dark red) is consistent

with a buildup of ions at each interface and a lower density tails of both cations and anions extending into the channel. Any electronic charge, which would be opposite in sign to the observed distribution, is not observed directly, but would instead suppress the apparent ion density through charge compensation. The observation of ionic species and not free charges can be further validated by comparing the total charge of the anion depletion region near the grounded electrode to the total accumulation charge of near the stressed electrode. Figure 5.3d shows that the integrated charge near the grounded (blue trace) electrode is nearly equal to that present at the stressed (red trace) electrode, and that these charge populations in parallel during ion relaxation following a 10 minute voltage stress of 150 V. The amount of charge near each electrode is also proportional to stress bias (**Figure 5.3e**), while the total charge within the channel remains balanced. The decays observed in Figure 5.3d are then representative of anions returning to their equilibrium positions, which is ultimately determined by the diffusivity (and through the Einstein relation, the mobility) of the mobile ions. Even though accumulated mobile ions near the electrode experience strong electrostatic and steric repulsion, the majority of the channel in which ions propagate during relaxation is charge-balanced. Because the decay occurs in parallel at each electrode, it therefore corresponds to ions moving through the bulk of the film. By comparing the decay transients of different CPE materials, it is then possible to extract the parameters that determine ionic drift-diffusion and establish trends in ion transport properties.

5.3 Ion relaxation and charged side chain density

The channel potential was next measured for PFN-P2-BIm_4 and PFN-P6-BIm_4 devices using the stressing routine described previously for PFN-P4-BIm_4. The post-stress potential profiles in the PFN-P2-BIm_4 and PFN-P6-BIm_4 films, shown in **Figure 5.4**,

are qualitatively similar to PFN-P4-BIm_4, and both show approximately no net charge within the channel and a synchronous decay of positive and negative charge populations near the electrodes. In **Figure 5.5**, the integrated anionic charge near the stressed electrode is plotted as a function of time after the release of the bias stress for PFN-P2-BIm_4, PFN-P4-BIm_4, and PFN-P6-BIm_4. The anionic charge in each film is fit to an exponential decay, giving decay lifetimes (τ) of 232 seconds, 66 seconds, and 8 seconds for PFN-P2-BIm_4, PFN-P4-BIm_4, and PFN-P6-BIm_4, respectively. The decay behavior is quite repeatable for multiple stress cycles carried out on the same sample, while variation in decay rate between experiments on different samples showed results within $\pm$ 30 seconds, $\pm$ 9 seconds, and $\pm$ 2 seconds of those provided here for PFN-P2-BIm_4, PFN-P4-BIm_4, and PFN-P6-BIm_4, respectively. These error values are small in comparison to differences in decay time between each of the materials.

Also shown in Figure 5.5 are fits obtained numerically from Monte Carlo simulations of mobile ions during stress and relaxation. In this simulation, drift-diffusion of ions is modeled, where ion mobility and the free ion carrier density (not the total density) are the fitting parameters that determine the decay behavior. The shape of the anion decay is well represented by this model, indicating that no additional complexity is needed in order to recreate the ion relaxation behavior. These simulations are presented below in further detail. To connect the observed ion relaxation behavior to a process of thermally-activated ion hopping, the temperature dependence of the KFPM decay transients was measured using a heated sample stage for planar devices using PFN-P2-BIm_4, PFN-P4-BIm_4, and PFN-P6-BIm_4. The decay of stressed devices was measured after bias-stressing for 3 minutes at 80 V at temperatures ranging from 25 °C to 60 °C. We observe Arrhenius behavior in accordance to a previous study of ion conduction measured by impedance spectroscopy, which showed highly temperature-activated ionic transport in CPEs.[35] The decay lifetimes were in this case determined from the time at which potential was no

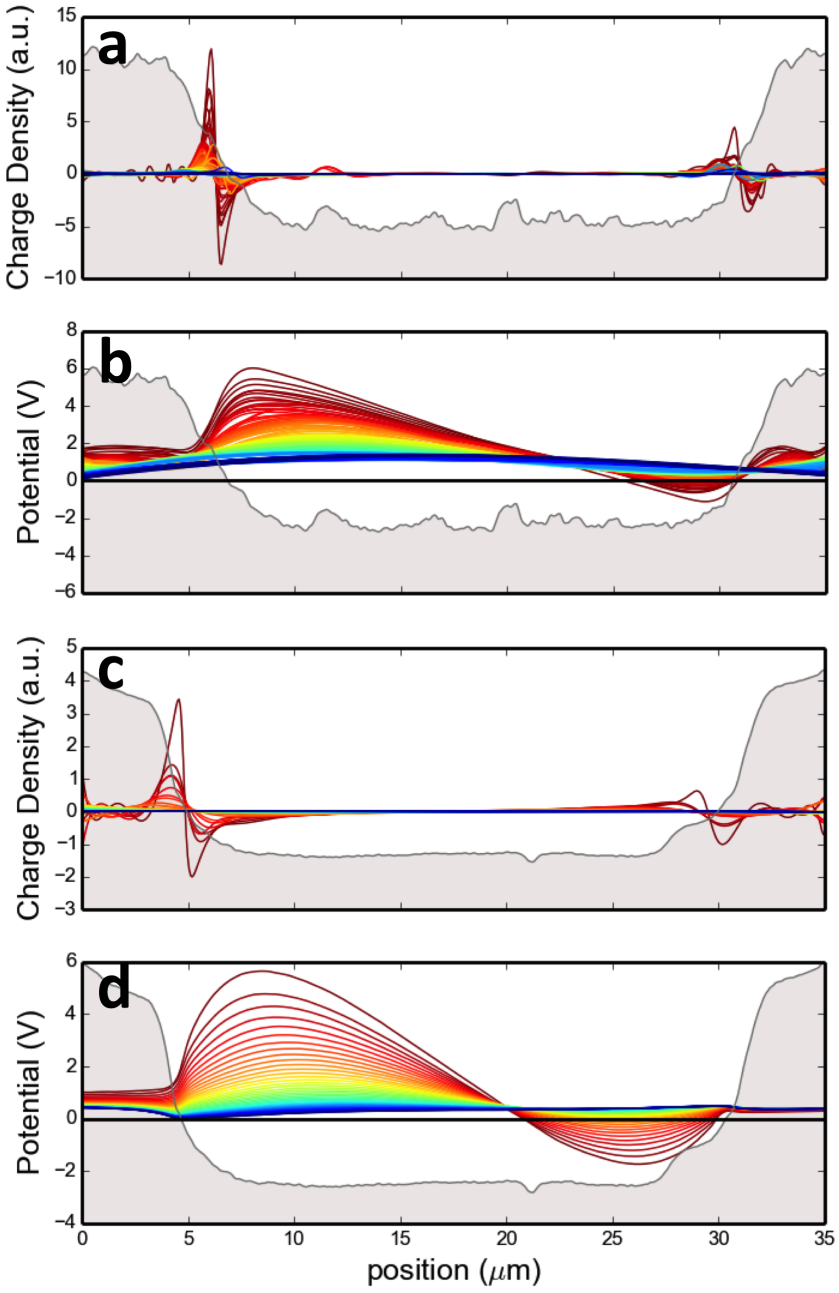

Figure 5.4: Charge (a,c) and potential (b,d) profiles immediately after release of a 15-minute, 100 V bias stress for films of PFN-P2-BIm$_4$ (a,b) and PFN-P6-BIm$_4$. Lines progress from red to blue, showing scans at two second intervals from 1 to 701 seconds after release of bias stress for PFN-P2-BIm$_4$ (a,b) and at 1 second intervals from 1 to 40 seconds in PFN-P6-BIm$_4$ (c,d).

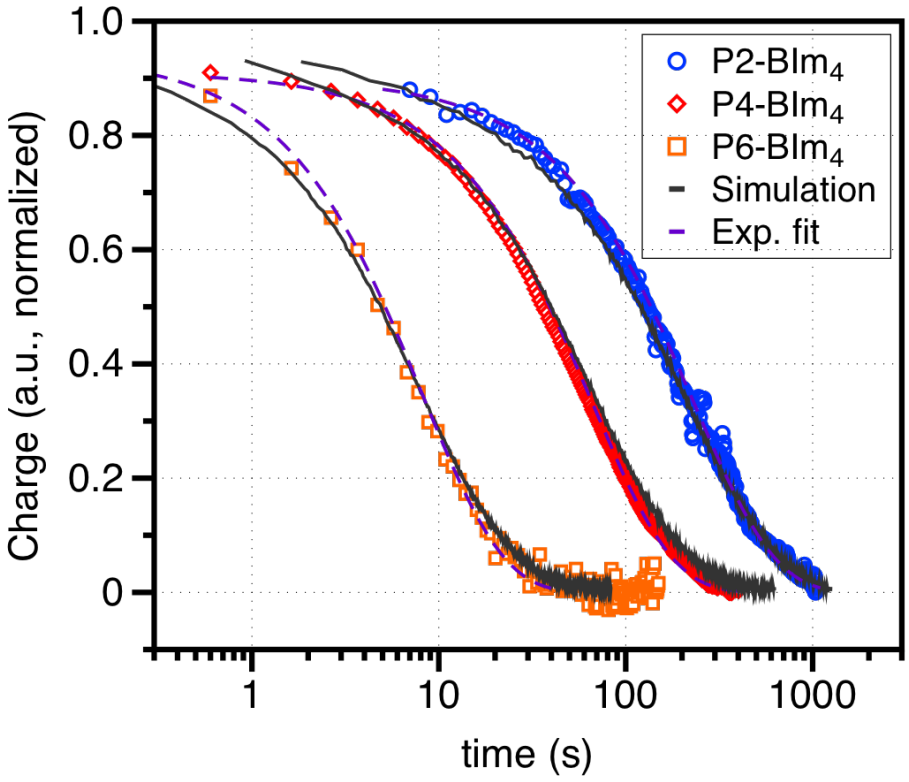

Figure 5.5: Integrated anionic charge near stressed electrode plotted vs. scanning time on lin-log scale. Data are fit to a single exponential decay, as well as by optimization of Monte Carlo simulation by varying the effective free carrier density and the ion mobility.

longer significantly changing. Because ions must travel approximately the same distance in returning to their equilibrium positions, the decay rate, $\frac{1}{\tau}$ (s^{-1}), serves as a proxy for conductivity or diffusivity, leading to the following equation for Arrhenius behavior of relaxation times:

$$\frac{1}{\tau} = \frac{1}{\tau_0} \exp\left(-\frac{E_A}{kT}\right) \tag{3}$$

Here τ_0 is the asymptotic relaxation time at very high temperatures, T is temperature, k is the Boltzmann constant, and E_A is activation energy. The decay rate was plotted as a function of temperature and fit to Equation (3) to determine E_A for the ion relaxation, shown in **Figure 5.6**. The extracted activation energies are 0.41 eV in PFN-P6-BIm_4, 0.60 eV in PFN-P4-BIm_4, and 0.78 eV in PFN-P2-BIm_4. These numbers are consistent with the relaxation of the three 25-μm devices seen in Figure 5.5, suggesting that CPEs with larger relaxation times, τ, also show larger activation energies. Activation energies were also determined from temperature-dependent impedance measurements (see Appendix C.2, Figure C.2) of ionic conductivity over the range T = 295 K to T = 404 K. (Table 5.1). Although the error bars in the temperature-dependent decay lifetime determined by KPFM are quite large (Figure 5.6), the trend in the activation energies obtained from impedance and from temperature-dependent KPFM experiments is quite similar, suggesting that even though these experiments are carried out under different circumstances, the same temperature-activated ion hopping process is probed. For comparison, $CF_3SO_4^-$ ions in cationic polyacetylene (PAC) showed an activation energy of 0.94 eV in vacuum-dried films at room temperature.[35] It is possible to correlate the trend in activation energies to the increase in ions per monomer. However, it is not the total ion density, but rather details of the side-chain structure that differ most significantly between these materials. X-ray reflectivity (XRR) measurements show that mass density remains relatively constant at about 1.2 $\pm$ 0.1 g/cm^3 in all three materials (see Appendix

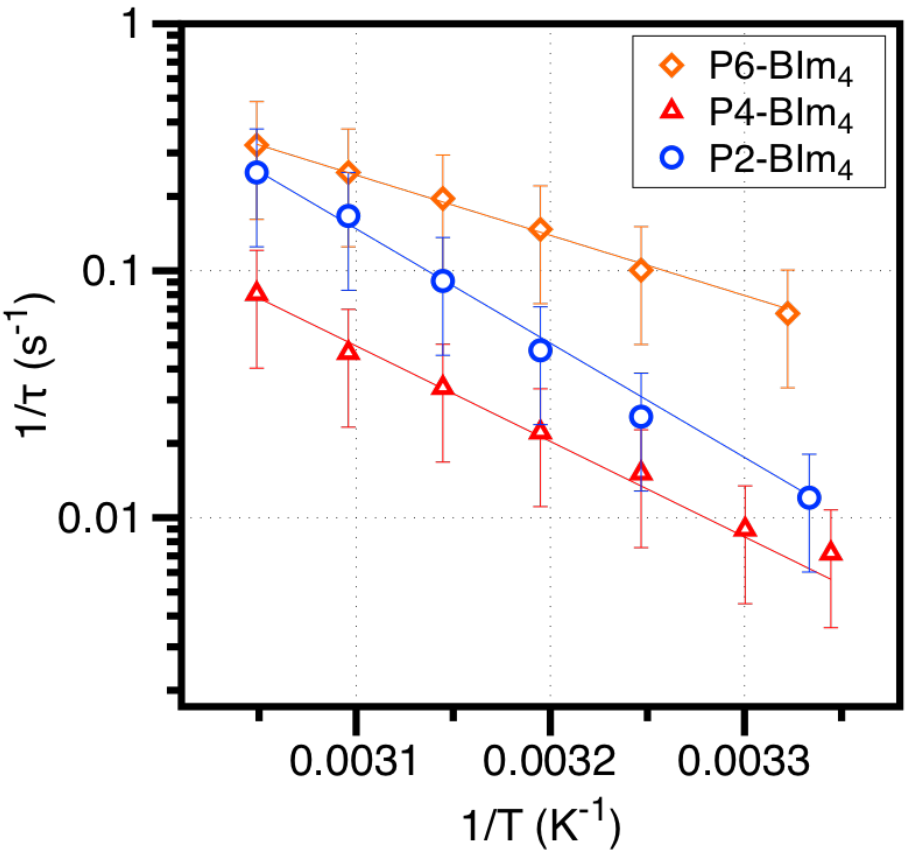

Figure 5.6: Plot of the inverse of exponential decay lifetime ($\frac{1}{\tau}$) as a function of inverse temperature after applying an 80 V bias stress for 3 minutes, with fits to Equation (3). The channel length used here for the PFN-P2-BIm_4 device ($\sim$18 μm) was shorter than that of the PFN-P6-BIm_4 and PFN-P4-BIm_4 devices (25 μm), causing a comparatively faster decay time in PFN-P2-BIm_4 compared to PFN-P4-BIm_4 at room temperature.

C.3, Figure C.4). At the same time, the increase in monomer mass that accompanies the addition of ionic side chains and counter ions causes a decrease in the number density of monomers in the film. As a result, the total ion density in the film is relatively unchanged, varying only between $1.3\times10^{21}cm^{-3}$ and $1.4\times10^{21}cm^{-3}$ from P2-PFN-BIm_4 to P6-PFN-BIm_4. From the simplified assumption that total ion density is proportional to conductivity, these small density differences cannot account for ion relaxation times that vary by more than a factor of 20. More significant is the structural change that accompanies the addition of more sidechains, which increases the volume occupied by alkyl chain and ionic species within each monomer. The importance of side-chain structure to the ion transport is also supported by comparing the activation energies in this series with that of PAC,[35] all of which are found to be amorphous materials (see Appendix C.4, Figure C.5). The activation energy in PAC was larger (0.94eV), despite the higher stoichiometric density (2.1×10^{21} cm^{-3}) and smaller radius of its $CF_3SO_4^-$ ions, which would otherwise both be expected to provide faster ion hopping. The impact of side chain structure can then be understood by considering that ion transport requires pathways to be opened up within a densely packed material. In the case of $BIm_4{}^-$, this requires considerable local rearrangement of the polymer. Because long alkyl chains exhibit greater vibrational motion and possess more degrees of freedom at room temperature than the sp^2 carbons on the conjugated backbone,[44] increasing the overall proportion of alkyl groups improves the transport of bulky ions. At the same time, the increased presence of ions in the aliphatic part of the molecule may provide partial screening of charge pair interactions, lowering the average binding energy between ion pairs. A better understanding of this mechanism would require separating the contributions of ion pair binding energy from the activation of ion hopping, which is beyond the scope of this study.

5.4 Ionic conductivity from Impedance Spectroscopy

To obtain an additional and complimentary measure of ion transport properties, impedance spectroscopy experiments were carried out on vertical, parallel plate device structures (diode electrode configuration). Low frequency impedance of CPEs is generally representative of ions at small AC voltage amplitudes ($\leq$ 100 mV) near short-circuit conditions, where the electronic injection is minimal. The conductivity spectrum, $\sigma'(\omega)$, where ω is the radial frequency $\omega = 2\pi f$, is estimated from the real component of the impedance, Z', as $\sigma'(\omega) = \frac{1}{Z'(\omega)}$. In a typical ionic conductor, the peak in the dielectric loss tangent, equal to $tan(\delta) = \frac{\epsilon''}{\epsilon'}$, occurs at the frequency at which most ions begin responding to the field. Also seen around this frequency is a plateau in the real conductivity, and the value of this plateau has been used elsewhere to estimate conductivity in CPEs.[35] **Figure 5.7a** shows averaged conductivity spectra obtained for 8 different PFN-P2-BIm_4 devices with thicknesses ~160 nm (N = 2) or ~450 nm (N = 6). The dashed line represents the best y-value fit to the plateau for all spectra, with a value of 3.5×10^{-12} S cm^{-1}. The same analysis was applied to PFN-P4-BIm_4 and PFN-P6-BIm_4 devices to obtain average room temperature ionic conductivities of 2.1×10^{-11} and 9.8×10^{-11} S cm^{-1}, respectively. These values represent the effective ionic conductivity, σ_{ion}, which should be inversely proportional to the lifetime measured by charge decay from KPFM. In **Figure 5.7b**, the decay rate, $1/\tau$, is plotted on a log-log scale as a function of σ_{ion}, along with a plot of the line $\sigma_{ion} = 1/\tau$ to guide the eye. The direct relationship between $1/\tau$ and σ_{ion} illustrates an excellent qualitative agreement between the ion transport characteristics determined through KPFM and impedance experiments. This further confirms that the behavior observed in the KPFM profile can be attributed to ion relaxation.

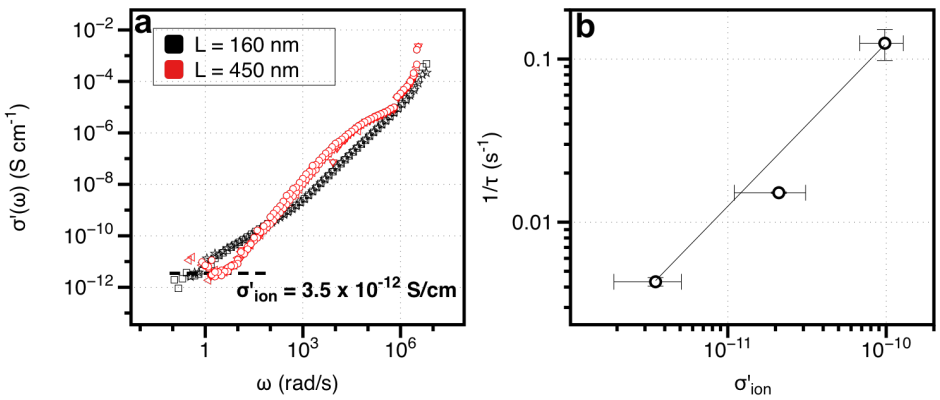

Figure 5.7: a) Conductivity spectra for 8 PFN-P2-BIm$_4$ devices, with thicknesses of either 160 nm or 450 nm. Plateau region is fit to obtain approximate ion conductivity. b) Decay rate, $^1/_\tau$, from KPFM ion relaxation plotted as a function of ionic conductivity determined by impedance spectroscopy on log-log scale, with plot of y=x to guide the eye and to demonstrate linear correlation where infinite decay time correlates to zero conductivity.

5.5 Monte Carlo simulations of ion relaxation

In order to obtain a further understanding of the ion transport behavior observed in KPFM, the ion relaxation behavior was modeled through a Monte Carlo simulation. In the model, the charges present in the simulation are initially homogeneously distributed throughout the film as point charges, with an equilibrium density equal to the density of free ionic carriers. During stress, charges redistribute through the channel and accumulate near the respective electrodes until the external field is fully screened. The ions are allowed to occupy a density of up to 1 per nm^{-3}. Upon releasing the bias, ions then move through both drift and diffusion until they reach an equal concentration throughout the film. In both simulation and the experiment, the stressing is carried out until the external is fully screened, however, the distribution of charge is much more narrow in the Monte Carlo simulation. To maintain consistency between the simulation and experiment, the decay behavior is monitored by integrating the entire ion population near the electrode in each case. The decay then reflects the transit of ions across the length of the

Table 5.1: Decay lifetime, τ(s), and activation energy from KPFM, $E_{A\text{-}KP}$; room temperature conductivity, σ_{ion}, and activation energy from impedance spectroscopy, $E_{A\text{-}IS}$; effective free ionic carrier density ρ, ionic mobility, μ, and conductivity product calculated as $\rho \times q \times \mu$, from Monte Carlo simulations to KP charge decays.

Polymer	τ(s) (S cm^{-}1)	σ_{ion} (eV)	$E_{A\text{-}KP}$ (eV)	$E_{A\text{-}IS}$ (cm^{-3})	ρ (cm^{2}V^{-1}s^{-1})	μ (S cm^{-}1)	$\rho \times q \times \mu$
PFN-P2-BIm$_4$	232	3.8×10^{-12}	.78	.71	1.0×10^{18}	2×10^{-11}	3.2×10^{-12}
PFN-P4-BIm$_4$	66	2.1×10^{-11}	.60	.61	1.5×10^{18}	7×10^{-11}	1.7×10^{-11}
PFN-P6-BIm$_4$	8	9.8×10^{-11}	.41	.45	2.0×10^{18}	4.5×10^{-10}	1.4×10^{-10}

channel, where the distance traveled can be related to the distance between the average distributions of positive and negative charge. The narrower distribution of ions in the Monte Carlo simulation may effectively increase the transit distance, which can lead to a slight overestimate of the transport parameters when fitting to the experimental data. Through fitting the measured charge relaxation dynamics using the Monte Carlo simulation (Figure 5.5), we obtain the ion mobility, μ, and the 'free' ionic carrier density, ρ, in CPE films, which are the two fitting parameters in the solution. The values obtained for PFN-P2-BIm$_4$, PFN-P4-BIm$_4$, and PFN-P6-BIm$_4$ are shown in Table 5.1. Both fitting parameters are inversely correlated with decay lifetime such that their product is the determining factor in obtaining a good fit, and this affords some flexibility in obtaining a reasonable match to the experimental data. As such, parameters were chosen in order to provide a good fit between simulation and experiment while simultaneously obtaining agreement between σ_{ion} and the conductivity calculated from the product of mobility and density fit parameters, yielding good agreement (Figure 5.5, Table 5.1). While a number of simplifying assumptions are made in the Monte Carlo simulation, the quantitative agreement between the experimental and simulated charge decay suggests that no further complexity is needed to provide a reasonable description of the system. A detailed description of these simulations is provided in Appendix C.1.

The best fit to the charge decay transients using our approach occurs at free ion carrier densities much lower than the stoichiometric density, at around 10^{18} cm^{-3}. In order to understand how such a low free ion carrier density could come about, the impact of strong Coulombic binding interactions between ion pairs should be considered. The relatively low dielectric constant of CPE materials[20] suggests that there is only weak screening of interactions between ions, and therefore the creation of free ion pairs requires an effective thermalization of ionic carriers from their bound states. For example, by simple Boltzmann treatment of bound and free mobile ion states, an estimated population of free carriers that is 1 in 1000 of the total ions corresponds to an ion pair binding energy of 175 meV. The activation energy for transport determined through temperature-dependent measurements includes within it the convolution of the ion hopping activation energy and the binding energy for ion pair creation. Computational studies of binding pair interactions that take into account ion size as well as the surrounding environment are beyond the scope of this work, but would be valuable in obtaining an independent estimate of the binding pair energy.

5.6 Effect of mobile ion size on ionic conductivity

Transient current behavior in CPEs has generally shown an inverse relationship between ion conductivity and the radius of the mobile ion. One notable exception is that, despite being smaller in size, the apparent ionic conductivity of the F^- ions in PFN-F was found to be lower than that of Br^- ions in PFN-Br, at least according to the time required for electrochemical doping to become saturated.[20] One of the suggestions for this deviation was a stronger binding interaction between the F^- ion and the quaternary ammonium charge, which could offset the difference in mass and ionic radius by increasing the energetic cost of separating ion pairs. The ion stress-relaxation dynam-

ics of PFN-Br, PFN-F, and PFN-BIm_4 devices were tested by KPFM to reveal decay lifetimes of 20 s, 24 s, and 36 s, respectively, as shown in **Figure 5.8**. Room temperature conductivity was also measured by impedance spectroscopy, and the resulting σ_{ion} values are 2.6×10^{-11} S cm^{-1}, 1.8 $\times10^{-11}$ S cm^{-1}, and 1.2 $\times10^{-11}$ S cm^{-1} for PFN-Br, PFN-F, and PFN-BIm_4, respectively. As observed with the series varying in ions per monomer, σ_{ion} values are directly proportional to the KPFM relaxation times. While this trend in conductivities is consistent with previous observations,[20] the effect of ion size on conductivity appears to be much smaller than that of varying the ion-bearing side chain density on the CPE. At the same time, the conductivity of PFN-P6-BIm_4 is even higher than the halide-containing PFN-X molecules. The ability of BIm_4^- to obtain relatively high conductivity despite its large size may be due to relatively weak ion pairing binding between BIm_4^- and R-NMe_3^+ ions, which would offset the retarding effects of its large volume and mass. Because the binding energy depends inversely on the separation between charges, it would be lowered by the large BIm_4^- radius. At the same time, the negative charge on the borate is likely to be shared among the strongly accepting imidazolyl groups, further decreasing the stability of the bound pair. A deeper understanding of the relationship between ion pair interactions, ionic transport, and local polarizability is needed.

5.7 Conclusions

In this work, we have demonstrated a new approach for using KPFM to directly visualizing ion dynamics in CPE films that affords an estimate of the static ion distribution under bias stressing conditions and characterizes ion transport. We found that the rate at which ions relax in CPE films containing a bulky mobile ion, BIm_4^-, was directly correlated to the number of ion-bearing sidechains (per repeat unit), and that

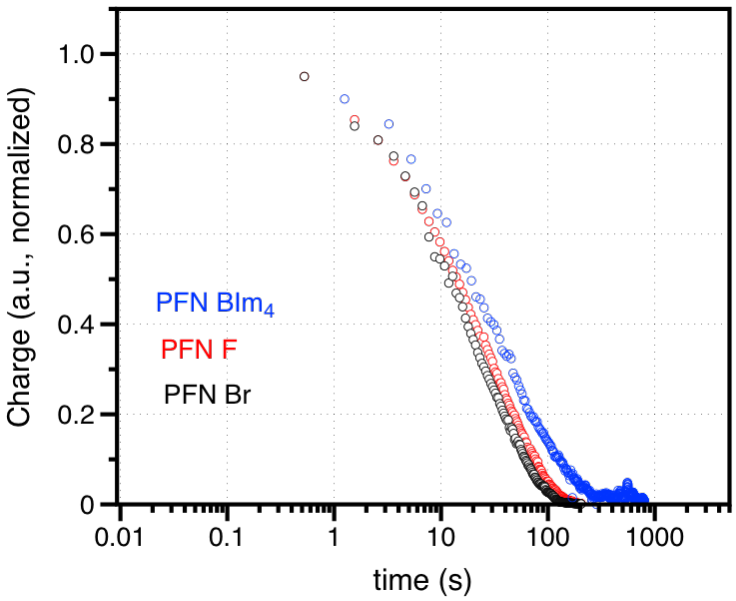

Figure 5.8: Charge decay transients measured near the stressed electrode by KPFM for planar devices prepared with 20 nm-thick films of PFN-BIm_4, PFN-F, and PFN-Br.

the relative composition of sidechains has a strong effect on the activation energy for ion hopping. While ionic conductivity showed a slight dependence on mobile ion size, even bulky anions were able to achieve high conductivities when the material was able to dynamically open up pathways for conduction through the vibrational motion of its side chains. The rate of relaxation obtained from KPFM was directly proportional to the conductivity determined by impedance spectroscopy, as were the apparent ion hopping activation energies, suggesting that the ion transport probed by the KPFM visualization is directly related to bulk transport properties measured through techniques at lower electric fields. Monte Carlo simulations were able to recreate the process of ion relaxation to yield estimates of ion mobility and the effective free carrier density of ions, providing a path to better understanding ion pair interactions in CPE films. Our findings further demonstrate the critical role of side chains in designing new materials with higher ionic conductivity. The methods described herein have decoupled the behavior of ionic and electronic carriers, thus providing a promising route to characterizing the motion of ions

in other mixed ionic-electronic transport materials.

5.8 Experimental Section

Synthesis and Preparation of Conjugated Polyelectrolytes: Precursor polymers for PFN-P2-BIm_4, PFN-P4-BIm_4, and PFN-P6-BIm_4 containing alkoxy side chains terminated by quaternary ammonium ions (R-NMe_3^+) but with bromide counter ions (Br^-) were synthesized by following a previous report.[6] In order to carry out ion exchange, precursor polymer (100mg) was dissolved in 10 mL of methanol, and an excess amount of sodium tetrakis(1-imidazolyl)borate was then added. The mixture was stirred at room temperature for 1 hour, after which the polymer was purified through dialysis against a cellulose tube with a molecular weight cut-off of 5,000 g/mol in deionized water. The addition of sodium tetrakis(1-imidazolyl)borate in methanol was repeated 2-3 times to complete the counter ions exchange. Finally, the resulting polymer was dried under vacuum to yield PFN-P2-BIm_4, PFN-P4-BIm_4, and PFN-P6-BIm_4. PFN-P2-BIm_4: Yield (89%); Number average molecular weight (M_n) = 11.9 kDa, polydispersity index (PDI) = 2.1; 1H NMR (400 MHz, DMSO) δ (ppm) 8.07 (b, 2H), 7.70 (b, 8H), 7.14 (b, 4H),7.02 (s, 8H), 6.91 (s, 8H), 6.85 (b, 4H), 6.75 (s, 8H), 3.89 (b, 4H), 3.23 (b, 4H), 3.01 (s, 18H), 1.65 (b, 8H), 1.41 (b, 4H), 1.28 (b, 4H). (Number average molecular weight (Mn) of the polymers was determined before ionization). PFN-P4-BIm_4: Yield (92%); M_n = 12.3 kDa, PDI = 2.1; 1H NMR (400 MHz, DMSO) δ (ppm) 8.12 (b, 2H), 7.75 (b, 10H), 7.02 (s, 16H), 6.91 (s, 16H), 6.87 (b, 6H), 6.74 (s, 16H), 3.88-3.28 (b, 16H), 3.03 (s, 36H), 1.60-1.10 (m, 32H). PFN-P6-BIm_4: Yield (90%); M_n = 14.2 kDa, PDI = 2.3; 1H NMR (400 MHz, DMSO) δ (ppm) 8.11 (b, 2H), 7.79 (m, 8H),7.02 (s, 24H), 6.90 (s, 24H), 6.74 (s, 24H), 6.50 (b, 4H), 3.75-3.20 (b, 24H), 3.04 (s, 54H), 1.75-1.10(b, 48H). The PFN-Br polymer was synthesized according to the procedure described previously,[45] after which

an ion exchange similar to that described above was carried out to obtain PFN-F and PFN-BIm_4.

Device preparation: Planar devices used in KPFM measurements were prepared on quartz substrates 10 mm x 10 mm in size cut from a 1 mm-thick wafer. Substrates were scrubbed with detergent, then sonicated for 10 minutes each in DI water, acetone, and isopropyl alcohol, then baked at 150 °C overnight. Device electrodes were outlined with clear tape to make two pairs of 2.5 mm x 4 mm electrodes, and aluminum wire $\sim$25 μm in diameter was affixed to the substrate surface to define a channel. Large electrode areas were used to accommodate large AFM sample stage probes with fixed dimensions. A 35 nm gold layer was thermally evaporated onto the masked quartz substrates, and substrates were cleaned by sonication in DI water, acetone, and isopropanol for 20 minutes each. CPE materials were transferred into an N_2-filled glovebox and dissolved at 5 mg/mL in 99.9% dry ethanol, and solutions were heated overnight at 60 °C. Device substrates were cleaned in O_2 plasma for 5 minutes, and the CPE solutions were spin-coated onto them in the glovebox at 1500 rpm. Film thicknesses were approximately 15-20 nm, as measured by a stylus profilometer (Ambios XP-100).

All devices for impedance spectroscopy measurements were prepared on Corning 1737 glass substrates patterned with 140 nm of ITO. CPE solutions were prepared in an N_2-filled glovebox at concentrations of 20 mg/mL and 40mg/mL in 99.9% dry methanol and incubated overnight at 60 °C. Substrates were scrubbed with detergent, then sonicated for 10 minutes each in DI water, acetone, and isopropyl alcohol and dried at 150 °C overnight. After treating with O_2-plasma for 5 min, ITO substrates were coated with a 40 nm PEDOT:PSS (Clevios P VP AI 4083) layer, annealed in air for 20 minutes at 140 °C, then moved into the glovebox. CPE layers were spin-casted onto the PEDOT:PSS at 1500 rpm, and dried on a hotplate at 60 °C for 15 min. Finally, a 100 nm layer of aluminum was thermally evaporated by shadow mask to yield device areas of $\sim$19 mm^2

as measured by profilometry. For temperature-dependent conductivity measurements, the PEDOT:PSS interlayer was omitted to avoid the interdiffusion of ions at elevated temperatures.

Kelvin probe force microscopy: Surface potential measurements were performed in a nitrogen-filled glovebox using the built-in amplitude modulation Kelvin probe force microscopy (AM-KPFM) routine on an MFP3D atomic force microscope (Asylum Research). KPFM is a capacitive technique for determining the contact potential difference (CPD) between an AFM tip and a sample surface. This implementation utilizes a two-pass scanning method, where a height profile is collected on the first scan and surface potential is measured on the second scan. The second scan is operated without force feedback at a constant lift height of 20 nm based on the height profile. This increased tip-sample distance ensures that shorter-ranged van der Waals forces do not affect tip-sample interactions. During the lift scan, a steady AC signal is applied to the cantilever, causing oscillation. Perturbations in the cantilever's oscillation amplitude occur due to capacitive charge buildup caused by a CPD between tip and sample. The CPD is then determined by way of a feedback loop that applies a bias to the cantilever equal and opposite in sign to the CPD, minimizing perturbation of the cantilever motion. Cr/Pt-coated n-Si probes with resonant frequency of 300 kHz and force constant of 40 N/m (Budget Sensors) were used in all measurements. A bias stress was provided externally using a Keithley 236 unit, which was provided with a common ground to the AFM. The lateral resolution of the measurement was limited by two factors. First, shadow mask deposition results in gold electrodes that are not as sharp-edged as lithographically defined contacts, as can be seen from the device profiles shown in the text. And second, the potentials recorded in AM-SKPM are distorted by capacitive coupling between the cantilever and the substrate, resulting in spatially broader data.[38,46,47] To obtain ρ(x), the 2nd derivative of the potential profile is determined numerically, and the potential profile

is first processed with a spline smoothing routine to remove small noise fluctuations. The fast scanning speed necessary for maximizing time resolution limits lateral resolution in V(x). CPD values can also be convoluted with the effects of probe geometry, interactions between the cantilever and the sample surface, and thermal noise fluctuations, and deconvolution algorithms are needed to obtain more quantitative CPD profiles.[48,49]. Another consequence of broadened potential profiles is a lower curvature, which suppresses the apparent density observed at sharp potential steps like the polymer-electrode interface. While these factors limit the quantitative accuracy and lateral resolution of the ρ(x) profile, the method used to describe ion relaxation through the decay of the integrated ion population near the stressed electrode is mostly unaffected by these limits.

Impedance Spectroscopy: Impedance of CPE parallel plate devices was measured using a Solartron 1260 impedance analyzer, applying an AC amplitude of 100mV from 0.1 Hz to 1 MHz at 0 V DC bias. J-V characteristics were collected before and after each set of impedance measurements using a Keithley 2600 voltage source to ensure the stability of the device. Temperature was controlled by placing the test device within a large metal block on a hot plate and allowing 15 minutes at each temperature before measuring. X-ray reflectivity: Reflectivity measurements were performed using a SmartLab High Resolution Diffractometer (Rigaku), with a 1.54 ÅX-ray. Test films were prepared by spin-coating onto quartz substrates to yield thicknesses of $\sim$35 nm. Reflectivity data were fit using a built-in simulation package to yield an estimate of mass density.

References

1. Hoven, C. V.; Yang, R.; Garcia, A.; Crockett, V.; Heeger, A. J.; Bazan, G. C.; Nguyen, T.-Q. *PNAS* **2008**, *105*, 12730–12735.

2. Duan, C.; Wang, L.; Zhang, K.; Guan, X.; Huang, F. *Adv. Mater.* **2011**, *23*, 1665–1669.

3. Hoven, C.; Yang, R.; Garcia, A.; Heeger, A. J.; Nguyen, T.-Q.; Bazan, G. C. *J. Am. Chem. Soc.* **2007**, *129*, 10976–10977.

4. Fang, J.; Wallikewitz, B. H.; Gao, F.; Tu, G.; Müller, C.; Pace, G.; Friend, R. H.; Huck, W. T. S. *J. Am. Chem. Soc.* **2011**, *133*, 683–685.

5. Garcia, A.; Bakus II, R. C.; Zalar, P.; Hoven, C. V.; Brzezinski, J. Z.; Nguyen, T.-Q. *J. Am. Chem. Soc.* **2011**, *133*, 2492–2498.

6. Lee, B. H.; Jung, I. H.; Woo, H. Y.; Shim, H.-K.; Kim, G.; Lee, K. *Adv. Funct. Mater.* **2014**, *24*, 1100–1108.

7. Seo, J. H.; Gutacker, A.; Walker, B.; Cho, S.; Garcia, A.; Yang, R.; Nguyen, T.-Q.; Heeger, A. J.; Bazan, G. C. *J. Am. Chem. Soc.* **2009**, *131*, 18220–18221.

8. He, Z.; Zhong, C.; Su, S.; Xu, M.; Wu, H.; Cao, Y. *Nat Photon* **2012**, *6*, 591–595.

9. Chen, H.-Y.; Hou, J.; Zhang, S.; Liang, Y.; Yang, G.; Yang, Y.; Yu, L.; Wu, Y.; Li, G. *Nat Photon* **2009**, *3*, 649–653.

10. Choi, H.; Park, J. S.; Jeong, E.; Kim, G.-H.; Lee, B. R.; Kim, S. O.; Song, M. H.; Woo, H. Y.; Kim, J. Y. *Adv. Mater.* **2011**, *23*, 2759–2763.

11. Zhou, H.; Zhang, Y.; Mai, C.-K.; Collins, S. D.; Nguyen, T.-Q.; Bazan, G. C.; Heeger, A. J. *Adv. Mater.* **2014**, *26*, 780–785.

12. Choi, H.; Mai, C.-K.; Kim, H.-B.; Jeong, J.; Song, S.; Bazan, G. C.; Kim, J. Y.; Heeger, A. J. *Nature Communications* **2015**, *6*, DOI: 10.1038/ncomms8348.

13. Seo, J. H.; Nguyen, T.-Q. *J. Am. Chem. Soc.* **2008**, *130*, 10042–10043.

14. Seo, J. H.; Yang, R.; Brzezinski, J. Z.; Walker, B.; Bazan, G. C.; Nguyen, T.-Q. *Adv. Mater.* **2009**, *21*, 1006–1011.

15. Lim, K.-G.; Park, S. M.; Woo, H. Y.; Lee, T.-W. *ChemSusChem* **2015**, *8*, 3062–3068.

16. Hoven, C. V.; Peet, J.; Mikhailovsky, A.; Nguyen, T.-Q. *Applied Physics Letters* **2009**, *94*, 033301.

17. van Reenen, S.; Kouijzer, S.; Janssen, R. A. J.; Wienk, M. M.; Kemerink, M. *Adv. Mater. Interfaces* **2014**, *1*, 00189.

18. Walker, E. M.; Lonergan, M. C. *J. Phys. Chem. C* **2013**, *117*, 14929–14938.

19. Cheng, C. H. W.; Lin, F.; Lonergan, M. C. *J. Phys. Chem. B* **2005**, *109*, 10168–10178.

20. Tordera, D.; Kuik, M.; Rengert, Z. D.; Bandiello, E.; Bolink, H. J.; Bazan, G. C.; Nguyen, T.-Q. *J. Am. Chem. Soc.* **2014**, *136*, 8500–8503.

21. Nishikitani, Y.; Takizawa, D.; Nishide, H.; Uchida, S.; Nishimura, S. *J. Phys. Chem. C* **2015**, *119*, 28701–28710.

22. Tekoglu, S.; Petzoldt, M.; Stolz, S.; Bunz, U. H. F.; Lemmer, U.; Hamburger, M.; Hernandez-Sosa, G. *ACS Appl. Mater. Interfaces* **2016**, *8*, 7320–7325.

23. Gu, Z.; Shen, Q.-D.; Zhang, J.; Yang, C.-Z.; Bao, Y.-J. *J. Appl. Polym. Sci.* **2006**, *100*, 2930–2936.

24. Mai, C.-K.; Arai, T.; Liu, X.; L. Fronk, S.; M. Su, G.; A. Segalman, R.; L. Chabinyc, M.; C. Bazan, G. *Chemical Communications* **2015**, *51*, 17607–17610.

25. Mai, C.-K.; Russ, B.; Fronk, S. L.; Hu, N.; Chan-Park, M. B.; Urban, J. J.; Segalman, R. A.; Chabinyc, M. L.; Bazan, G. C. *Energy Environ. Sci.* **2015**, *8*, 2341–2346.

26. Mai, C.-K.; Schlitz, R. A.; Su, G. M.; Spitzer, D.; Wang, X.; Fronk, S. L.; Cahill, D. G.; Chabinyc, M. L.; Bazan, G. C. *J. Am. Chem. Soc.* **2014**, *136*, 13478–13481.

27. Stavrinidou, E.; Leleux, P.; Rajaona, H.; Khodagholy, D.; Rivnay, J.; Lindau, M.; Sanaur, S.; Malliaras, G. G. *Adv. Mater.* **2013**, *25*, 4488–4493.

28. Giovannitti, A.; Nielsen, C. B.; Rivnay, J.; Kirkus, M.; Harkin, D. J.; White, A. J.; Sirringhaus, H.; Malliaras, G. G.; McCulloch, I. *Adv. Funct. Mater.* **2015**, 03791.

29. Khodagholy, D.; Rivnay, J.; Sessolo, M.; Gurfinkel, M.; Leleux, P.; Jimison, L. H.; Stavrinidou, E.; Herve, T.; Sanaur, S.; Owens, R. M.; Malliaras, G. G. *Nat Commun* **2013**, *4*, DOI: 10.1038/ncomms3133.

30. Malti, A.; Edberg, J.; Granberg, H.; Khan, Z. U.; Andreasen, J. W.; Liu, X.; Zhao, D.; Zhang, H.; Yao, Y.; Brill, J. W.; Engquist, I.; Fahlman, M.; Wågberg, L.; Crispin, X.; Berggren, M. *Adv. Sci.* **2016**, *3*, 00305.

31. Mikhnenko, O. V.; Collins, S. D.; Nguyen, T.-Q. *Adv. Mater.* **2015**, *27*, 2007–2012.

32. Brus, V. V.; Collins, S. D.; Mikhnenko, O. V.; Wang, M.; Bazan, G. C.; Nguyen, T.-Q. *Advanced Electronic Materials* **2016**, *2*, DOI: 10.1002/aelm.201500344.

33. Garcia, A.; Brzezinski, J. Z.; Nguyen, T.-Q. *J. Phys. Chem. C* **2009**, *113*, 2950–2954.

34. Zalar, P.; Nguyen, T.-Q. In *Conjugated Polyelectrolytes*, Liu, B., Bazan, G. C., Eds.; Wiley-VCH Verlag GmbH & Co. KGaA: 2012, pp 315–344.

35. Lin, F.; Wang, Y.; Lonergan, M. *Journal of Applied Physics* **2008**, *104*, 103517.

36. Pingree, L. S. C.; Rodovsky, D. B.; Coffey, D. C.; Bartholomew, G. P.; Ginger, D. S. *J. Am. Chem. Soc.* **2007**, *129*, 15903–15910.

37. Meier, S. B.; van Reenen, S.; Lefevre, B.; Hartmann, D.; Bolink, H. J.; Winnacker, A.; Sarfert, W.; Kemerink, M. *Adv. Funct. Mater.* **2013**, *23*, 3531–3538.

38. Matyba, P.; Maturova, K.; Kemerink, M.; Robinson, N. D.; Edman, L. *Nat Mater* **2009**, *8*, 672–676.

39. van Reenen, S.; Matyba, P.; Dzwilewski, A.; Janssen, R. A. J.; Edman, L.; Kemerink, M. *J. Am. Chem. Soc.* **2010**, *132*, 13776–13781.

40. Lange, I.; Blakesley, J. C.; Frisch, J.; Vollmer, A.; Koch, N.; Neher, D. *Phys. Rev. Lett.* **2011**, *106*, 216402.

41. Zhang, Y.; Zalar, P.; Kim, C.; Collins, S.; Bazan, G. C.; Nguyen, T.-Q. *Adv. Mater.* **2012**, *24*, 4255–4260.

42. Calzolari, A.; Vercelli, B.; Ruini, A.; Virgili, T.; Pasini, M. *J. Phys. Chem. C* **2013**, *117*, 26760–26767.

43. Mills, T. J.; Lonergan, M. C. *Phys. Rev. B* **2012**, *85*, 035203.

44. Clarke, J. H. R. In *The Physics of Glassy Polymers*, Haward, R. N., Young, R. J., Eds.; Springer Netherlands: 1997, pp 33–83.

45. Liu, B.; Gaylord, B. S.; Wang, S.; Bazan, G. C. *J. Am. Chem. Soc.* **2003**, *125*, 6705–6714.

46. Charrier, D. S. H.; de Vries, T.; Mathijssen, S. G. J.; Geluk, E. .-.-J.; Smits, E. C. P.; Kemerink, M.; Janssen, R. A. J. *Organic Electronics* **2009**, *10*, 994–997.

47. Charrier, D. S. H.; Kemerink, M.; Smalbrugge, B. E.; de Vries, T.; Janssen, R. A. J. *ACS Nano* **2008**, *2*, 622–626.

48. Jacobs, H. O.; Leuchtmann, P.; Homan, O. J.; Stemmer, A. *Journal of Applied Physics* **1998**, *84*, 1168–1173.

49. Strassburg, E.; Boag, A.; Rosenwaks, Y. *Review of Scientific Instruments* **2005**, *76*, 083705.

Appendices

Appendix A

Appendix to Chapter 3

A.1 DOS Distributions and Fermi Level

The relationship between charge density and the DOS can be approximated by the convolution of the Boltzmann distribution with the DOS function, $g(E)$, as in Equation (1):

$$n(E) = \int_{E_F}^{\infty} g(E) \cdot \exp\left(\frac{E_F - E}{kT}\right) dE \tag{1}$$

The shape of the function describing the DOS can most clearly be distinguished by the density dependence of the Fermi level, as described by Blakeseley and Neher.[1] The case of a Gaussian DOS is shown in Equation (2) for a LUMO distribution.

$$g(E) = \frac{N}{\sigma\sqrt{2\pi}} \exp\left(-\frac{(E - E_{LUMO})^2}{(2\sigma)^2}\right) \tag{2}$$

Here, σ is the width of disorder, E_{LUMO} is the LUMO DOS maximum or center, and N is the density of states at E_{LUMO}. In this treatment, disorder leads to an effective LUMO energy $E_{LUMO,eff}$ (Equation (3)) below which the Fermi level change with density follows

the thermal voltage, kT (Equation (4)).

$$E_{LUMO,eff} = E_{LUMO} - \frac{\sigma^2}{kT} \tag{3}$$

$$E_{F,e} = E_{LUMO,eff} + kT \ln\left(\frac{n}{N_0}\right) \tag{4}$$

In an exponential DOS (Equation (5)), E_F follows a slope equal to the characteristic energy of the exponential distributions, $E_t = mkT$, where $m > 1$ (Equation (6)), with a maximum at E_{LUMO}.

$$g(E) = N \exp\left(\frac{E - E_{LUMO}}{E_t}\right) \tag{5}$$

$$E_{F,e} = E_{LUMO} + mkT \ln\left(\frac{n}{N_0}\right) \tag{6}$$

The resulting relationship between the DOS distributions $\mathrm{V_{OC}}$ was derived previously by Lange *et al.*,[2] and was shown for the case of a fully exponential DOS in the main text. In the case of a fully Gaussian combined DOS, $\mathrm{qV_{OC}}$ would follow a slope of $2kT$ as the natural log of carrier density n below $\mathrm{E}_{g,eff}$, where $\mathrm{E}_{g,eff} = \mathrm{E}_{HOMO,eff} - \mathrm{E}_{LUMO,eff}$ and N_{eff} is the effective density of states at $\mathrm{E}_{g,eff}$:

$$qV_{\mathrm{OC}} = E_{g,eff} + 2k_BT \ln\left(\frac{n}{N_{eff}}\right) \tag{7}$$

A.2 Calculated Voltage Losses from Disorder and Recombination

Using the maximum density of states value N estimated from the point where ΔV_{OC}= 0, we obtain a simplified exponential DOS distribution that describes the combined donor-acceptor energetics relative to E_{CT}. From this, it is possible to quantify the contribution of disorder to the total voltage loss as:

$$V_{disorder} = m_{DA} kT \ln\left(\frac{n_{oc}}{N}\right) \tag{8}$$

$V_{disorder}$ is defined as the difference between the measured V_{OC} and that calculated for a system with minimal disorder (where $m_{DA} = 2$) at the same charge density, and therefore describes loss due to 'excess' disorder in the system. $V_{disorder}$ is calculated for each system at the 1-sun condition. After having accounted for $V_{disorder}$, the remainder of $\Delta V_{OC}$is attributed to recombination in the absence of 'excess' disorder, and is given as V_{rec} = ΔV_{OC} - $V_{disorder}$. Again using the N value from above from the convergence at zero loss, it follows that V_{rec} should be described by:

$$V_{\mathrm{rec}} = 2kT \ln\left(\frac{n_{oc}}{N}\right) \tag{9}$$

In order to properly compare V_{rec} in DTS:N2200 with the other systems, it should be noted that a larger N leads to an increase in ΔV_{OC}simply because it decreases the value of $\ln \frac{n_{oc}}{N}$. According to Equation (8), this leads to a 0.047 V loss due only to the difference between N values. Therefore, an adjusted V_{rec} value is used for DTS:N2200 when analyzing trends across all systems. When V_{rec} is plotted against n_{oc} (Figure A.1), reasonable agreement is obtained with a plot of Equation (9) (solid line).

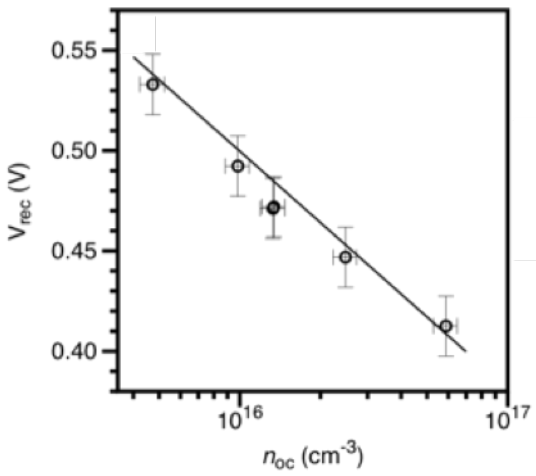

Figure A.1: Voltage loss due to recombination (V_{rec}) calculated as ΔV_{OC} – $V_{disorder}$, plotted at n_{oc}, along with a line plot of Equation (8).

A.3 The Effect of Geminate Losses on V_{OC}

The relative loss due to a low generation rate is determined with respect to the highest rate of generation, represented as G_0:

$$V_G = kT \ln\left(\frac{G}{G_0}\right) \tag{10}$$

By taking V_{rec} to consist of loss due to relatively low generation and to the rate of recombination ($V_{rec} = V_Y + V_G$), $V_{rec} - V_G$ then gives the trend in voltage loss due only to differences in the recombination strength between systems, V_γ, which is described by a function varying only with γ:

$$V_\gamma = kT \ln\left(\frac{G_0}{N_0^2}\right) - kT \ln(\gamma) \tag{11}$$

A plot of $V_\gamma$vs. γ (Figure A.2a) shows reasonable agreement with a plot of Equation (11). In the text, an exponential decrease in γ is observed with increasing ϵ_r, which is consistent with the fact that a plot of $V_\gamma$vs. ϵ_r shows a decreasing linear trend, which

here has a slope of -0.064 V (Figure A.2b).

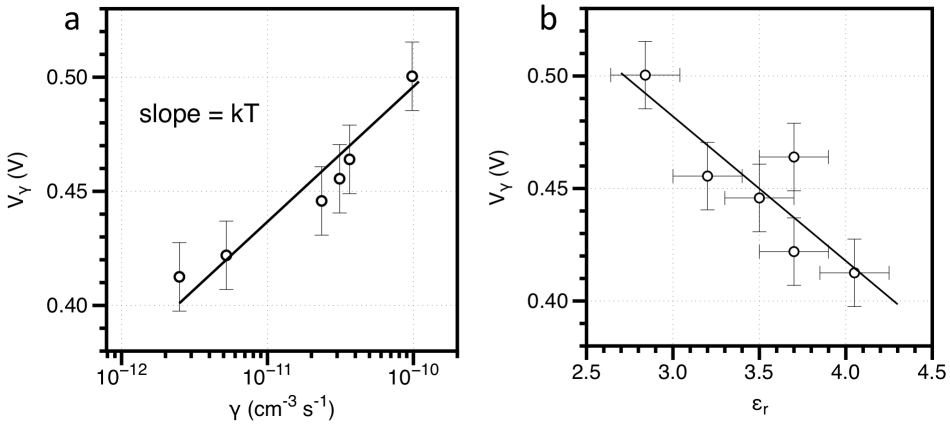

Figure A.2: a) $V_\gamma$plotted as a function of γ, with line plot of Equation (11). b) $V_\gamma$plotted vs. ϵ_r, with linear fit (slope = -0.064 V).

Previous work has shown that some systems appear to suffer from geminate losses near open-circuit conditions, and so a correction may be made to the generation rate estimated at reverse bias (G_sat) using a correction factor. This correction factor is based on the difference in charge generation at reverse bias and at open-circuit, and is estimated by the difference in charge collected by bias-assisted charge extraction (BACE). The effect of field-dependent generation is reported elsewhere for DPP2:PC_{71}BMand DTS:PC_{71}BM with and without DIO,[3] as well as for DPP3:PC_{71}BM(unpublished). Field-dependent generation in DPP1:PC_{71}BM and DTS:N2200 were not analyzed, and instead an upper bound for field-dependent loss was estimated from the fill factor at 1-sun illumination. The observed fill factors are 0.43 and 0.59 for DPP1:PC_{71}BM and DTS:N2200, respectively. Table A.1 shows the saturated (G_{sat})and corrected (G) generation rates at V_{OC} for all systems.

Table A.1: Estimated generation rate at V_{OC}

Blend	G_{sat} (10^{21} cm^{-3} s^{-1})	geminate loss correction factor	G (10^{21} cm^{-3} s^{-1})
DPP1:$PC_{71}BM$	5.35	0.6	3.2
DPP2:$PC_{71}BM$	6.24	0.5	3.1
DPP3:$PC_{71}BM$	8.32	0.5	4.2
DTS:$PC_{71}BM$	8.74	0.75	6.6
DTS:$PC_{71}BM$(DIO)	8.67	1	8.7
DTS:N2200	2.44	0.9	2.3

References

1. Blakesley, J. C.; Neher, D. *Phys. Rev. B* **2011**, *84*, 075210.

2. Lange, I.; Blakesley, J. C.; Frisch, J.; Vollmer, A.; Koch, N.; Neher, D. *Phys. Rev. Lett.* **2011**, *106*, 216402.

3. Proctor, C. M.; Albrecht, S.; Kuik, M.; Neher, D.; Nguyen, T.-Q. *Adv. Energy Mater.* **2014**, *4*, 00230.

Appendix B

Appendix to Chapter 4

B.1 Transition Dipole Moments of p-DTS(FBTTh$_2$)$_2$

To understand the relationship between polarization angle in the pd-pcAFM image and the orientation of the molecules, the transition dipole moments of p-DTS(FBTTh2) were calculated. Following the calculations of the related small molecule p-DTS(PTTh$_2$)$_2$ (C-F is replaced by an N atom) by Zhugayevych *et al.*, time-dependent density functional theory (TD-DFT) calculations were performed using Gaussian09 at a CAM-B3LYP/6-31G* level of theory with the side-chains omitted and the solvent chloroform was included using the conductor-like polarizable continuum model to mimic the dielectric effects of the crystalline environment.[g09, zhugayevychJPCC2013] It is important to note that the acceptor units of p-DTS(FBTTh$_2$)$_2$ adopt a different conformation in single crystals (**Figure B.1a**) as compared to p-DTS(PTTh$_2$)$_2$. However, as both conformations of the acceptor units may be present in the thin film, we include the calculations with the acceptor units flipped, similar to p-DTS(PTTh$_2$)$_2$ (**Figure B.1b**). The transition dipole orientations and wavelengths for excited states with appreciable oscillator strengths are listed in Table B.1. The orientation of the acceptor units is observed to change the orientation of

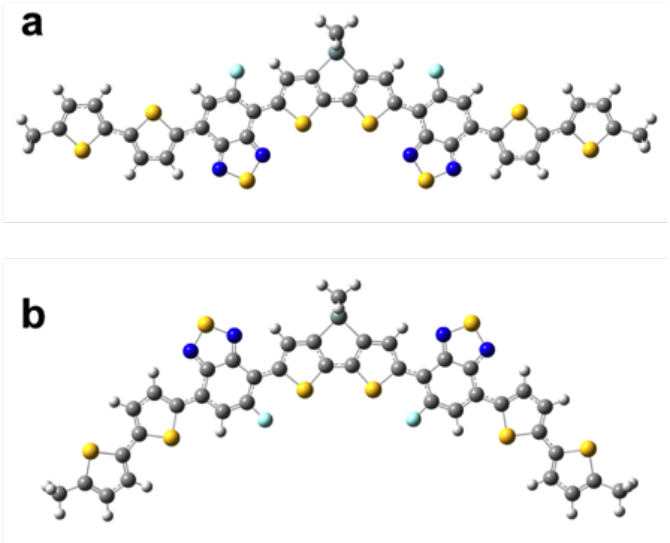

Figure B.1: Optimized geometries for two symmetric conformations of p-DTS(FBTTh$_2$)$_2$. a) The expected conformation in the crystal structure, and b) another energetically low-lying conformation, with acceptor units flipped about the core DTS unit.

the transition dipoles associated with the high-energy absorption band (i.e. around 410 nm). For the conformation in the single crystal structure, conformation 1, the transition dipole moments at low- and high-energy are along the long-axis of the molecule. For conformation 2, the dependence of transition dipole orientation in the high-energy band is more complicated but the low-energy transition is still along the molecular long-axis. Thus, probing within the low-energy band is likely to give a more robust picture of the orientational order of the molecules. But it may be possible in the future to probe conformational disorder by detailed comparison of pd-pcAFM images at different wavelengths.

B.2 Fitting BHJ Films of Optimized Blend

The interleaved pd-pcAFM image and contact-mode height image for the four polarization measurement of optimized p-DTS(FBTTh$_2$)$_2$:PC$_{71}$BM in the main text are shown

Table B.1: Wavelength and transition dipole direction relative to the molecular long-axis for conformations 1 and 2 shown in Figure B.1a and Figure B.1b, respectively.

Wavelength (nm)	Oscillator Strength	Direction of Transition Dipole
Conformation 1		
730	2.58	Parallel
379	0.75	Parallel
337	0.53	Parallel
Conformation 2		
706	2.42	Parallel
555	0.33	Perpendicular
382	0.45	Parallel
345	0.40	Perpendicular
335	0.33	Parallel

in **Figure B.2**. No obvious structure is observed in the height image. The extracted images, in-plane polarizations of 0°, 45°, 90°, and 135°, are shown in **Figure B.3**. For reference, the zero angle is taken to point in the vertical direction (towards the top of the page) and increasing angles move clockwise in-plane. The orthogonal pairs show relatively complementary structure as expected and the sum of all photocurrent maps is quite uniform.

The four polarized photocurrent maps were fit to Equation (1) by minimizing the mean squared error (MSE) at each (x,y) pair. A brute force method was used to ensure the global minimum was found. The estimated coefficients $A(x, y)$ and $B(x, y)$ are shown in **Figure B.4**. A histogram of $R(x, y)$, the ratio of the photocurrents parallel and perpendicular to the director as derived from the fit coefficients, is shown in **Figure B.5a**. It is useful to note that the order parameter is identical to the fraction

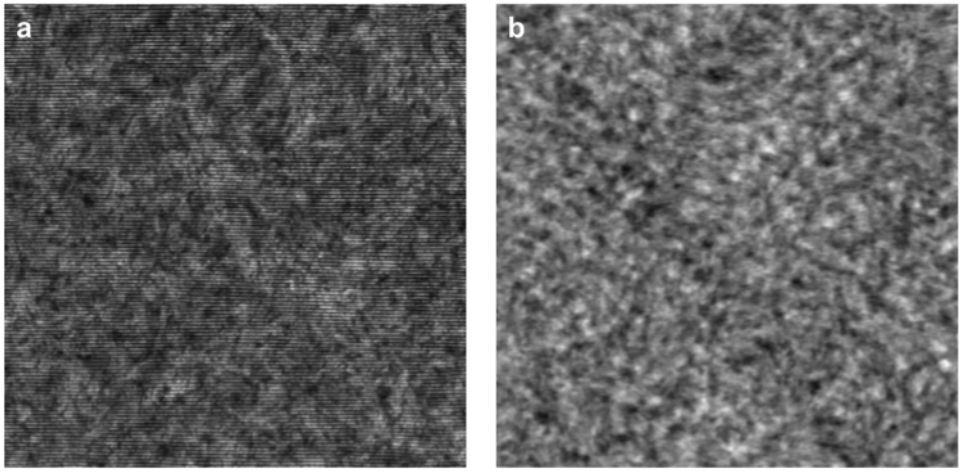

Figure B.2: a) Interlaced pd-pcAFM image with 0°, 45°, 90°, and 135° in-plane polarizations. b) Contact-mode height image acquired during the pd-pcAFM scan (±5 nm grey scaling). Both images are 5 μm x 5 μm in size.

of polarization-dependent current, which corresponds to the integral of the polarization dependent current with respect to the incident polarization divided by the integral of the total current with respect to incident polarization. A histogram of the local order parameters is shown in **Figure B.5b**.

$$I(x, y; \beta) = A(x, y) + 2B(x, y)\cos^2(\beta - \phi(x, y)) \quad (1)$$

We note that pcAFM imaging is dependent on the AFM tip-quality and this can lower the fraction of polarization-dependent photocurrent. Poor quality tips tend to give 'streaky', 'patchy', and visibly fuzzy/noisy features in the photocurrent maps. As the tip quality improves, the photocurrent features become sharper and more distinct while the distribution of $R(x, y)$ (*e.g.*, Figure B.5) narrows and shifts to higher values.

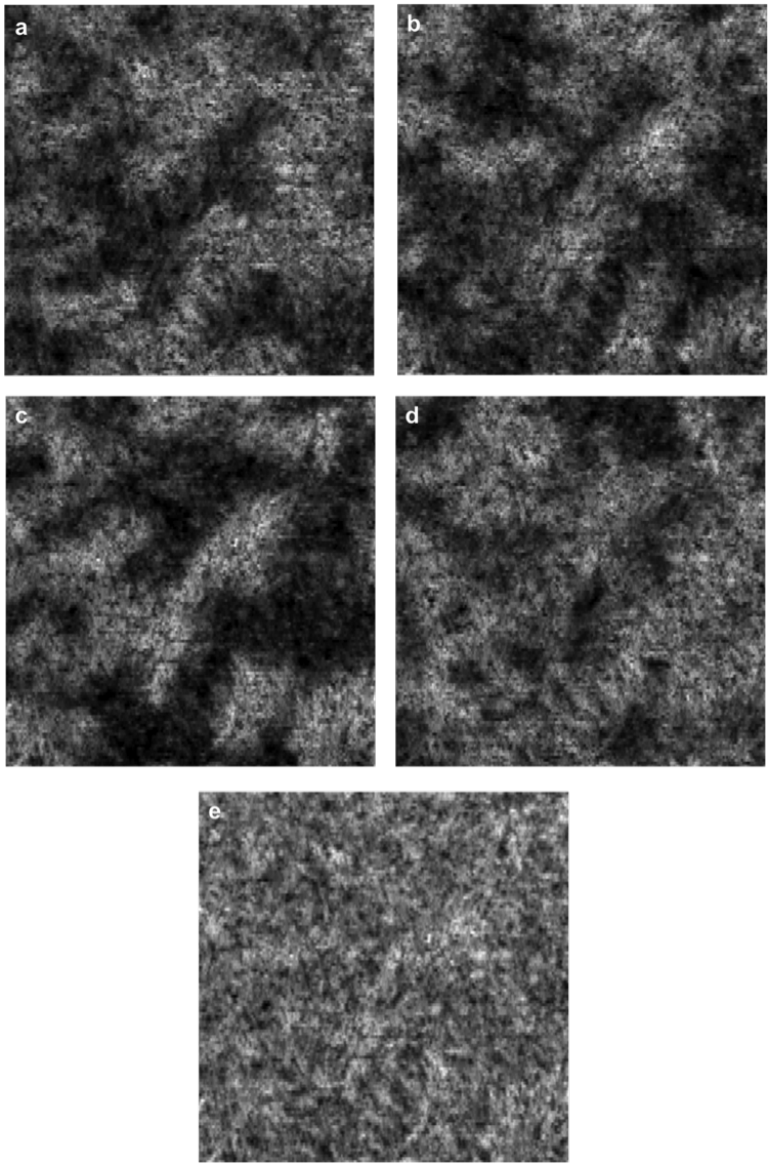

Figure B.3: Extracted pd-pcAFM photocurrent maps at a) 0°, b) 45°, c) 90°, and d) 135°. Photocurrent maps were taken at a 2V bias and scaled from 80 to 400 pA. e) The sum of the four polarization images. All images are stretched to keep a 1:1 aspect ratio and are 5 μm x 5 μm in size. .

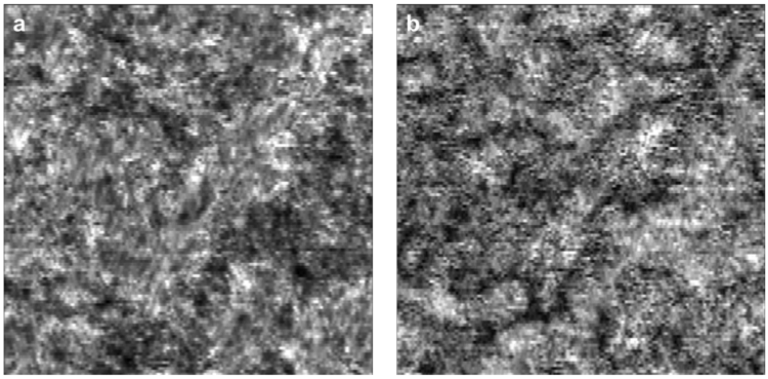

Figure B.4: Fitting coefficients a) $A(x, y)$ and b) $B(x, y)$. Part (a) is scaled from 50 to 200 pA. Part (b) is scaled from 0 to 100 pA. Both maps are 5 μm per side.

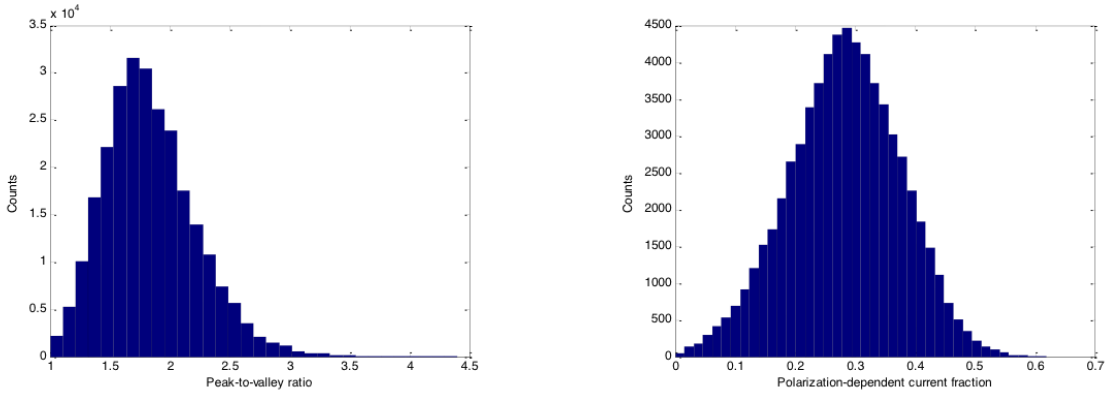

Figure B.5: Histogram of a) $R(x, y)$, the ratio of photocurrent parallel and perpendicular to the local molecular director, and b) the local order parameter for a single pd-pcAFM image. The mean values of $R(x, y)$ and the position averaged order parameter are 1.83 and 0.29, respectively.

B.3 Fitting BHJ Films Without Solvent Additive

It has been previously established that processing p-DTS($FBTTh_2$)$_2$:$PC_{71}BM$ films without the solvent additive diiodooctane or high temperature thermal annealing results in OPV devices with lower PCE.[vanderpollAM2012] Structural investigations suggest the as-cast blend film is more disordered than the optimized blend films; no signs of the fibular structure or phase separation were observed in with HR-TEM or cross-sections of the BHJ layer although a weak in-plane $\pi-\pi$ stacking peaks is observed with GIWAXS.[loveAFM2013] Dark-field TEM and pd-pcAFM measurements of the as-cast p-DTS($FBTTh_2$)$_2$:$PC_{61}BM$ blend show long-range order similar to the optimized blend. Dark-field images show long-range order and a complementary structure with micron-scale order similar to the optimized blend (**Figure B.6**). The pd-pcAFM photocurrent maps used for constructing the director field in Figure 4.8b in Chapter 4 are shown in **Figure B.7** and the $A(x, y)$ and $B(x, y)$ fit coefficients are shown in **Figure B.8**. Near the disclination cores, where transition dipoles adopt a range of orientations, the $B(x, y)$ coefficients are significantly reduced and the $A(x, y)$ coefficients increase. The distribution of the peak-to-valley ratio and the fraction of polarization-dependent current are shown in Figure B.9. In general, the photocurrent maps are much more homogeneous without the fibular structure, and the order parameter ranges from 0.3 to 0.4.

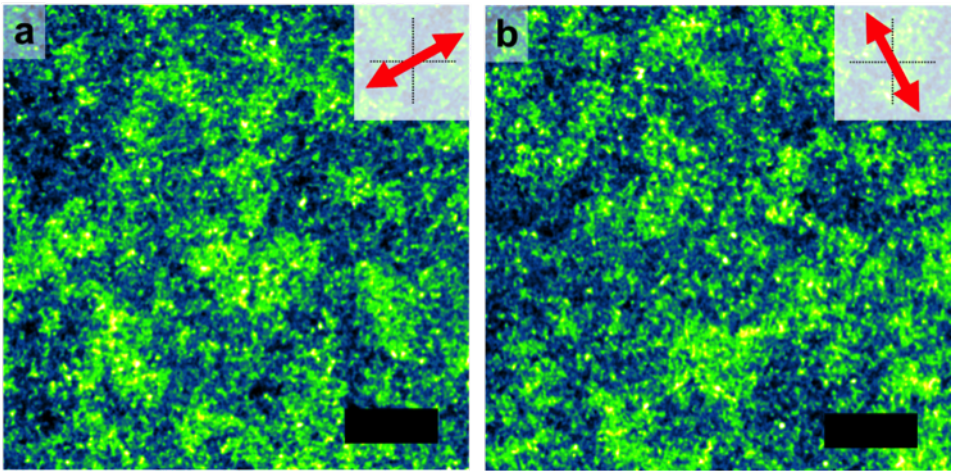

Figure B.6: Dark-field images of p-DTS(FBTTh2)2:PC60BM blend films processed without solvent additive or high temperature thermal annealing. Part (a) and (b) show two orthogonal crystallite directions as indicated by the red arrows. Images are 6 μm x 6 μm per side.

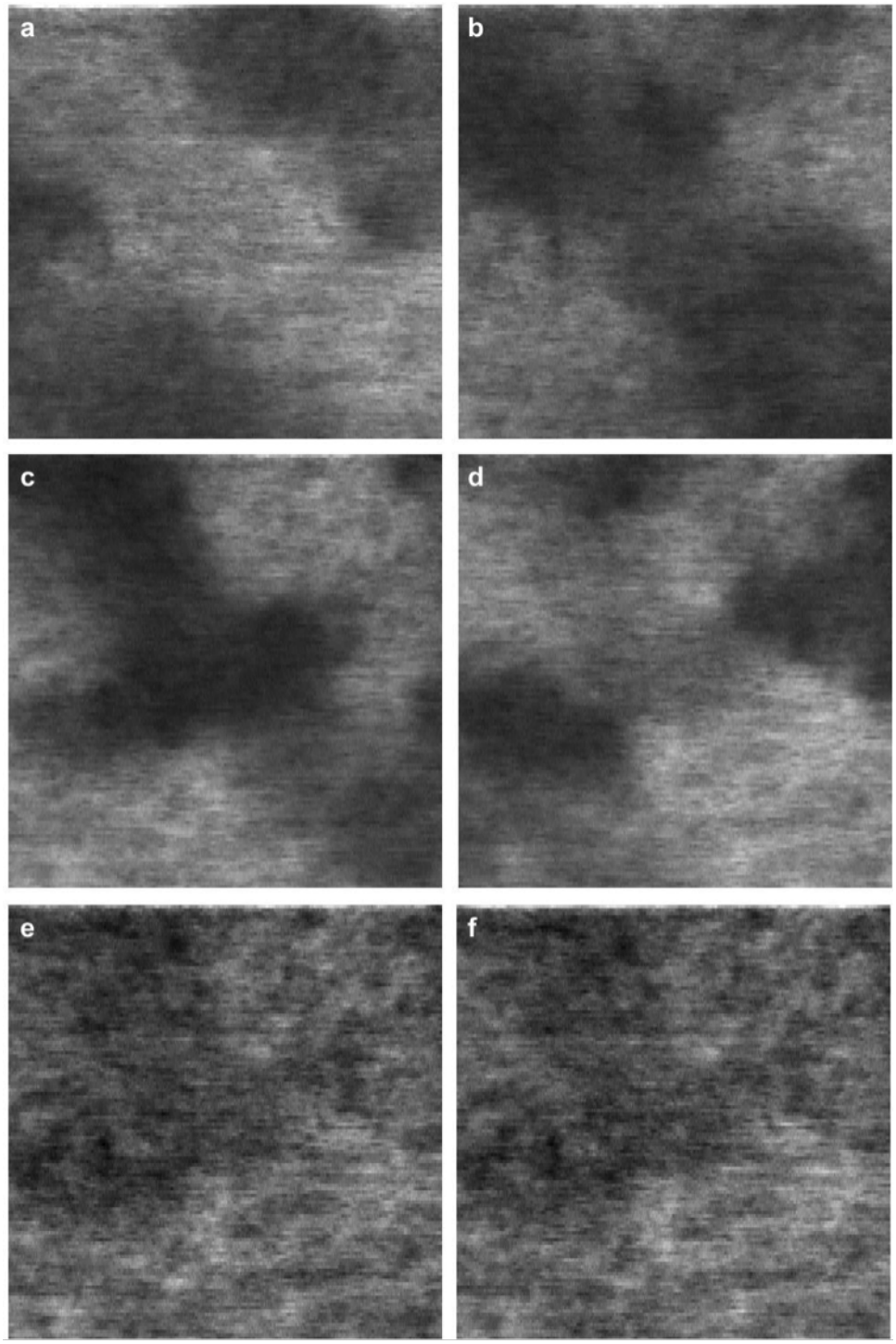

Figure B.7: Extracted pd-pcAFM photocurrent maps at a) 0°, b) 45°, c) 90°, and d) 135° for the as-cast BHJ. Photocurrent maps were taken at a 1 V bias and scaled from 1 to 14 pA. e) Sum of 0° and 90° photocurrent maps. f) Sum of 45° and 135° photocurrent maps. The sum images are scaled from 8 to 20 pA. All images are stretched to keep a 1:1 aspect ratio and are 2 μm x 2 μm in size.

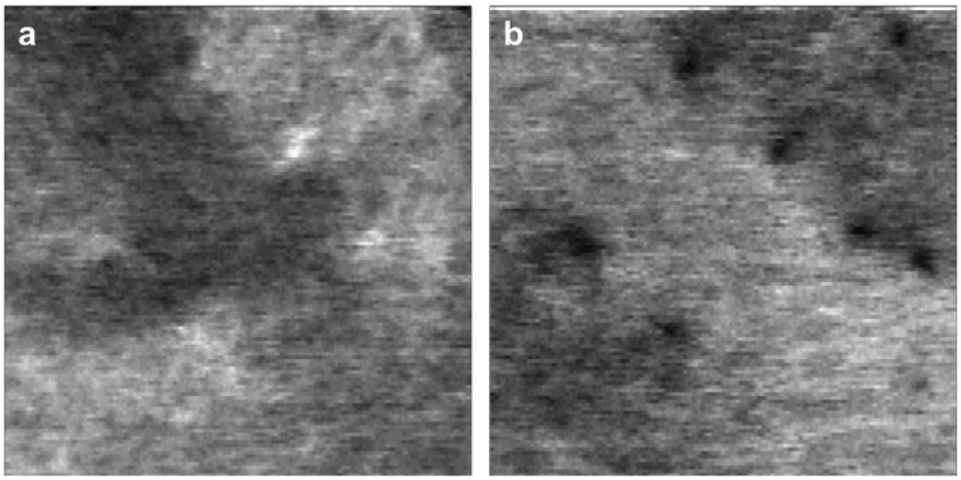

Figure B.8: Fitting coefficients (a) A(x,y) and (b) B(x,y) for the as-cast BHJ. Part (a) is scaled from 2 to 7 pA. Part (b) is scaled from 0 to 4 pA. Both maps are 2 μm x 2 μm in size.

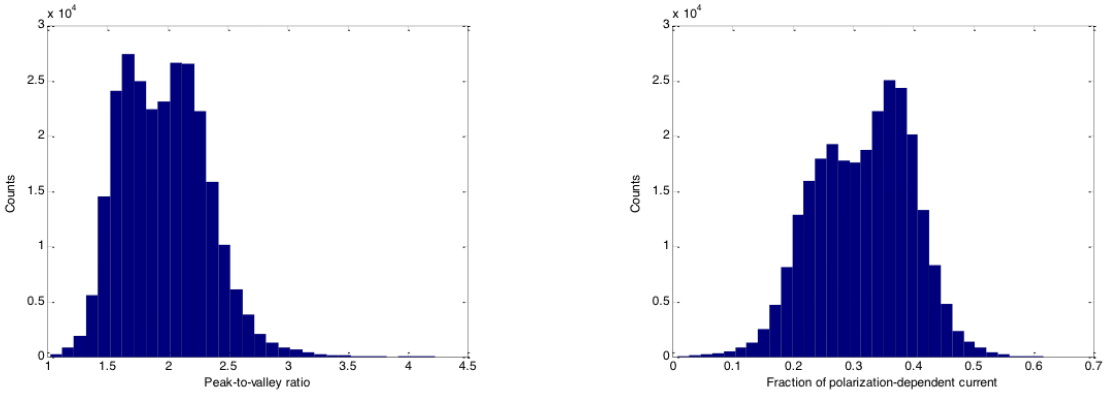

Figure B.9: Histogram of (a) R(x,y), the ratio of photocurrent parallel and perpendicular to the local molecular director, and (b) the local order parameter for the pd-p-cAFM image. The mean values of R(x,y) and the position averaged order parameter are 2.0 and 0.32, respectively.

B.4 Pure Donor Films

Orientational order over several microns is also observed in the pure donor film with pd-pcAFM. The photocurrent maps are shown in **Figure B.10** for the data presented in Figure 4.9 in Chapter 4. The bright spots in the photocurrent maps correspond to pinhole defects. This does not seem to have a significant effect on the observed polarization dependence but the increased photocurrent but does signify a change in the sample-tip interaction. As expected, the magnitude of the photocurrent is lower without the fullerene assisting charge-generation. Moreover, the change in the measured length-scale provides additional evidence that the polarization-dependent photocurrent is not an experimental artifact. The extracted fit coefficients and their sum are shown in **Figure B.11**. Following the discussion in the main text, the regions of higher splay show lower values of B(x,y) and correspondingly higher values of A(x,y). The sum of the coefficients, which approximate the unpolarized photocurrent response, is nearly uniform except within the pinholes. The distribution of R(x,y) and the local order parameters are shown in **Figure B.12**.

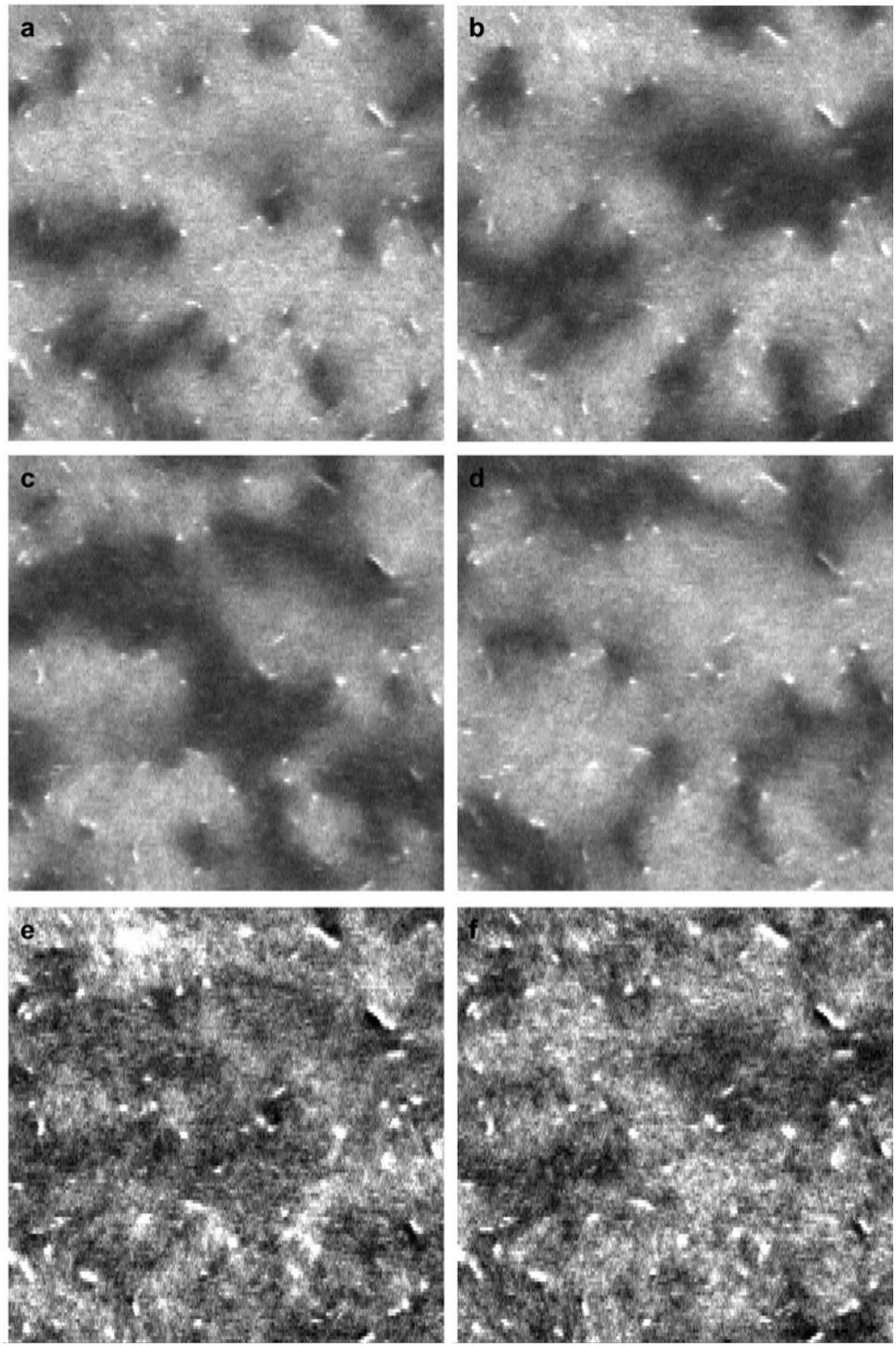

Figure B.10: Extracted pd-pcAFM photocurrent maps at (a) 0°, (b) 45°, (c) 90°, and (d) 135° for the pure donor film. Photocurrent maps were taken at a 1.5V bias and scaled from 1 to 8 pA. e) Sum of 0° and 90° photocurrent maps. f) Sum of 45° and 135° photocurrent maps. Parts (e) and (f) are scaled from 8 to 12 pA. All images are stretched to keep a 1:1 aspect ratio and are 10 μm x 10 μm in size.

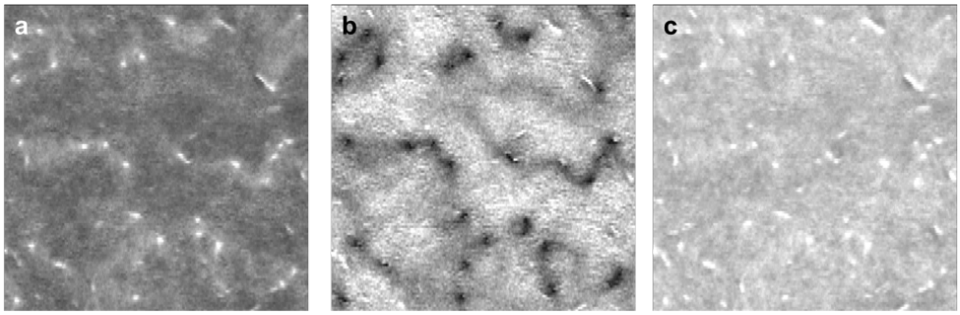

Figure B.11: Fit coefficients for the pristine film for a) A(x,y) scaled from 0 to 6 pA and b) B(x,y) scaled from 0 to 2 pA. c) Sum of A(x,y) and B(x,y) scaled from 0 to 6 pA. All images are 10 μm per side.

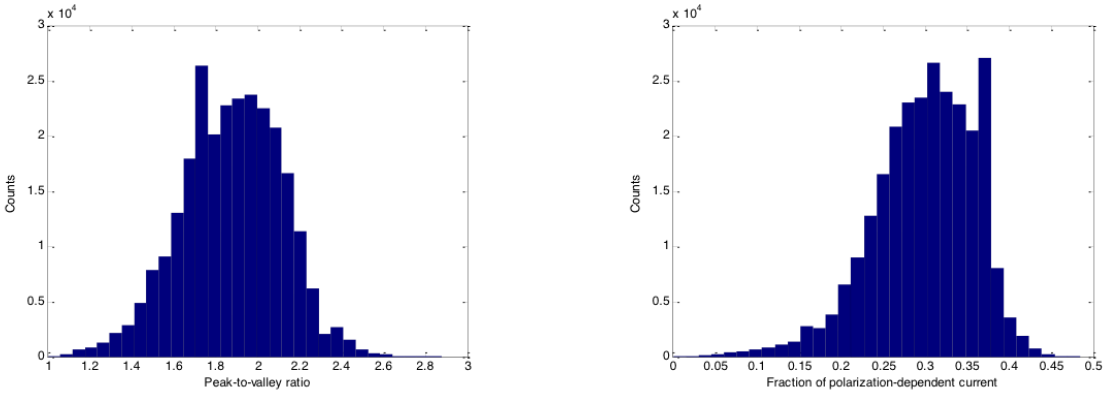

Figure B.12: Histogram of the a) peak-to-valley ratio and b) fraction of polarization-dependent current. The mean values of the peak-to-valley ratio and polarization-dependent photocurrent are 1.83 and 0.30, respectively.

B.5 Angular Dependence of Absorption

The high degree of orientational order suggests a more realistic treatment of the absorption may be helpful when fitting the photocurrent maps. The simple polarization dependence in Equation (1) is likely accurate when the fraction of the absorbed light is small, *i.e.*, self-absorption is negligible. However, the polarization-dependence absorption deviates from $\eta cos^2(\theta)$, where η is the optical density, as the exponential absorption through the film thickness becomes important. This effect is easily demonstrated by plotting Equation (2), the light absorbed by a perfectly oriented film as a function of the incident polarization, versus Equation (B.5), the simplified form valid for small optical densities, for several different values of the optical density (**Figure B.13**). Note that for values of θ sufficiently close to 90°, the approximation of Equation (B.5) is always valid.

$$1 - exp(-\eta cos^2(\theta)) \tag{2}$$

$$\eta cos^2(\theta) \tag{3}$$

We restrict our attention to the deviations in the shape of the absorption profile as a function of optical density and incident polarization (**Figure B.14**). The deviations in the shape of the absorption profile prevent the sum of two orthogonal polarization photocurrent maps from forming a true complementary pair as η increases. It is easily shown (Figure B.10e-f) that the sum of the 0° and 90° photocurrent maps is not equal to the sum of the 45° and 135° photocurrent maps in the case of the pure film. A significant effort was first made to explain the difference in the summed photocurrent maps by polarization-dependent intensity fluctuations, but it was ultimately found not to be able to explain the effect. It may be possible to estimate the optical density of the

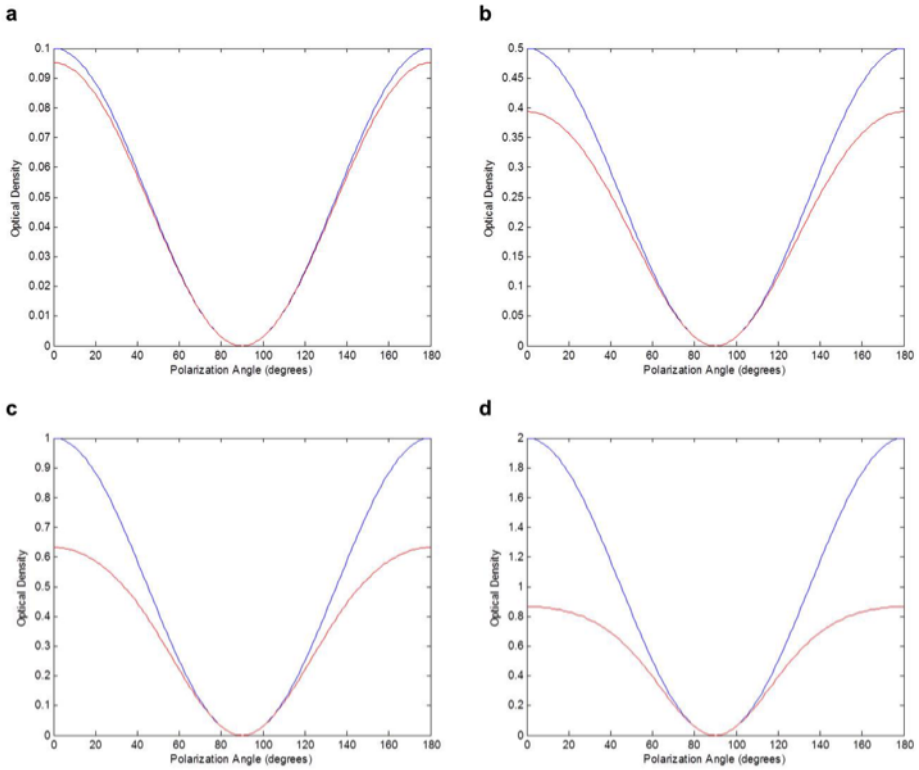

Figure B.13: Optical absorption of a perfectly oriented film of optical density, η, versus incident polarization: (a) 0.1, (b) 0.5, (c) 1.0, and (d) 2.0. The red and blue lines correspond to the full and approximate expressions given by Equation (2) and Equation (B.5), respectively.

molecules with long-range order in the future but any such number should be taken with a grain of salt. Given our current understanding, it is difficult to conclusively assign these deviations to light absorption as the anisotropic transport properties could also play a role.

The effects of the exponential absorption through the film were modeled by a spatially dependent optical density $\eta(x, y)$ that modifies the shape of the fitting function. The full model now appears in Equation (4). It should be noted this adds a weakly coupled fourth parameter to our fits; the values of A(x,y) and B(x,y) are not substantially affected, but the mean square error is lowered. Adding this parameter was most helpful for the pure film ($\eta \sim 1.1$), moderately helpful for optimized blend ($\eta \sim 0.5$), and least relevant for

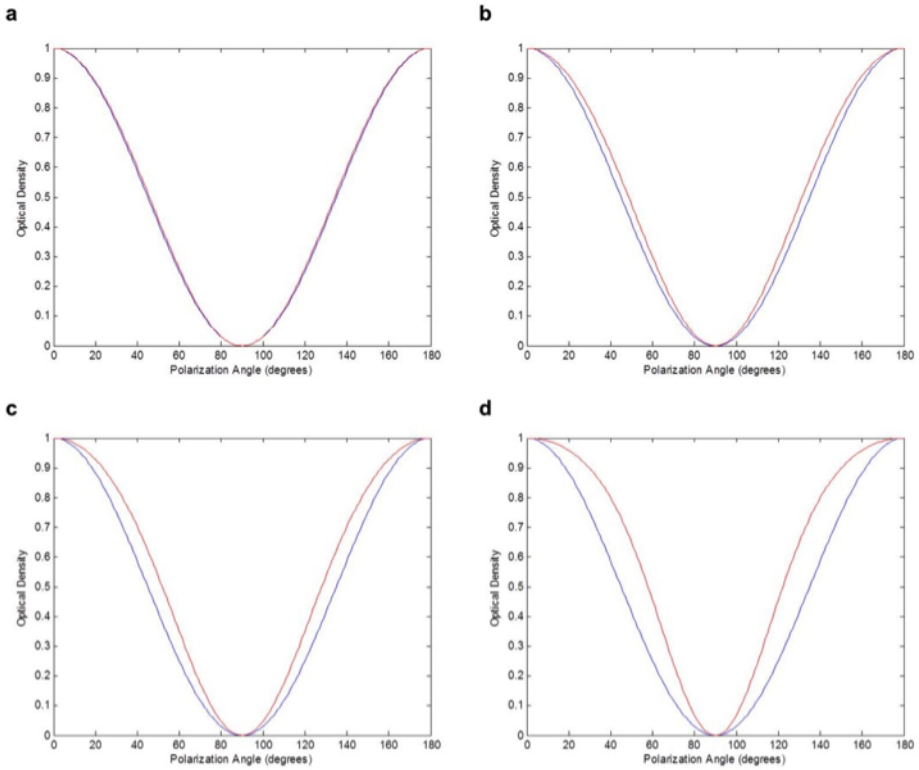

Figure B.14: Normalized optical absorption of a perfectly oriented film of optical density, η, versus incident polarization: (a) 0.1, (b) 0.5, (c) 1.0, and (d) 2.0. The red and blue lines correspond to the full and approximate expressions given by Equation (2) and Equation (B.5), respectively. All curves have been normalized to unity at $\theta = 0°$.

the as-cast blend ($\eta \sim 0.2$).

$$I(x,y;\beta) = A(x,y) + \frac{2B(x,y)(1 - exp(-\eta(x,y)cos^2(\beta - \phi(x,y))))}{1 - exp(-\eta(x,y))} \tag{4}$$

It is useful to examine the distortion of the summed photocurrent maps as a function of η. For summed orthogonal photocurrent maps (0° and 90° incident polarizations), the angular distortion is described by Equation (5) and it depends on both the in-plane orientation of the molecules with respect to the incident polarization and the magnitude of η. The expression converges in the limit $\eta \rightarrow 0$ to $cos^2(\phi) + sin^2(\phi) = 1$, which is the expected result for dipole-like absorption. However, the angular distortion is appreciable

even for $\eta \sim 0.5$ (**Figure B.15a**). Interestingly, the distortions are almost exactly canceled if four polarizations (0°, 45°, 90°, and 135°) are summed (Equation (6)) even for values of $\eta \sim 1$ (**Figure B.15b**). Thus, the sum of four photocurrent maps is expected to be more uniform than either orthogonal pair, particularly as η increases, which is in agreement with the results of both the optimized BHJ and pristine films.

$$\frac{1 - exp(-\eta cos^2(0° - \phi))}{1 - exp(-\eta)} + \frac{1 - exp(-\eta cos^2(90° - \phi))}{1 - exp(-\eta)} \tag{5}$$

$$\begin{aligned} &\frac{1 - \exp(-\eta cos^2(0° - \phi))}{1 - \exp(-\eta)} + \frac{1 - \exp(-\eta cos^2(45° - \phi))}{1 - \exp(-\eta)} + \\ &\frac{1 - \exp(-\eta cos^2(90° - \phi))}{1 - \exp(-\eta)} + \frac{1 - \exp(-\eta cos^2(135° - \phi))}{1 - \exp(-\eta)} \end{aligned} \tag{6}$$

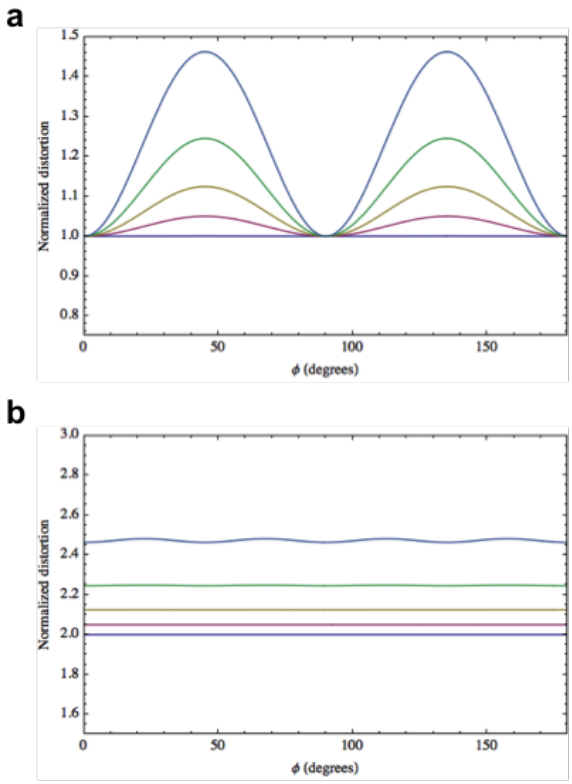

Figure B.15: a) Distortion in the photocurrent profile for (a) the sum of orthogonal photocurrent maps and (b) four summed photocurrent maps for $\eta = \{0, 0.2, 0.5, 1.0, 2.0\}$

References

1. Mikhnenko, O. V.; Collins, S. D.; Nguyen, T.-Q. *Adv. Mater.* **2015**, *27*, 2007–2012.

2. Lee, B. H.; Jung, I. H.; Woo, H. Y.; Shim, H.-K.; Kim, G.; Lee, K. *Adv. Funct. Mater.* **2014**, *24*, 1100–1108.

Appendix C

Appendix to Chapter 5

C.1 Description of Monte Carlo Simulation

Ionic charge transport can be modeled by solving the drift-diffusion, continuity, and Poisson equations:

$$\overrightarrow{j}(\overrightarrow{r},t) = qp(\overrightarrow{r},t)\mu\overrightarrow{E}(\overrightarrow{r},t) - qD\nabla p(\overrightarrow{r},t), \tag{1}$$

$$\nabla\overrightarrow{j}(\overrightarrow{r},t) = q\frac{\partial p(\overrightarrow{r},t)}{\partial t}, \tag{2}$$

$$\nabla(\epsilon(\overrightarrow{r})\nabla V(\overrightarrow{r},t) = -\frac{qp(\overrightarrow{r},t)}{\epsilon_0} \tag{3}$$

Here j is electrical current, $\overrightarrow{r}$ is coordinate, t is time, q is elementary charge, μ is charge carrier mobility, $\overrightarrow{E}$ is electric field, D is diffusion coefficient, p is charge carrier density, V is electrostatic potential, ϵ is relative permittivity, and ϵ_0 is permittivity of free space. The Poisson equation poses significant computational load that is mostly responsible for

the large time needed to perform numerical simulations of charge transport. To solve the Poisson equation, a computer performs mostly division operations. Divisions are the slowest floating-point operations being 5-10 times slower than additions, depending on hardware. Therefore it is desirable to minimize division operations in favor of additions. Moreover, modern CPUs allow vector operations, which enables execution of up to 8 floating point additions simultaneously on each computational core. First, we solve the Poisson equation using the Green function approach:

$$\nabla(\epsilon(\overrightarrow{r})\nabla G(\overrightarrow{r},\overrightarrow{s}) = -\frac{q\delta(\overrightarrow{r}-\overrightarrow{s})}{\epsilon_0}, \tag{4}$$

where $G(\overrightarrow{r},\overrightarrow{s})$ is the Green function, and $\delta(\overrightarrow{r})$ is the Dirac delta-function. If at any given time the charge distribution is $p(\overrightarrow{s})$, then the solution of the Poisson equation is:

$$V(\overrightarrow{r}) = \int G(\overrightarrow{r},\overrightarrow{s})p(\overrightarrow{s})d\overrightarrow{s}. \tag{5}$$

Equation (5) is an integral equation, which means that in order to evaluate $V(\overrightarrow{r})$ a computer would perform only fast addition operations if the Green function is known. For instance, **Figure C.1** shows the calculated Green functions for two locations: (a) close to an electrode and (b) in the middle of the device. The Green functions (a) and (b) represent the electrostatic potentials of two charges that are located at these locations. In order to evaluate the combined electrostatic potential (c) of both charges, we must simply add (a) and (b). Note that in the common scale, electrostatic potential of the charge close to the electrode is much weaker as compared to the central charge due to the image charge effects near the interface with a metal. We must numerically solve Equation (4) only once for each device geometry. The numerical Green function is then written to a file and can

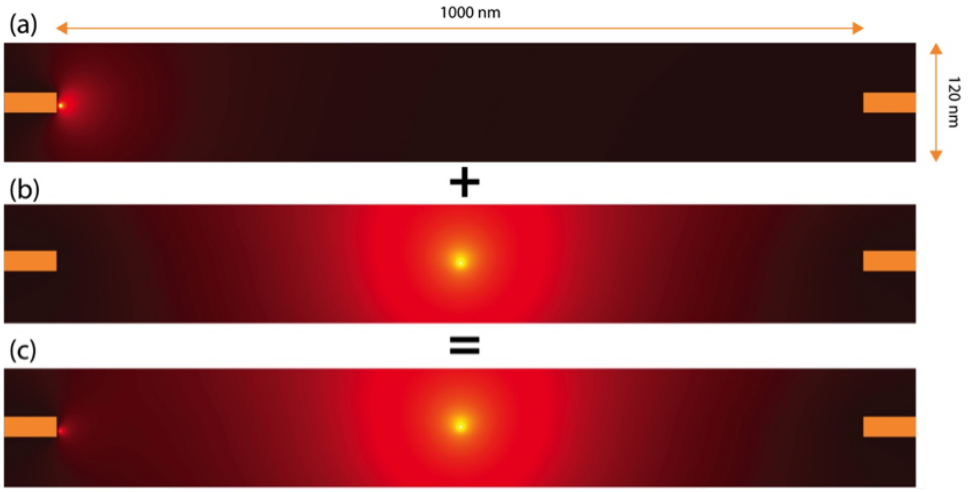

Figure C.1: a) and b): the Green functions of the Poisson equation in a real device configuration for two locations. The electrostatic potential values are represented by false coloring. The orange bars represent 20 nm thick gold electrodes - source and drain. The bottom gate electrode is separated form the gold electrodes by 300 nm of SiO_2 and is not shown by the vertical scale on these images. c) The sum of (a) and (b).

be further used to solve the drift-diffusion equation. An additional advantage of this approach is that we can obtain the solution of the Poisson equation with high precision without extending the execution time of the rest of simulation. To ensure maximum flexibility of our simulation, we use the Monte-Carlo approach to solve Equation (1) and Equation (2). Due to the device symmetry, we will only consider a two-dimensional problem that corresponds to the cross-section normal to the device electrodes. We will model the dynamics of each individual charge. For every time iteration dt, each charge will be moved by the distance ds according to Equation (1):

$$d\overrightarrow{s} = \mu \overrightarrow{E}(\overrightarrow{r}, t)dt + \sqrt{4Ddt}\overrightarrow{n}. \tag{6}$$

Here the first term represents the drift component. The second term is 2-D diffusion according to the Einstein-Smoluchowski theory of random walks. We assume that the Einstein relationship holds for the mobility and the diffusion coefficient. $\overrightarrow{n}$ is a unit

vector pointing at random direction. Such an approach automatically satisfies the continuity equation (Equation (2)). It important to note that the charge coordinates are not restrained by a grid in our simulation. We keep track of the electric field $\overrightarrow{E}(\overrightarrow{r}, t)$ on a 1 nm grid. The total field is a sum of partial electric fields caused by each individual charge and electrodes (Figure C.1). Thus to move a charge from location r_1 to location r_2 we would first subtract the electric field of the charge at r_1, and then we would add the electric field of the charge at position r_2. In an analogous way, we will change the voltage of an electrode from V_1 to V_2. Previously we tested the simulation against the Mott-Gurney law in a diode configuration, and in a transistor configuration we obtained output and transfer characteristics that are consistent with experimental data.**mikhnenkoAM2015** Numerous performance enhancements have been deployed in order to make the computer simulation highly efficient. For instance, we took advantage of the fact that the electric field of a charge varies slowly at large distances. For this reason one can describe the far field of a charge on grids with larger spacing than 1 nm. To model ionic motion in CPEs the Monte Carlo simulation takes the following input parameters:

- Measurements of the device geometry.
- Dielectric constant of CPE.
- Solution of Poisson equation previously computed by our Poisson solver and stored in a file.
- Measurements of the device geometry.
- The stress voltage, at which ions were initially displaced.
- The density of 'free' ions.
- The mobility of the 'free' ions.

The simulation starts by placing the 'free' ions at random position within the device channel. The covalently bound to the polymer backbone counter-ions were modeled as homogeneously distributed charge with total value equal to the total charge of the 'free' ions. Then a large voltage is applied to one of the electrodes until equilibrium of ionic distribution is reached. We neglected the electronic current in the device for two reasons: (i) there is a large injection barrier for both electrons and holes, and (ii) we did not measure significant electrical current during the application of large voltage through the device. Once the equilibrium is reached, the stress voltage is then released and the ions relax to their pre-stress condition. The snapshots of ionic distribution are taken at sufficiently small time intervals and the stress-release cycle is repeated until smooth data is collected for the ionic distribution within the device channel. The output of the simulation is the time dependence of ionic density near the electrodes. This output is compared to the measured by Kelvin probe data, so the adjustments to the ionic mobility and density are made and fed back to the simulation until a good agreement between the measured and experimental data is obtained.

C.2 Temperature-Dependent Ionic Conductivity

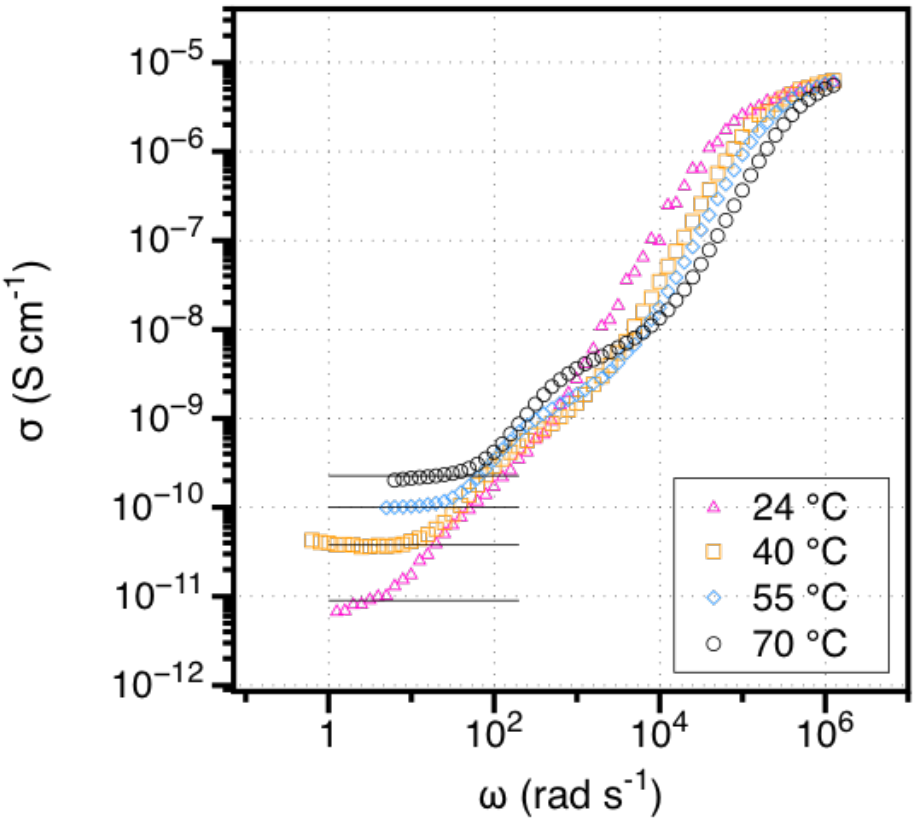

Figure C.2: Conductivity spectrum as a function of temperature for a 200 nm-thick PFN-P4-BIM_4 device fabricated with the structure glass/ITO/PFN-P4-BIm_4/Al. Each data point is obtained from the average of 200 cycles.

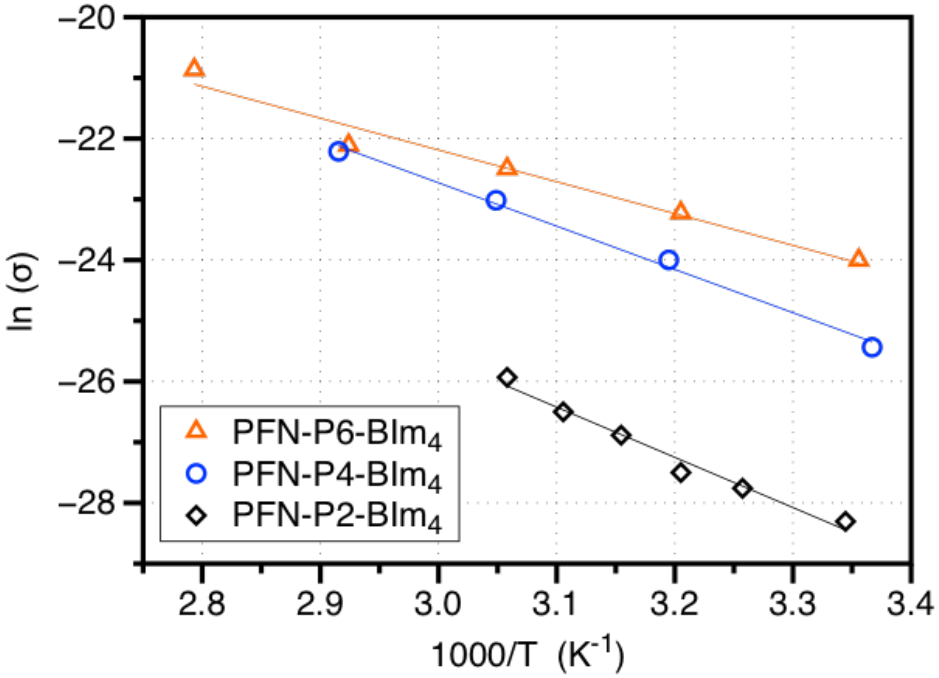

Figure C.3: Arrhenius plot of temperature-dependent ionic conductivity for PFN-P4-BIM$_2$, PFN-P4-BIM$_4$, and PFN-P4-BIM$_6$ devices prepared with the structure glass/ITO/CPE/Al. Devices were heated to 100 °C for 1 hour prior to carrying out measurements.

C.3 X-ray Reflectivity

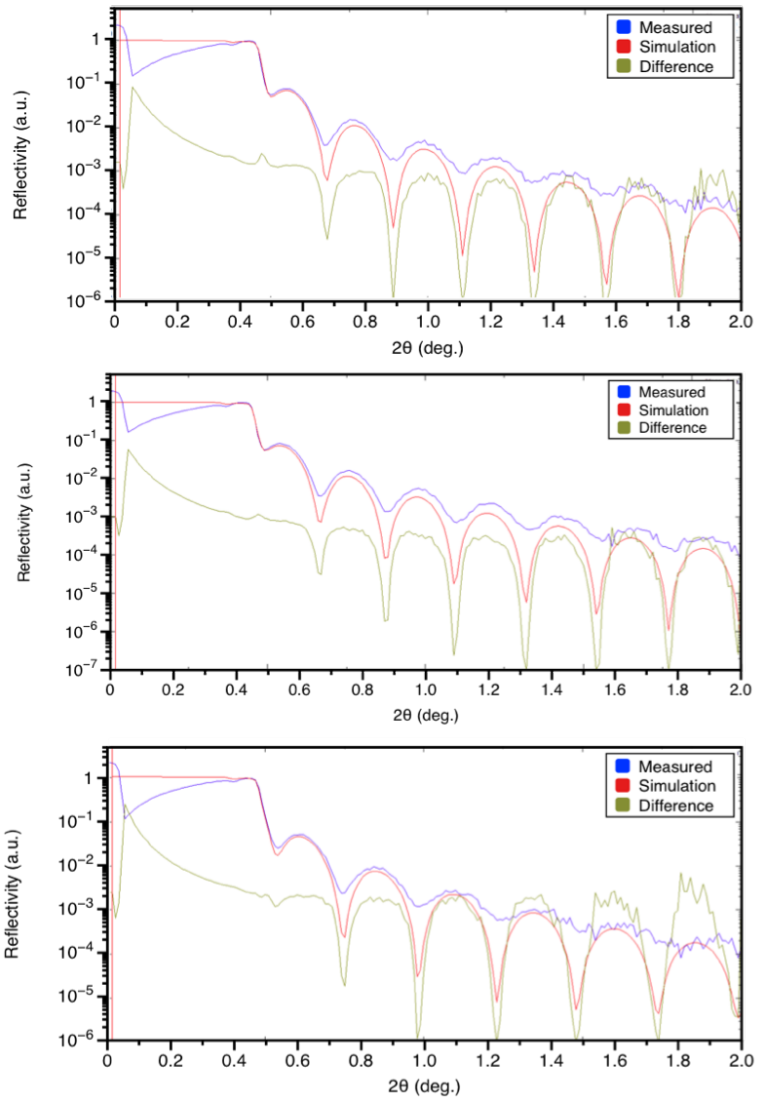

Figure C.4: Experimental X-ray reflectivity measurements along with simulated best fit used to obtain film density for a) PFN-P4-BIM$_2$, b) PFN-P4-BIM$_4$, and c) PFN-P4-BIM$_6$. Film thicknesses are approximately 35 nm. Simulated fits to reflectivity data show densities of $\sim$1.2 g cm^{-3} for all three materials

C.4 UV-VIS of CPE Films

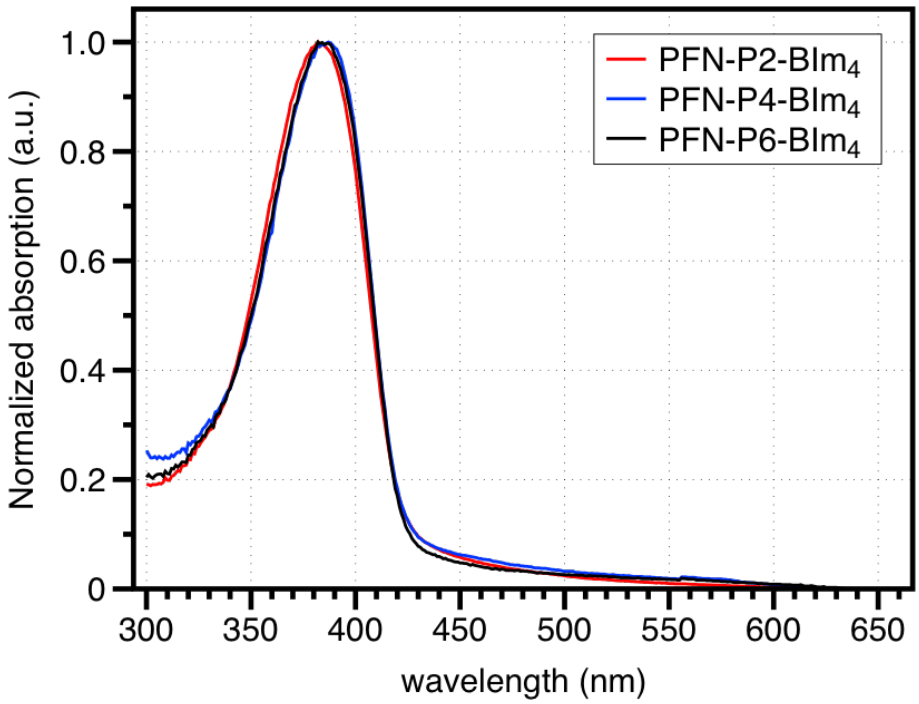

Figure C.5: UV-VIS absorption spectra of PFN-P4-BIM_2, PFN-P4-BIM_4, and PFN-P4-BIM_6 films prepared on quartz substrates. Evidence for the lack of higher order structures and an overall amorphous film morphology can be found by comparing this spectrum to that of UV-VIS in dilute solution, where λ_{max} has been observed at ~370 nm.[leeAFM2014] The wavelength of peak absorption, which is virtually the same for all three materials, is approximately 385 nm, indicating a minimal red shift going from solution to solid state. Because solid-state packing has only a negligible affect on molecular order, and the absorption spectrum lacks any additional features, the films are therefore considered amorphous.

References

1. Frisch, M. J. et al., Gaussian Inc. Wallingford CT 2009.

2. Zhugayevych, A.; Postupna, O.; Bakus II, R. C.; Welch, G. C.; Bazan, G. C.; Tretiak, S. *J. Phys. Chem. C* **2013**, *117*, 4920–4930.

3. van der Poll, T. S.; Love, J. A.; Nguyen, T.-Q.; Bazan, G. C. *Advanced Materials* **2012**, *24*, 3646–3649.

4. Love, J. A.; Proctor, C. M.; Liu, J.; Takacs, C. J.; Sharenko, A.; van der Poll, T. S.; Heeger, A. J.; Bazan, G. C.; Nguyen, T.-Q. *Adv. Funct. Mater.* **2013**, *23*, 5019–5026.